Quantitative Computed Tomography

Der Technischen Fakultät der
Universität Erlangen–Nürnberg

zur Erlangung des Grades

DOKTOR–INGENIEUR

vorgelegt von

Michael Balda

Erlangen — 2011

Als Dissertation genehmigt von der
Technischen Fakultät der
Universität Erlangen-Nürnberg

Tag der Einreichung:	20.05.2011
Tag der Promotion:	14.09.2011
Dekan:	Prof. Dr.-Ing. R. German
Berichterstatter:	Prof. Dr.-Ing. J. Hornegger
	Prof. Dr. rer. biol. hum. M. Kachelrieß

Quantitative Computertomographie

Der Technischen Fakultät der
Universität Erlangen–Nürnberg

zur Erlangung des Grades

DOKTOR–INGENIEUR

vorgelegt von

Michael Balda

Erlangen — 2011

Als Dissertation genehmigt von der
Technischen Fakultät der
Universität Erlangen-Nürnberg

Tag der Einreichung:	20.05.2011
Tag der Promotion:	14.09.2011
Dekan:	Prof. Dr.-Ing. R. German
Berichterstatter:	Prof. Dr.-Ing. J. Hornegger
	Prof. Dr. rer. biol. hum. M. Kachelrieß

Zusammenfassung

Computertomographie (CT) ist ein weit verbreitetes, bildgebendes Verfahren in der Medizin. Traditionelle CT liefert Informationen über die Anatomie eines Patienten in Form von Schichtbildern oder Volumendaten. Hierbei werden sogenannte Hounsfield-Einheiten verwendet, die Aufschluss über die Gewebezusammensetzung geben. Aufgrund der polychromatischen Eigenschaften der für CT verwendeten Röntgenstrahlung sind die Werte für alle Materialien bzw. Gewebetypen außer Wasser und Luft von deren Dichte und Zusammensetzung aber auch von verschiedenen CT-Systemparametern und Einstellungen abhängig. Ziel der quantitativen CT (QCT) ist es, Messwerte zu liefern die bestimmte Materialcharakteristika möglichst exakt beschreiben. Dies kann z. B. die Dichteverteilung bestimmter Materialien wie Kontrastmittel oder die lokale Röntgenabsorption sein. Darauf aufbauend sind verschiedene spezifische Anwendungen wie etwa Perfusionsdiagnostik oder die Schwächungskorrektion für Positronen-Emissions-Tomographie realisierbar.

Diese Arbeit widmet sich drei wesentlichen Themengebieten der QCT. Nach einer kurzen Übersicht über die technischen und physikalischen Grundlagen wird die spektrale Detektion von Röntgenstrahlung für CT behandelt. Hierbei werden zwei Simulationskonzepte für CT-Detektoren vorgestellt, die sich für spektrale Detektion eignen. Dies sind der integrierende Szintillationsdetektor und der zählende Direktwandler. Für erstere existieren spezielle Varianten, die geeignet sind, um spektrale Daten für quantitative CT zu liefern, der letztere liefert direkt spektrale Daten. Ziel der vorgestellten Simulationen ist es, die Simulation eines kompletten CT-Scans derart zu beschleunigen, dass es möglich ist, entsprechende Detektorparameter im Hinblick auf die Qualität der rekonstruierten Daten zu optimieren. Dies wird durch ein auf das spezifische Detektordesign zugeschnittene Simulationskonzept erreicht, welches durch geeignete Lookup-Tabellen unterstützt wird. Verglichen mit Standard-Partikelinteraktionssimulationen können somit um einen Faktor $1/200$ kürzere Simulationslaufzeiten erreicht werden. Die hierbei erreichte Genauigkeit liegt auf dem gleichen Niveau wie die der Standardsimulationen und konnte mit realen Ergebnissen von Prototypen und Messstationen abgeglichen werden.

Das zweite behandelte Themenfeld sind Algorithmen für QCT, die mit den gewonnenen spektralen Messdaten Anwendungen der QCT realisieren. Den Kern dieses Abschnitts bildet die Lokale Spektrale Rekonstruktion (LSR). Die LSR ist ein iteratives Rekonstruktionsverfahren und liefert eine exakte Beschreibung der lokalen spektralen Eigenschaften des rekonstruierten spektralen CT-Datensatzes. Aus dieser Beschreibung lassen sich direkt lokale quantitative Größen für die abgebildete Anatomie ableiten. Mit Hilfe der LSR lassen sich somit verschiedene Anwendungen der QCT formulieren. Wir zeigen dies exemplarisch an einer quantitativen Strahlaufhärtungskorrektur, an einer Schwächungskorrektur für Positronen-Emissions-Tomographie und Einzelphotonen-Emissions-Tomographie und an einer Materialidentifikation.

Das letzte Themengebiet befasst sich mit der Rauschreduktion für QCT-Daten, die bei CT grundsätzlich mit Dosiseinsparung verbunden ist. Wir stellen zwei neuartige Rauschreduktionsverfahren vor: Zum einen eine bildbasierte Rauschreduktion auf Histogrammbasis, die explizit auf die Eigenschaften multispektraler CT-Daten zugeschnitten ist. Hier zeigen wir anhand synthetischer und realer Daten ein Rauschreduktionspotential von ca. $20\,\%$. Das zweite Verfahren ist ein nichtlineares Filter auf

Projektionsdaten, das ein punktbasiertes Projektionsmodell nutzt, um Strukturen in den Projektionsdaten zu detektieren und zu bewahren. Die hier gezeigte Realisierung stellt eine angepasste Variante des bekannten Bilateralfilters dar, bei dem das photometrische Ähnlichkeitsmaß durch ein strukturelles Ähnlichkeitsmaß ersetzt wird, das spezifisch für den CT-Abbildungsprozess ist. Die Eigenschaften dieses Filters werden an realen und synthetischen Daten untersucht. Dabei wird ein Rauschreduktionspotential von etwa 15 % für gemessene Patientendaten belegt.

Abstract

Computed Tomography (CT) is a wide-spread medical imaging modality. Traditional CT yields information on a patient's anatomy in form of slice images or volume data. Hounsfield Units (HU) are used to quantify the imaged tissue properties. Due to the polychromatic nature of X-rays in CT, the HU values for a specific tissue depend on its density and composition but also on CT system parameters and settings and the surrounding materials. The main objective of Quantitative CT (QCT) is measuring characteristic physical tissue or material properties quantitatively. These characteristics can, for instance, be density of contrast agents or local X-ray attenuation. Quantitative measurements enable specific medical applications such as perfusion diagnostic or attenuation correction for Positron Emission Tomography (PET).

This work covers three main topics of QCT. After a short introduction to the physical and technological basics for QCT, we focus on spectral X-ray detection for CT. Here, we introduce two simulation concepts for spectral CT detectors, one for integrating scintillation and one for directly-converting counting detectors. These concepts are tailored specifically for the examined detector type and are supported by look-up tables. They enable whole scan simulations about 200 times quicker than standard particle interaction simulations without sacrificing the desired precision. These simulations can be used to optimize detector parameters with respect to the quality of the reconstructed final result. The results were verified with data from real detectors, prototypes and measuring stations.

The second topic is QCT algorithms which use spectral CT data to realize QCT applications. The core concept introduced here is Local Spectral Reconstruction (LSR). LSR is an iterative reconstruction scheme which yields an analytic characterization of local spectral attenuation properties in object space. From this characterization, various quantitative measures can be computed. Within this theoretical framework, various QCT applications can be formulated. This is demonstrated for quantitative beam-hardening correction, PET and SPECT attenuation correction and material identification.

The final part is dedicated to noise reduction for QCT. In CT noise reduction is directly linked to patient dose saving. Here, we introduce two novel techniques: Firstly an image-based noise reduction based on joint histograms of multi-energy data-sets. This method explicitly incorporates the typical signal properties of multi-spectral data. We demonstrate a dose saving potential of 20 % on real and synthetic data. The second method is a non-linear filter applied to projection data. It uses a point-based projection model to identify and preserve structures in the projection domain. This principle is applied to a modified bilateral filter, where the photometric similarity measure is replaced with a structural similarity measure derived from this concept. We examine the properties of this filter on synthetic and real patient data. We get a noise reduction potential of about 15 % without sacrificing image sharpness. This is verified on synthetic data and real phantom and patient scans.

Acknowledgment

Table 1 lists three groups of people whose support made this work possible. The relations between these groups are qualitatively illustrated in Fig. 1. The most important supporters are listed here. Group membership is indicated in parenthesis:

1. Parents (A): Needless to say – without them I wouldn't have started this whole project (on many levels). Thank you for everything!

2. Supervisor (B): Thanks to Achim Hornegger for the infrastructure, the opportunity to visit some really interesting conferences, all the feedback and for forming the LME the way it is.

3. Supervisor (C): Thank you, Björn Heismann, for the great collaboration on a scientific and personal level. It was certainly a great to work with you.

4. Other proof readers (B): Thanks to Maria Polyanskaya and Konrad Sickel for finding many mistakes and improving the style. I promise not to blame you too excessively for the remaining typos.

5. Other LME staff (B): Thanks for the dynamic and inspiring working environment.

6. Siemens crew at the detector center (C): Special thanks to Daniel Niederlöhner for his scientific consulting and input and for contributing measurements. I would also like to thank Stefan Wirth, Edgar Kraft and Jürgen Leppert for their contributions and consulting.

7. Andreas Mahnken (no group): Thanks for the data / images and medical consulting.

8. Metrilus (D): Thanks Simon Placht and Christan Schaller for the patience, the company and especially for the things yet to come.

Michael

Id	Type	Main contributions
A	Friends and family	Financial support, motivation, spirit, distraction.
B	Pattern Recognition Lab crew	Great working atmosphere, many nice (non-)work related activities.
C	Siemens Healthcare	Financial support, measurement results, scientific consulting.
D	Metrilus GmbH	Experience, challenges, great alternative to becoming a member of group C.

Table 1: Supporting groups. Group B includes alumni.

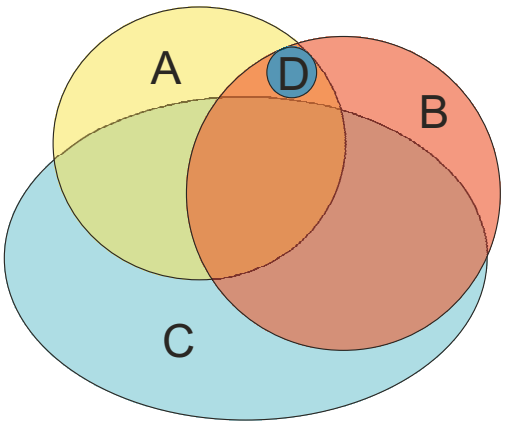

Figure 1: Diagram qualitatively indicates intersections between groups from Tab. 1.

Contents

1 Introduction **1**
- 1.1 Quantitative Computed Tomography and Spectral Detection 1
- 1.2 Structure of this Thesis 2
- 1.3 X-Ray Generation and Spectra 3
- 1.4 Detection Concepts 7
  - 1.4.1 Scintillation Detectors 8
  - 1.4.2 Semiconductor Detectors 11
- 1.5 Spectral CT Measurement 13
- 1.6 CT Measurement Process 15
  - 1.6.1 Physics of X-Ray Attenuation 15
  - 1.6.2 CT Reconstruction 19
  - 1.6.3 Beam Hardening 23
  - 1.6.4 Basic CT Calibration Steps 25
- 1.7 CT Image Quality Metrics 26
- 1.8 Scientific Contributions of this Work 29

2 Detector Simulation **31**
- 2.1 Simulation Concepts 31
  - 2.1.1 Monte-Carlo Simulation of X-Ray Detectors 31
  - 2.1.2 Look-Up Table-Based Detector Simulation 32
- 2.2 Integrating Scintillator Detectors 33
  - 2.2.1 Simulation Principles 33
  - 2.2.2 Simulation Workflow 34
  - 2.2.3 Results 41
- 2.3 Directly Converting Counting Detectors 43
  - 2.3.1 Simulation Principles 43
  - 2.3.2 Simulation Elements and Workflow 44
  - 2.3.3 Results 50
- 2.4 Conclusions 55

3 Quantitative CT **59**
- 3.1 Concepts of Quantitative CT 59
- 3.2 Basis Material Decomposition 60
  - 3.2.1 Projection Data-Based BMD 61
  - 3.2.2 Image-Based BMD 62
- 3.3 Local Spectral Reconstruction 63

3.3.1 Concept of Local Spectral Weighting . . . 63
3.3.2 Theory . . . 63
3.3.3 Materials and Methods . . . 71
3.3.4 Results and Discussion . . . 73
3.4 Conclusions . . . 82

4 Dose Reduction **85**
4.1 Noise Reduction in CT . . . 85
4.2 Value-based Noise Reduction for Multi-Energy CT . . . 86
4.2.1 Method . . . 87
4.2.2 Evaluation and Results . . . 91
4.3 Ray Contribution Masks for Iterative Structural Sinogram Filtering . 98
4.3.1 Theory of Structure Aware Filtering . . . 99
4.3.2 Materials and Methods . . . 105
4.3.3 Evaluation and Results . . . 108
4.4 Conclusions . . . 113

5 Summary and Outlook **115**

List of Figures **119**

List of Tables **125**

Bibliography **127**

Chapter 1

Introduction

Computed Tomography (CT) is a widespread modality in diagnostic medical imaging as it offers a fast and detailed insight into the patient's anatomy. This work is dedicated to Quantitative Computed Tomography (QCT). This branch of CT applications broadens the fields of application for CT by providing real quantitative information on the scanned anatomy. Standard single-energy CT reconstruction assumes mono-energetic radiation, however, common X-ray sources for medical CT are polychromatic. QCT algorithms take this property into account to provide quantitative information on tissue composition. With this extra data, functional imaging applications or material identification becomes possible for CT. Within the scope of this work, several novel techniques have been developed that cover the full range of quantitative CT data processing from multi-spectral X-ray detection over quantitative CT reconstruction to specialized signal enhancement techniques for QCT applications. This introductory chapter provides the fundamentals of Quantitative CT and spectral detection whereas the following chapters mostly focus on novel QCT methods developed within the scope of this theses. The following section introduces the general concepts of Quantitative CT and gives a detailed overview of the structure of this work.

1.1 Quantitative Computed Tomography and Spectral Detection

Traditional CT measures the spatial distribution of the X-ray attenuation of an object. The X-ray attenuation of a material is energy dependent, at specific energies it is governed by the composition of the material, more precisely on its mass density and the atomic number and composition of its elements. A common measure for X-ray attenuation in medical CT is the Hounsfield Unit (HU). It is normalized to the attenuation of water so that water gets the value 0 HU in a CT dataset, while air gets -1000 HU. This normalization suggests a certain level of quantitativity of the HUs, but in fact the HU value of a material other than water and air in a CT scan depends on the system design and settings of the CT device as well as the characteristics of the complete scanned object. This dependency is caused by the non-linear attenuation characteristics of polychromatic radiation.

The basics of CT X-ray measurement and its properties are covered in the following sections of this chapter. Here, X-ray tubes and detection principles are discussed, the physical processes behind X-ray attenuation and measurement are introduced. The last part gives a short overview on the most important quality metrics for the acquired signals and shows how these metrics can be computed.

The term *Quantitative Computed Tomography* refers to one common property of all QCT-methods: Their result values should be solely dependent on the material properties. This problem cannot be generally solved with standard mono-energetic CT measurements since the reconstruction problem cannot be solved analytically for a single measurement with polychromatic sources. Spectral input data is required, i. e. multiple measurements with different spectral characteristics are made for each projection ray. Most quantitative CT algorithms require two spectral measurements (e. g. [Alva 76]), for several scenarios more measurements are needed [Schl 08]. *Dual Energy CT* (DECT) measures two image-sets at different energy weightings, e.g. by performing two scans with tube voltages set to 80 kVp[1] and 140 kVp respectively. The output quantities of these algorithms differ with respect to the diagnostic demands: They range from energy-normalized attenuation values over physically motivated quantities like density and effective atomic number to spatial distributions of whole attenuation spectra. Other QCT applications use the quantitative information to support algorithmic post-processing of CT or Positron Emission Tomography (PET)/ Single Photon Emission Computed Tomography (SPECT) data. The most popular current Dual Energy CT diagnostic applications are bone removal [Zhen 08], PET/SPECT attenuation correction [Heis 09], lung perfusion diagnostic or quantification of contrast agent concentrations, for instance in the myocard.

1.2 Structure of this Thesis

Spectral X-ray detection techniques and their simulations are described in Chapter 2. It introduces special simulation approaches for two CT detection concepts: The most common standard approach of energy-integrating scintillation detectors and a more experimental one which has not yet reached commercial medical CT: Counting semiconductor detectors.

Chapter 3 introduces QCT algorithms that process the spectral measurement values: The first part focuses on general concepts of QCT algorithms, then *Basis Material Decomposition* is introduced, which is an important basis for many QCT methods. The last part gives an insight into the newly developed *Local Spectral Reconstruction* algorithm. It models the spectral properties of CT measurement and reconstruction and provides a unified framework for many QCT applications such as beam hardening correction, energy normalization and material identification.

Since QCT methods require spectral input data, the signal processing differs much from standard CT, for instance special reconstruction techniques are applied. Of course, the patient dose of a QCT examination should not greatly exceed the dose of

[1]The peak acceleration voltage of X-ray tubes is usually given in kVp (*kilovolt peak*). An acceleration voltage of 120 kVp results in a X-ray spectrum where the individual photon energies are distributed in the range from 0 to 120 keV. Kiloelectronvolts (keV) are a common measure for the kinetic energy of the accelerated electrons. Section 1.3 gives an overview on X-ray generation.

a comparable standard CT examination. Several common QCT methods, however, are prone to measurement noise which leads to poor signal quality in the quantitative output values. Consequently, specifically adapted signal improvement techniques have to be applied to get the maximum signal quality. These methods should take the properties of spectral data into account. Chapter 4 explains two novel signal enhancement algorithms for CT: The first one is a purely histogram-based post-reconstruction approach explicitly dedicated to spectral data, the second one is an edge-preserving general purpose CT projection data-filter that uses a projection model to merge the benefits of projection-based and image-based approaches.

Chapter 5 summarizes the results presented in this work and gives an outlook on possible further research directions on QCT.

1.3 X-Ray Generation and Spectra

In the following sections the basics of CT systems and data acquisition are discussed. This work focuses on third generation CT set-ups with a rotating X-ray source and an arc-shaped detector in a gantry (see Fig. 1.1). The following descriptions assume a world coordinate system (CS) with the origin in the center of rotation. For the detector descriptions a commonly used detector coordinate system is used: Its z-coordinate has the same direction as in the world CS, and the ϕ-coordinate points along the detector arc.

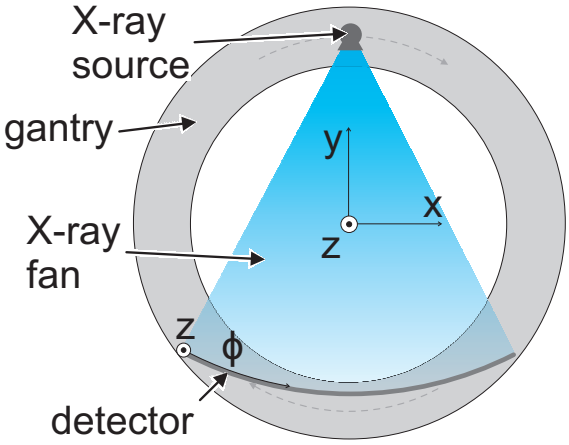

Figure 1.1: Third generation CT layout with rotating X-ray source and a single-row detector. The arrows annotated with (x, y, z) indicate the world coordinate system and the (ϕ, z)-arrows indicate the detector coordinate system. The symbol $\odot$ indicates an arrow pointing perpendicularly outwards the paper or display plain towards the reader.

X-ray Tubes

Medical CT systems use X-ray tubes to generate X-rays. Figure 1.2a shows a basic set-up of an X-ray tube. A cathode emits electrons which are accelerated by an electrical field. The strength of the electrical field and hence the energy of the electrons

are determined by the *tube voltage*. The electron beam hits an anode in which the electrons are slowed down and Bremsstrahlung is emitted. Additionally, inner-shell electrons of the atoms in the anode material are hit by high-energy free electrons and ejected from the atom. This leaves the ionized atom in an excited state. The electron hole is filled by an electron transition from a higher orbital to the lower one with the hole. These transitions cause the emission of photons of discrete characteristic energies. The emitted spectrum is referred to as *characteristic spectrum*. The resulting tube spectrum is a mixture of the Bremsstrahlung-spectrum and the characteristic spectrum.

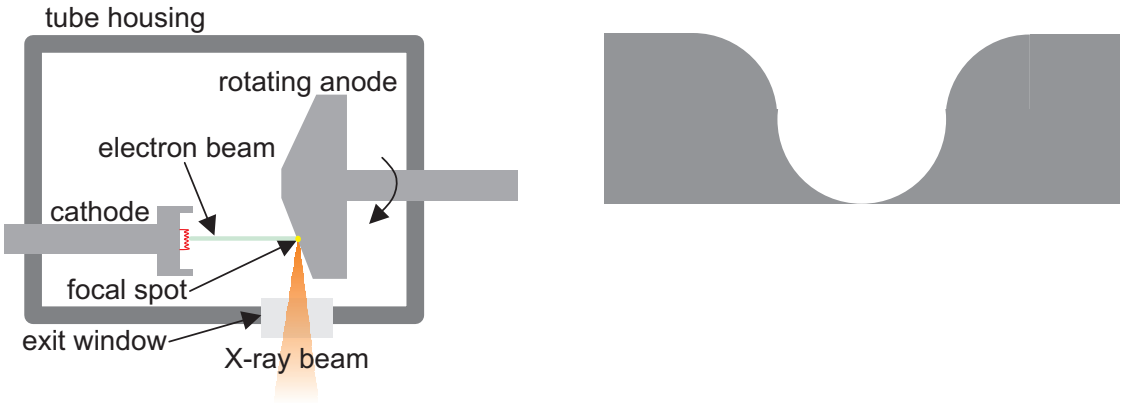

(a) Basic layout of a CT X-ray tube.

(b) Possible wedge filter shape.

Figure 1.2: Tube model and wedge filter.

The materials used for the anode are combinations of tungsten, rhenium and / or molybdenum because of their heat resistance and high density. Most of the energy consumed by the tube is converted into heat, only less than 1% of the energy is emitted in form of X-rays [Beut 00]. Several tube designs were introduced in order to reduce the heat-induced wear and tear of the anode. *Rotating anode tubes* represent the most common tube design in CT systems. CT systems have to support high tube voltages and have to deliver high tube currents compared to other medical X-ray imaging modalities, so the X-ray tubes need to deal with high peak power and also high sustained power as continuous scans, for instance helical CT acquisitions, demand long duty cycles of the X-ray tube.[2] The tube design has to ensure a very efficient cooling of the anodes. Due to the rotation of the anode, the electron beam distributes its energy on circlular focal path instead of dissipating its energy in a single spot of the anode material.

The focal spot of a CT tube has a certain extent which depends on several parameters. Generally, its size increases with higher tube current. Larger focal spot sizes decrease the image quality as this causes a blurring of the projection signal. The

[2]The typical peak electrical power of a CT X-ray tube can exceed 100 kW.

intensity profile of the focal spot can, for instance, be approximated by a Cauchy distribution[3] with a full-width half maximum (FHWM) in the range of 1 to 2 mm.

Figure 1.4a shows a typical tube spectrum for a tungsten tube at a tube voltage of 120 kV. Tube voltage settings for medical CT range from about 60 kVp to 150 kVp. The intensity of the X-ray beam can be adjusted with the tube current setting. Modern CT tubes can deliver tube currents up to 800 mA. The acceleration voltage is the most important parameter regarding the shape of the spectrum of Bremsstrahlung. Other influences such as anode material, tube model, tube current and wear and tear [Erdl 09] have additional minor influences. The peak locations of the characteristic spectrum depend on the target material and the transition energies between its electron shells[4]. The visible peaks in Fig. 1.4a correspond to the transition energies for tungsten. The larger peak resembles the Kα_2 and Kα_1 transition between the K and the L_2 / L_1 shell at 57.99 keV and 59.32 keV. The smaller peak is caused by the Kβ_1 and Kβ_2 transition between the K and the N_3 / N_2 shell at 67.25 keV and 69.07 keV [Lass 99]. Tube spectra are modeled using Monte Carlo simulations of particle interactions such as *Geant* [Agos 03, Alli 06], measurements [Aich 04] or hybrid approaches [Tuck 91].

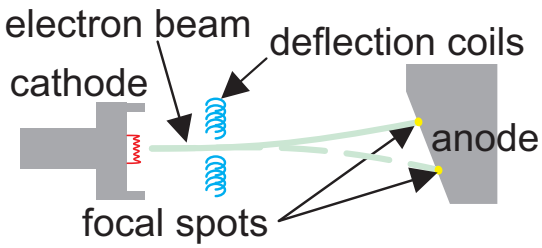

Figure 1.3: Schematic illustration of an X-ray tube with single FFS. The two dots on the anode represent the alternating focal spot positions. The deflection coils force the electron beam to alternate between to trajectories indicated by the hatched and solid line.

Some CT X-ray tubes have the possibility to deflect the electron beam in various directions at very high frequencies. This is schematically illustrated in Fig. 1.3. This way, multiple alternating focal spot positions can be achieved. This technique is called *flying focal spot* (FFS) [Kach 04]. This kind of super-sampling can be used to increase the maximum possible resolution for a given detector sampling distance. An FFS along the patient axis (z-axis) is called z-FFS. It increases the inter-slice resolution. The perpendicular ϕ-FFS increases the intra-slice resolution. Each combination of FFS modes has to be incorporated into the reconstruction algorithms.

[3]Determined by applying the distribution fitting program *EasyFit* (MathWave, Dnepropetrovsk, Ukraine) to a measured tube profile.

[4]The electron configuration of atoms is described by the atomic shell model. An overview on theories of atomic shell models is given in [Gree 09].

Tube Pre-Filters

Low energy X-rays are usually absorbed almost completely in the body and therefore do not contribute to the signal but would increase X-ray dose. Additional pre-filters are applied at the exit window of the tube to eliminate low energy X-rays. Typically these filters consist of up to two millimeters of titanium and/or aluminum (see Fig. 1.4a for an example spectrum).

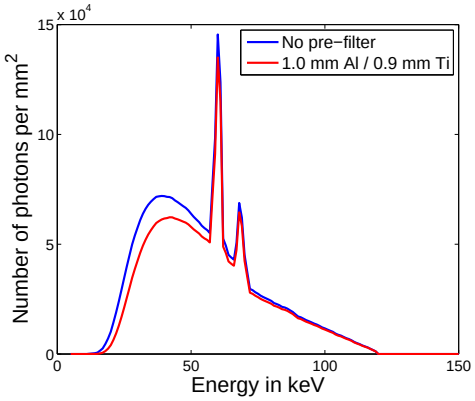

(a) Spectrum of a tungsten tube at 120 kVp acceleration voltage with and without filter.

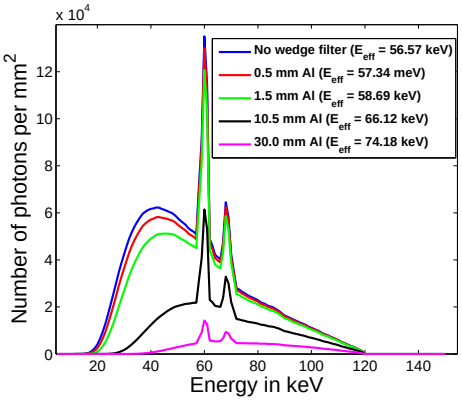

(b) Filtered 120kVp tube spectrum for various wedge filter thicknesses.

Figure 1.4: Tube spectra with and without pre-filtering. Tube spectra generated with *drasim* (by Karl Stierstorfer, Siemens AG, Forchheim). The spectral attenuation coefficients were taken from the XCOM database of photon cross sections [Berg 98].

When scanning the human body, in most situations the center rays of an X-ray fan-beam have to pass through more matter than the outer rays and are attenuated much stronger, so more dose is required in the center. A so called bow-tie or wedge filter is used to shape the intensity of the fan beam accordingly. It typically consists of an aluminum slab with a central round cavity. Figure 1.2b shows a possible layout of such a filter. At the edges, the wedge filter can reach a thickness of approx. 3 cm whereas there is almost no filtering in the center. Figure 1.4b shows examples how the pre-filtered tube spectrum from Fig. 1.4a is modified by passing through differently thick parts of an aluminum wedge filter[5]. The corresponding effective energies E_{eff} become larger with increasing attenuation. E_{eff} is the centroid of the respective spectrum. This effect is called *beam-hardening*. It is a side-effect of the wedge filter which makes the characteristics of the X-ray spectrum inhomogeneous throughout the X-ray fan [Mail 09]. This has to be taken into account when designing spectral CT applications.

A third category of tube filters also plays a specific role in Dual Source CT devices such as the Siemens Definition Flash (Siemens AG, Forchheim, Germany). It employs two tube-detector pairs and produces two measurements simultaneously at different tube voltages. For quantitative CT applications with Dual Source data it is desirable

[5]The attenuation coefficients for computing attenuated spectra are taken from the NIST XCOM database of photon cross sections. It is available at `http://www.nist.gov/pml/data/xcom/index.cfm`

to use two spectra with as little overlap as possible in order to ensure the maximal spectral separation between the two acquired datasets. For this task, usually the two tubes are operated at two different kVp settings. Additionally, a special filter can be used to attenuate the lower energy components in the high energy tube spectrum. In practice, a thin tin filter is used. Figures 1.5a and 1.5b compare two pairs of 80 kVp and 140 kVp spectra with and without tin filter and the respective relative overlaps. The spectral separation is clearly improved as the low energy components of the 140 kVp spectrum are effectively suppressed by the tin filter.

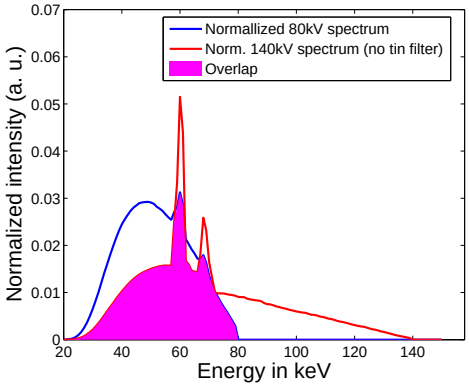

(a) Normalized 80 kVp and 140 kVp tube spectra with overlap.

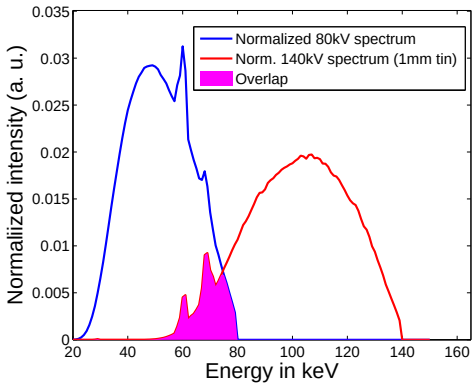

(b) Spectral overlap for normalized 140 kVp tube spectrum with 1 mm tin filter.

Figure 1.5: Spectral overlap without and with tin filter (data from *drasim* by Karl Stierstorfer, Siemens AG, Forchheim). The intensities are displayed in arbitrary units (a. u.).

1.4 Detection Concepts

Detectors are used to convert the incoming attenuated X-ray radiation into an electric (digital) projection signal which is then reconstructed to a 2-D or 3-D distribution of local object attenuation values. CT detectors are usually equipped with an anti-scatter grid (collimator) that blocks scattered radiation, i.e. X-ray photons with a trajectory other than the direct line from the X-ray source to detector pixel. It is made from a very dense material like tungsten. For standard CT reconstruction algorithms, scattered X-ray quanta do not contribute to the usable signal and reduce the signal quality.

CT X-ray detectors can be distinguished by their working principle (scintillation detectors and semiconductor detectors) and the type of output signal (integrating and counting detectors). Table 1.1 gives an overview of the fields of application of these detectors. Figure 1.6 illustrates the different signal generation principles for an idealized case with optimal integrating and counting detectors at a very low X-ray flux: Ideal integrating detectors yield a signal that is directly proportional to the complete incoming X-ray energy which is the sum of all X-ray quanta weighted with their respective energy (Fig. 1.6b). A counting detector may distinguish incoming

quanta with respect to their energy. In practice, a counting detector is provided with several energy thresholds and yields the number of detected quanta above or between the thresholds. This results in multiple output signals for a single measurement. An example signal for one threshold is shown in Fig. 1.6c. Here we assume each X-ray photon deposits its complete energy in one interaction event and each interaction event is observed instantaneously. Effects of practical systems such as noise or low-pass characteristics of the detection process are neglected for the sake of simplicity. Realistic system responses are considered in Chapter 2 which is dedicated to the simulation of detector systems.

Working principle / Output type	**Integrated energy**	**Photon counts**
Scintillation	CT, Digital Radiography	PET / SPECT
Direct conversion	Mammography (a-Se)	CT (experimental), PET, SPECT [Shar 08]

Table 1.1: X-ray detector types and typical fields of application. The abbreviation *a-Se* refers to amorphous selenium detectors.

1.4.1 Scintillation Detectors

Integrating scintillation detectors are the current state of the art technology for medical CT systems. Figure 1.7a shows a basic layout of the detector. The detector converts the measurements of the intensity of attenuated X-rays to a digital signal which is then transmitted from the rotating gantry to the *image reconstruction system* (IRS) using slip rings.

The incoming X-rays are first absorbed by the scintillation crystal. The absorbed energy is emitted as visible light. The visible light is then detected by the photodiode layer and converted into an electrical signal. Materials used for the scintillation crystals in CT are cadmium tungstate ($CdWO_4$) or gadolinium oxysulfide doped with praseodymium (Gd_2O_2S:Pr or GOS, see Fig. 1.7b). The scintillation crystal is divided up into small blocks which correspond to the detector pixels. The gaps between the blocks are called septa. These are filled with a highly reflective material like titanium dioxide (TiO_2) that prevents optical light from entering the scintillator crystal that corresponds to another pixel. The top of the scintillator is also coated with a reflective material.

The scintillation crystal has to fulfill several criteria in order to be qualified for medical CT applications: The necessary frame rates of well over 1000 frames per second require a sufficiently small decay time, otherwise portions of the signal from one temporal sample would be present in following sample. This causes a smearing of the signal over time and thus decreases signal quality. Materials with high atomic numbers have to be used, since the X-ray absorption of the material has to be sufficiently high, so that most incoming X-ray photons interact within a thin scintillator layer.

The electrical current from the photodiode is integrated over a given amount of time. At the end of the integration period, the resulting charge is read-out and the

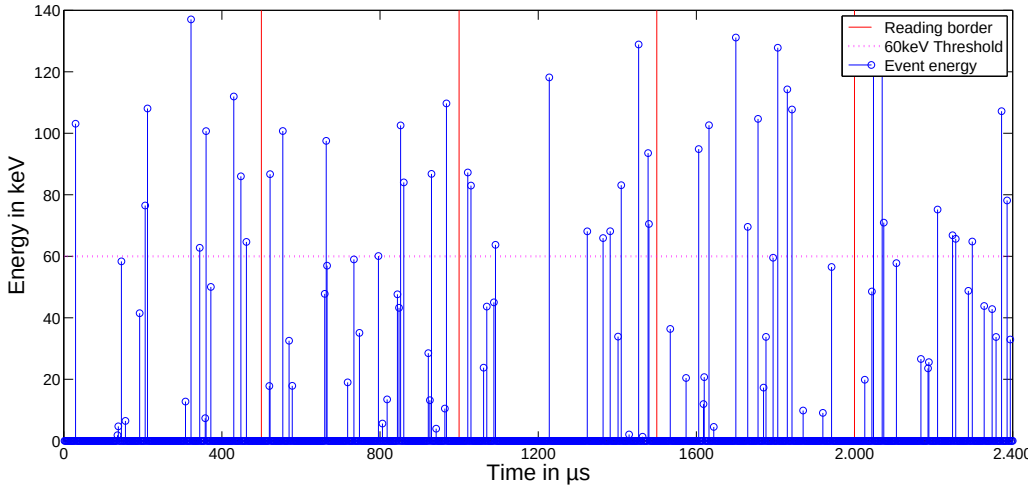

(a) Sample signal of interaction events within one detector pixel over time. The term *event* refers to any interaction of an X-ray quantum with the detector material.

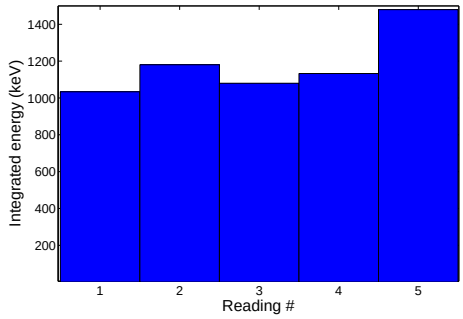

(b) Output signal for ideal energy integration.

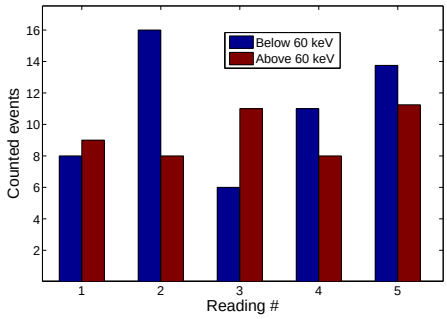

(c) Output signal for ideal event counting.

Figure 1.6: Sample output signals for ideal energy integration and ideal photon counting for synthetic input signal of randomly distributed interaction events at different energies.

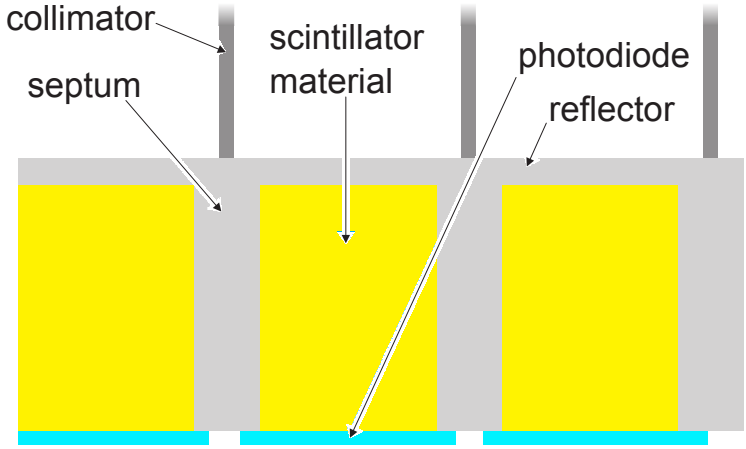

(a) Basic layout of a scintillator as used in CT.

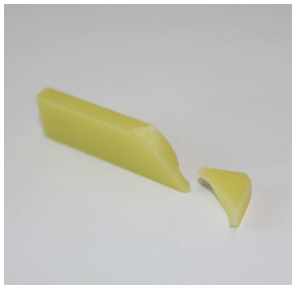

(b) Gadolinium oxysulfide doped with praseodymium.

Figure 1.7: Scintillation detectors.

next integration period starts. One integration time plus the read-out time is called a *reading*. The typical amount of readings per gantry rotation is about 1000 if no FFS is used. If the rotation period is 0.5 s, the reading time corresponds to approximately 500 μs.

The integrated signal from the photodiodes is amplified, digitized and processed by an *analog-to-digital converter* (ADC). The dynamic range of the detected signal is very large and the amount of data that has to be transferred from the gantry should be kept small. In order to reduce the quantization noise, the detector ASIC (*application specific integrated circuit*) logarithmizes the signal and transforms it to a pre-defined data-range during quantization before the signal is transmitted to the IRS. These computations on the detector ASIC reduce the required datarate for the transfer of the measurements from the gantry to the IRS.

Since one reading time comprises thousands of X-ray interaction events, the individual events cannot be resolved in the output signal. The output signal corresponds to the total detected energy of all incoming X-ray photons during one reading. Figure 1.8 shows the typical energy sensitivity of such a detector system. For low energy photons it is rather linear as the amount of optical photons generated in the scintillator is linearly dependent on the energy of an incoming X-ray photon. The step at approx. 50.2 keV corresponds to the K-edge of gadolinium. At this point the energy of the incoming X-ray photons is sufficient to eject inner-shell electrons from the K-shell of the gadolinium atom. The average depth of interaction decreases due to increased photoelectric absorption, causing more optical photons to be generated further away from the photodiode, resulting in a higher signal loss. At very high energies around 100 kV and above, the spectral sensitivity drops, as the absorption of high energy photons decreases and an increasing amount of photons passes through the detector without interacting with the scintillator material. Section 2.2 introduces a concept for efficiently simulating these detectors and gives a detailed analysis of their properties.

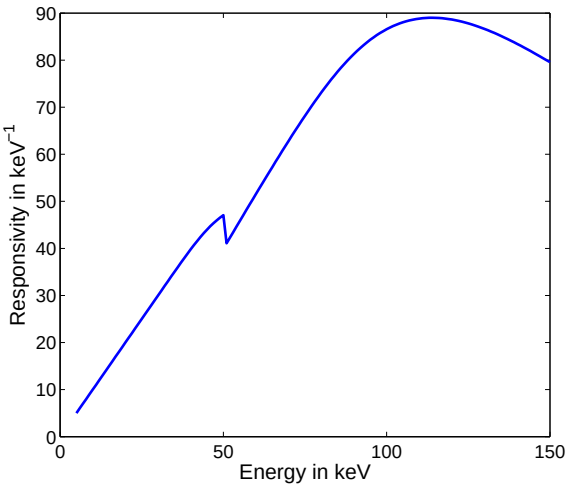

Figure 1.8: Detector responsivity $D(E)$ for a 1.4 mm Gd_2O_2S scintillator CT detector [Heis 08]. This is the relative detector output signal strength for a detected quantum of given energy.

1.4.2 Semiconductor Detectors

Figure 1.9 displays the basic layout of a semiconductor detector. The principle of counting detectors for medical CT applications was originally introduced in 1998 [Fisc 98]. Since then, an increasing amount of publications and prototype systems has shown the potential of directly-converting counting detectors for X-ray imaging modalities like Computed Tomography and others. Some of the most renowned are the Medipix [Camp 98] / Medipix2 [Llop 01, Tlus 06], the PILATUS [Schm 04] or the CIX detector [Kraf 07]. The latter represents a combined integrating/counting detector concept. In combination with room-temperature semiconductors like cadmium telluride (CdTe) or cadmium zinc telluride (CdZnTe or CZT) these detector systems benefit from accessing the spectral information of photons and superior low-signal properties. The cathode and the pixelized anodes produce an electric field in the semiconductor material. The signal generation from the X-ray photons to final counts can be divided into three different stages:

1. Interaction of photons inside the sensor material and deposition of charges.

2. Motion of the charges towards the electrodes and thereby inducing electric signals.

3. Amplifying and counting inside the electronics.

Unlike standard scintillation detectors, semiconductor detectors can be used for photon counting in CT. Their decay time is sufficiently low and a high readout frequency of the signal compared to the frequency incoming X-ray photons can be chosen, so it is possible to identify individual X-ray interactions. Figure 1.10 illustrates this property for two different integration times. The frequency of X-ray interactions within a detector pixel is dependent on the X-ray flux (X-ray energy per unit area

and time) and the pixel area. Semiconductor detectors offer the necessary properties: The shaping width of the signal of an individual event can be adjusted to a few nano-seconds and low signal cross-talk between pixels allows for pixel areas below $0.05\,\mathrm{mm}^2$ [Bald 09].

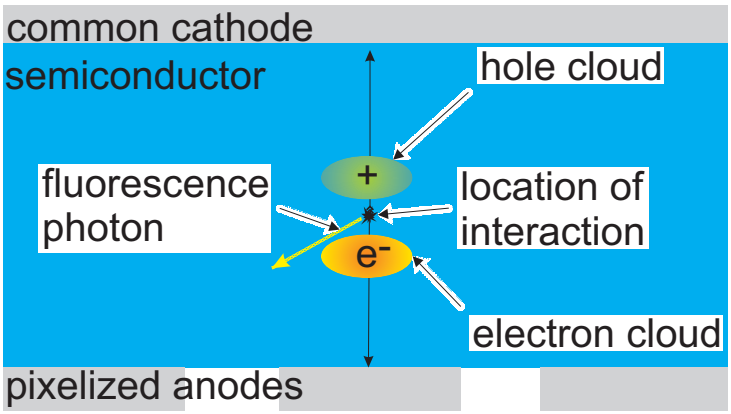

Figure 1.9: Basic layout and working principle of a directly converting semiconductor detector.

Section 2.3 contains an in-depth analysis of the signal properties of a practical counting semiconductor detector concept and introduces a simulation concept for this detector type.

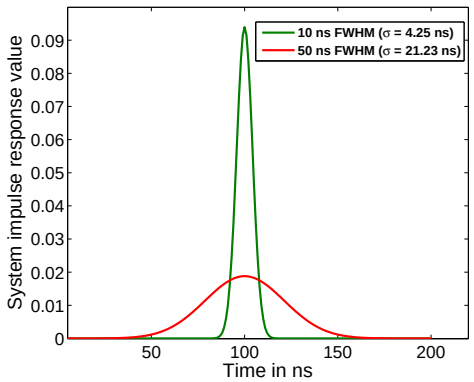

(a) Linear system impulse response function examples.

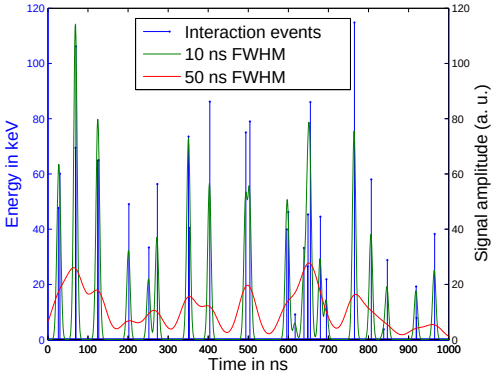

(b) Example input signal with evenly random distributed events and resulting signals.

Figure 1.10: Output signals for two different Gaussian impulse responses with FWHM 10 ns and 50 ns. In the 10 ns signal most of the pulses remain distinguished and their locations and pulse heights can be recovered by a suitable discriminator. The 50 ns signal does not show this property, so it is only suited for energy integrating detection. The average frequency of events in the input signal is 50 MHz.

1.5 Spectral CT Measurement

Spectral CT detection refers to producing multiple measurements of the same object with different spectral weightings. The spectral weighting is defined by the tube spectrum and the spectral sensitivity of the detector. In spectral detection techniques one of these or both are changed between measurements. The spectral weightings should have as little overlap as possible. This enhances the discrimination between the spectral measurements which is beneficial for QCT algorithms.

Usually only two spectral measurements are created due to dose limitations and the fact that most quantitative CT algorithms do not benefit from additional spectral measurements. This fact can be attributed to the specific attenuation properties of body materials in the CT energy range (see Sec. 1.6.1).

Dual kVp: The easiest method for producing spectral measurements is called *Dual kVp* [Kelc 79]. For this method two subsequent CT scans are performed at different tube voltages, e.g. 80 kVp and 140 kVp. No special equipment is needed for this method. In medical CT, this method is prone to motion artifacts as the alignment of the two datasets cannot be ensured due to patient motion in-between the two scans. However, this can be a valid method for evaluating quantitative CT algorithms on phantom data.

Dual Source: *Dual Source CT* is similar to dual kVp with the two CT scans being performed simultaneously by a special CT system. In this system, the gantry houses two tube-detector pairs A and B with a fixed angular offset (see Fig. 1.11). The two X-ray tubes are operated at different tube voltages. Flohr et al. have presented an evaluation of one of the first commercially available medical Dual Source systems in [Floh 06]. More recent systems offer an optional tin filter on one tube to increase spectral separation (see Fig. 1.5) whereas the two detectors are usually identical in terms of spectral sensitivity. Most available systems, however, use differently sized detectors due to space restrictions within the gantry. So the measurements of the smaller detector offer a limited *field of view* (FOV). The data from the larger detector can be used to compensate for truncation artifacts in the reconstruction but Dual Energy data is only available for the smaller FOV. Since the two tube-detector pairs are operated simultaneously, scatter radiation from tube A impairs the signal of detector B and vice versa. This is a major drawback of this technology, as this property decreases signal quality and leads to an increased patient dose.

KVp-switching: *KVp-switching* is another tube-based approach that switches the tube voltage between two readings (see [Zou 08] and [Xu 09]). As reading times are typically in the range of hundreds of micro-seconds, a special tube capable of changing the tube voltage very quickly is required. Due to dose efficiency, the tube current should also be adjusted for different kVp-settings as the attenuation properties of human body tissue are very different for different X-ray energies. The projections acquired with this approach are not perfectly aligned as the projections are interleaved. Missing projections have to be interpolated.

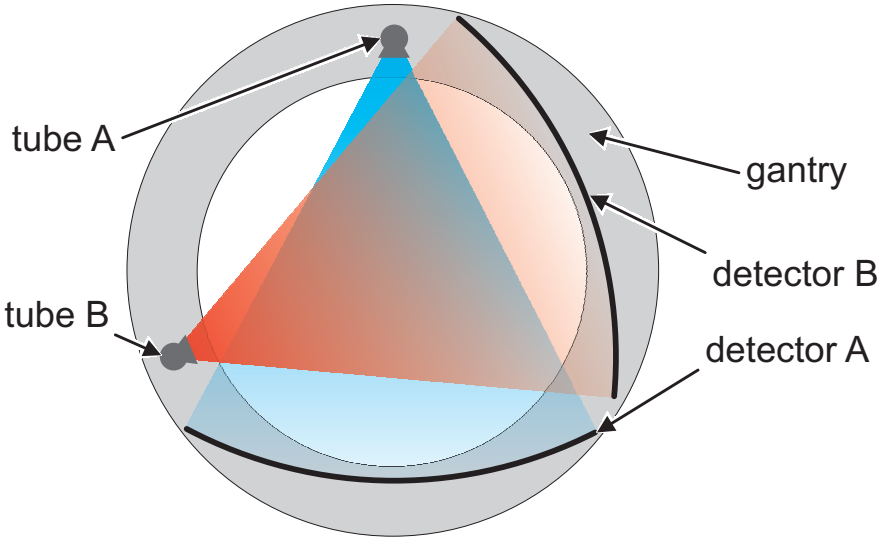

Figure 1.11: Concept of Dual Source CT.

Dual layer detectors: This technology uses a variation of the detector spectral sensitivity to produce measurements at different energy weightings. Two scintillation detector layers are stacked upon each other and the top detector layer is a pre-filter for the lower one. This technology is also referred to as *sandwich detector*. Figure 1.12 shows a possible realization of this concept. The detector efficiency is lowered, as the top layer photodiodes and wiring absorb parts of the X-rays and escape photons may enter the other layer and impair the energy separation of the layers [Kapp 09a].

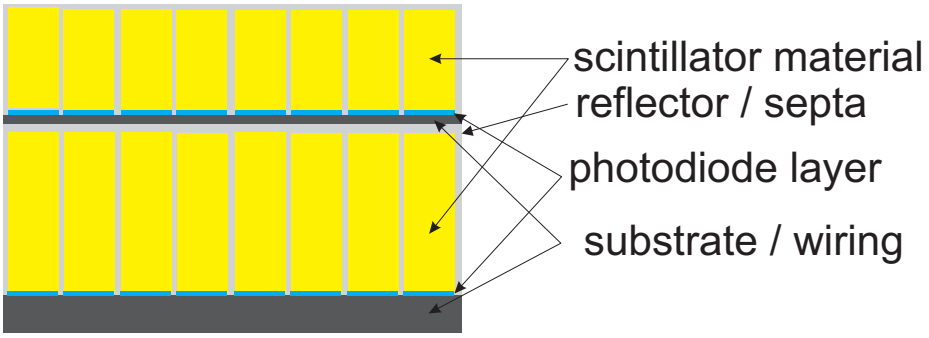

Figure 1.12: Concept of a dual layer detector.

Counting detectors: Spectral measurements can be conducted with counting detectors by using multiple energy-thresholded photon counts. Theoretically, X-ray counting for medical CT can be performed with scintillators and semiconductor detectors. As semiconductor detectors have the advantage of being very fast and having very limited cross-talk between channels, a lot of effort has been put in evaluating the suitability of these detectors for medical CT. However, still some issues have to be resolved before this technology becomes commercially available in medical CT scanners. Counting detectors perform especially good at low X-ray flux, at high

flux levels, which typically appear in medical CT, several problems arise: Signal saturation prevents distinction of individual detection events and polarization of the semiconductor material affects the signal quality.

Due to physical effects, material defects and technical limitations the discrimination of X-ray quanta cannot be perfect. This leads to a limited spectral separation between the spectral sensitivities for each threshold signal which is dependent of the incoming X-ray flux. Figure 1.13 shows spectral sensitivities for thresholds producing photons counts below and above 60 keV at low X-ray flux and their overlap for a 140 kVp tube spectrum.

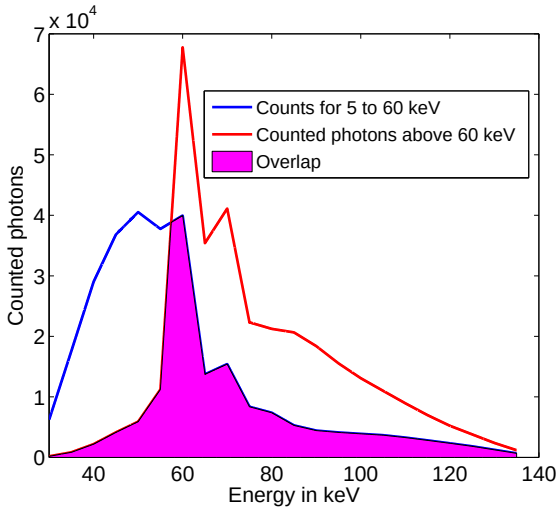

Figure 1.13: Spectral sensitivity example for a counting semiconductor detector with thresholds set to 5 keV and 60 keV. Due to several effects like cross talk, escape photons and signal pile-up, the spectral separation is reduced by a considerable overlap of the sensitivity curves. This example was generated using *SimSD* [Bald 09].

This section only lists the most common methods for multi-energy data acquisition. Alternative methods have been published, for instance, Rutt and Fenster [Rutt 80] present a split-filter approach. For this method, one half of the fan- / cone-beam is filtered differently. The two detector halves produce signals with different energy weightings. These methods are not commonly used in practical CT, so they are not considered here.

1.6 CT Measurement Process

1.6.1 Physics of X-Ray Attenuation

Physical effects

When X-rays pass through matter, a fraction of the X-ray quanta is absorbed and / or deflected from the original path. This process is called *attenuation*. Different physical effects contribute to the total attenuation. The individual contributions of these effects are non-deterministic and depend on the energy of the X-ray quanta. The following types of interaction of radiation with matter are known:

- Coherent (Rayleigh) scattering
- Incoherent (Compton) scattering
- Photoelectric absorption
- Pair production (in nuclear field and electron field)

The attenuation of a material is defined by its atomic composition and the mass density of the elements. Figure 1.14 shows the mass attenuation function $\left(\frac{\mu}{\rho}\right)(E)$ of water over energy E. Here, μ denotes the attenuation function and ρ the mass density. This quantity is dependent on the effective atomic number Z_{eff} of the material. The mass attenuation function of water is plotted over a very large range of energies on a logarithmic scale. The individual contributions of all the effects introduced above are also shown. The relevant energy range for medical CT from approximately 30 keV to 150 keV is marked by the vertical bar. The only two major contributors to the attenuation function in this range are incoherent (Compton) scattering and the photoelectric absorption. Figure 1.14b shows only those two components in the energy range of CT on a linear scale. In this range, Compton scattering is almost constant with respect to energy whereas the photoelectric absorption asymptotically approaches zero towards the upper bound of the energy range.

Figure 1.15 shows the mass attenuation of selected elements and its two major components incoherent scattering (Fig. 1.15a) and photoelectric absorption (Fig. 1.15b). The selection covers a wide range of atomic numbers. The photoelectric absorption shows a large variation with respect to the atomic number Z and the X-ray energy. For high-Z materials like tungsten or lead, a K-edge is present, as the relevant transition energies between the K-shell and other shells lie within the CT energy range. This causes the discontinuities in the tungsten and lead lines of Figs. 1.15b and 1.15c. For elements with lower atomic numbers these transition energies are below 30 keV and therefore no such discontinuities are visible. Compared to photoelectric absorption, the dependence on the atomic number is smaller for incoherent scattering.

Spectral Attenuation Coefficient

The *spectral attenuation coefficient* $\mu(E)$ expresses the total attenuation of a material with respect to energy. The mixture rule [Hubb 69, McCu 75] allows to approximate the mass attenuation function $\left(\frac{\mu}{\rho}\right)(E)$ of a material with errors below one percent for the CT energy range. For a material M consisting of N elements with the elemental mass attenuation functions $\left(\frac{\mu}{\rho}\right)_i(E)$, atomic mass Z_i and relative frequency r_i of the element in the compound for $i = 1$ to N, the mixture rule reads as follows:

$$\left(\frac{\mu}{\rho}\right)^{(\mathrm{M})}(E) = \frac{1}{\sum_{i=1}^{N} r_i Z_i} \cdot \sum_{i=1}^{N} r_i Z_i \cdot \left(\frac{\mu}{\rho}\right)_i(E). \tag{1.1}$$

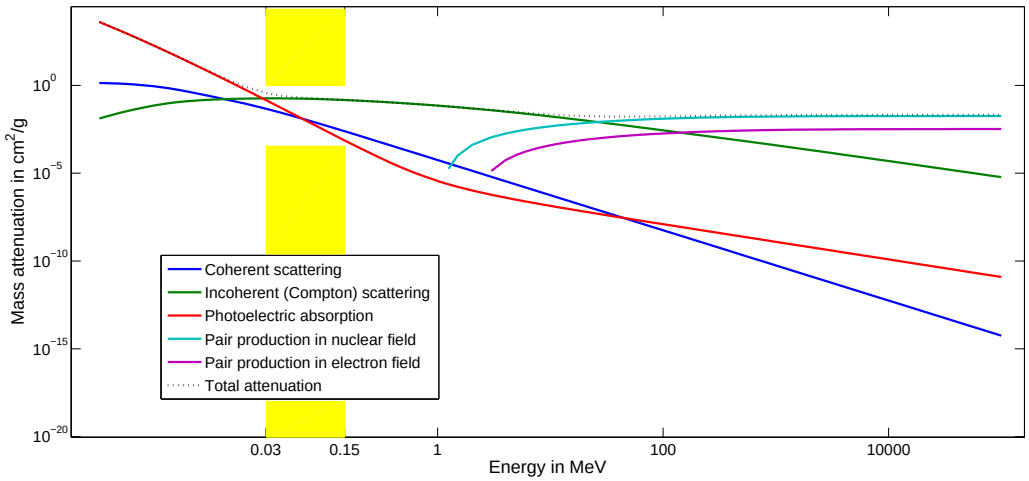

(a) Mass attenuation of water (yellow bar marks energy range of medical CT).

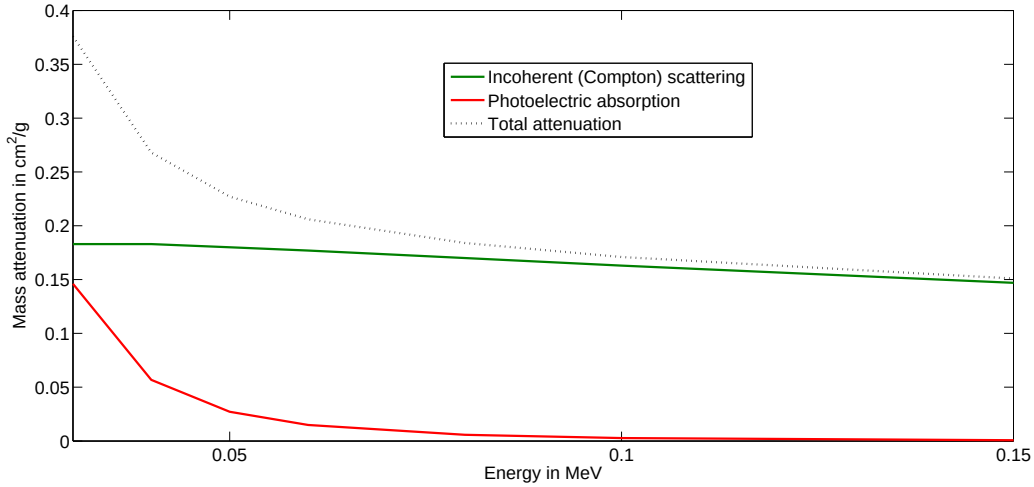

(b) Mass attenuation of water in the CT energy range.

Figure 1.14: Mass attenuation function of water and its contributions. Data taken from XCOM database [Berg 98].

For water (H_2O) with $Z_H = 1\,u$ and $Z_O = 16\,u$ we get the following mass attenuation[6]:

$$\left(\frac{\mu}{\rho}\right)^{(H_2O)}(E) = \frac{1}{2+16} \cdot \left(2 \cdot 1 \cdot \left(\frac{\mu}{\rho}\right)^{(H)}(E) + 1 \cdot 16 \cdot \left(\frac{\mu}{\rho}\right)^{(O)}(E)\right). \tag{1.2}$$

The spectral attenuation coefficient $\mu_M(E)$ of a material is obtained as follows:

$$\mu_M(E) = \rho_M \cdot \left(\frac{\mu}{\rho}\right)^{(M)}(E) \tag{1.3}$$

[6]The atomic mass unit "u" equals approx. $1.660 \cdot 10^{-27}\,kg$.

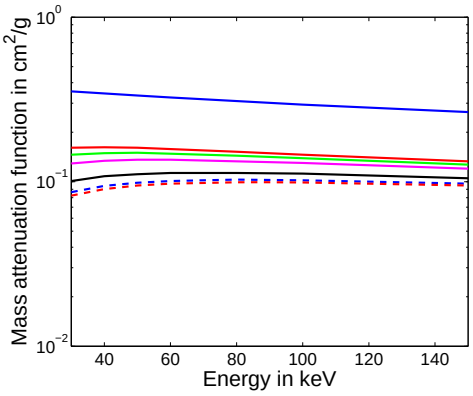

(a) Incoherent attenuation

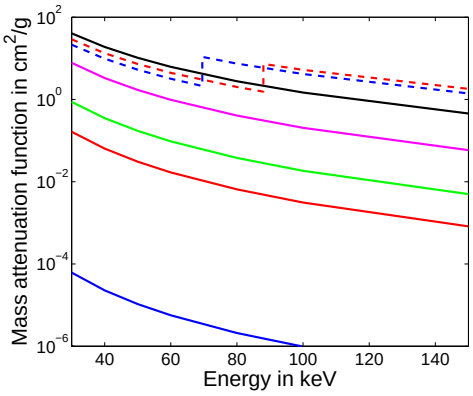

(b) Photoelectric effect

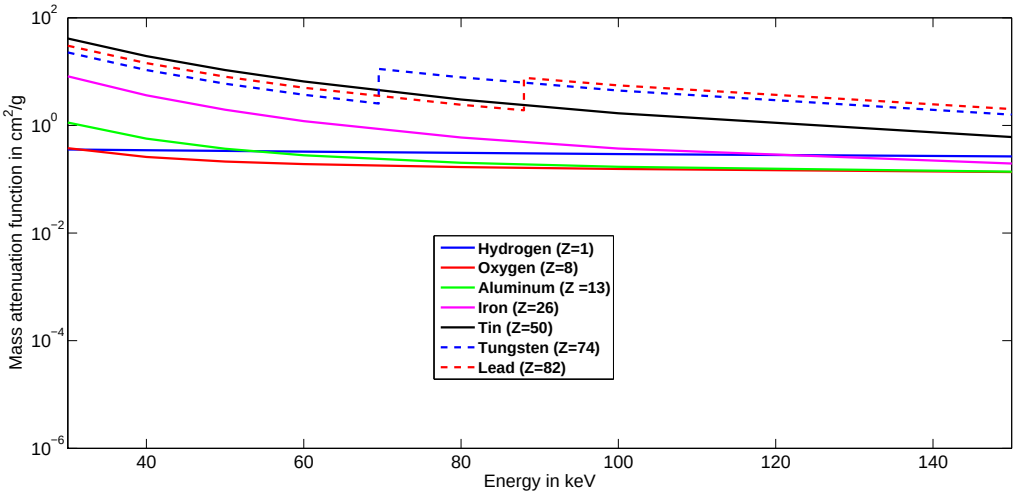

(c) Total attenuation

Figure 1.15: Mass attenuation function and its two major components in the CT energy range for various elements. Data taken from XCOM database [Berg 98].

where ρ_{M} is the density of the material usually given in $\frac{\mathrm{g}}{\mathrm{cm}^3}$. The mass attenuation function has the unit $\frac{\mathrm{cm}^2}{\mathrm{g}}$, so the unit of the spectral attenuation coefficient is cm^{-1}. Using Eq. (1.1) the spectral attenuation of any material with known composition can be modeled. The ICRU 46 report [ICRU 92] summarizes the chemical composition and photon-cross sections for a variety of biological tissues. The spatial distribution of the spectral attenuation coefficients should ideally be measured by a single-energy CT device for an effective energy E_{eff}.

Attenuation Law

Having determined the spectral attenuation coefficient of a material M, the number of non-attenuated photons can be computed with the attenuation formula (Beer-Lambert law):

$$I(E) = S(E)e^{-l\mu_{\mathrm{M}}(E)} \tag{1.4}$$

where l represents the material thickness, $S(E)$ the number of quanta per energy E and $I(E)$ the intensity of the quanta passing through the object without being attenuated. If a non-homogeneous material with a spatial distribution of spectral attenuation coefficients $\mu(E, \mathbf{r})$ is exposed to radiation with a spectral energy distribution $S(E)$, the attenuation law reads:

$$I(E) = S(E)e^{-\int_0^{+\infty} \mu(E, \mathbf{l}_{\theta,t}(\alpha))\mathrm{d}\alpha} \tag{1.5}$$

For 2-D slice reconstruction, $\mathbf{r} \in \mathbb{R}^2$ denotes the location in the world coordinate system and the expression $\mathbf{r} = \mathbf{l}_{\theta,t}(\alpha) : \mathbb{R} \to \mathbb{R}^2$ represents a parameterization of the X-ray beam with an angular parameter θ and a distance to the origin t. Figure 1.16b illustrates this geometry.

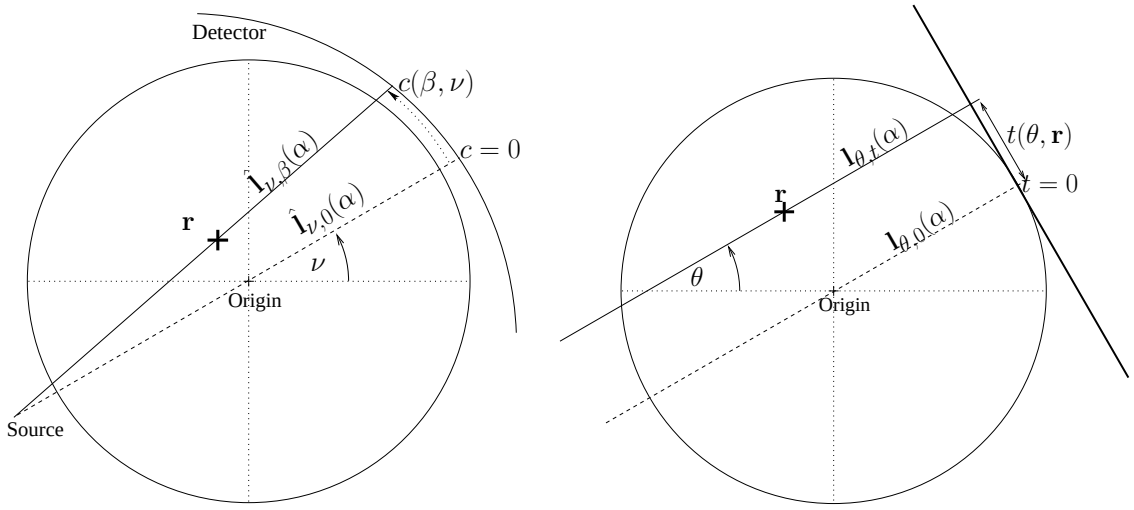

(a) Fan beam projection geometry.

(b) Parallel beam projection geometry.

Figure 1.16: Notation for fan- and parallel-beam geometries.

Section 1.3 showed that X-ray tube spectra are not mono-energetic and Sec. 1.4 introduced the type-dependent spectral sensitivities $D(E)$ of CT detectors. These properties have to be taken into account when formulating the relation between input spectrum $S(E)$, attenuator $\mu(E, \mathbf{r})$ and corresponding output signal $I_{\theta,t}$ of the detector channel and reading corresponding to the ray parameters θ and t:

$$I_{\theta,t} = \int_0^{\infty} S(E)D(E)e^{-\int_0^{+\infty} \mu(E, \mathbf{l}_{\theta,t}(\alpha))\mathrm{d}\alpha}\mathrm{d}E \tag{1.6}$$

1.6.2 CT Reconstruction

The goal of CT reconstruction is to recover the spatial distribution of attenuation coefficients from the measured $I_{\theta,t}$-values. In classical single energy CT, the energy information of the spectral attenuation coefficient is lost due to the measurement process and cannot be recovered. Therefore the polychromatic characteristics of the

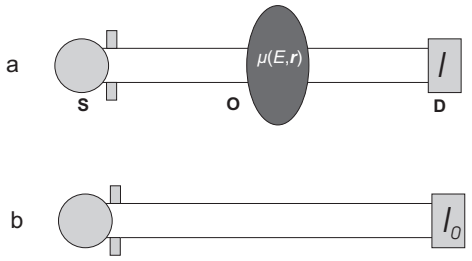

Figure 1.17: Schematics of an X-ray attenuation measurement.

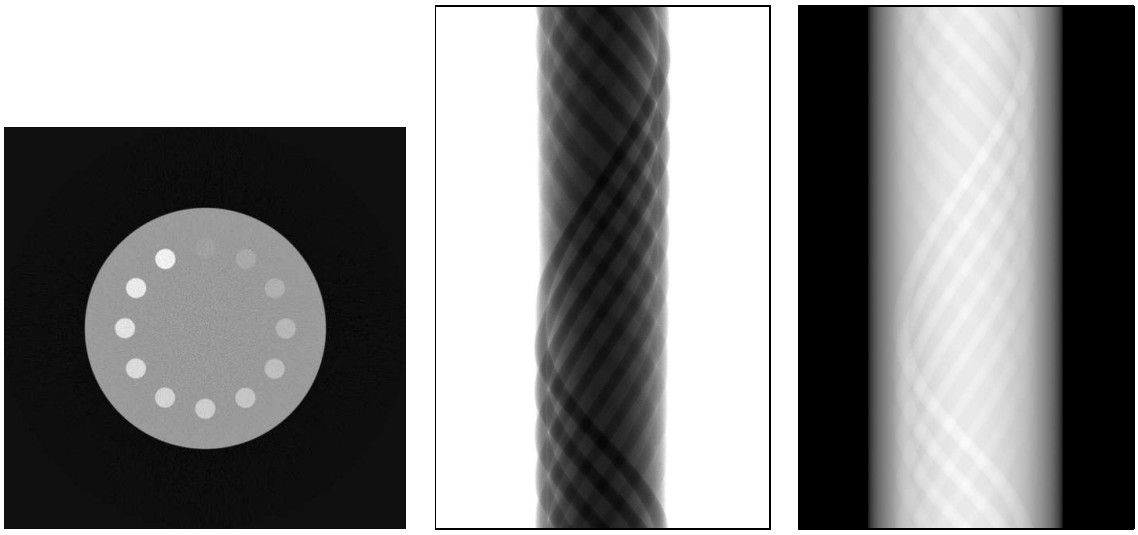

(a) Slice image of a clock phantom. (b) Measured intensities. (c) Sinogram of integrated attenuation values.

Figure 1.18: Left: Slice image of a clock phantom. The attenuation coefficients at 64 keV are gray-coded (intensity window center (c): $0.016\,\mathrm{mm}^{-1}$, width (w): $0.032\,\mathrm{mm}^{-1}$). Middle: Measured intensities $I_{\theta,t}$ for mono-energetic radiation at 64 keV (arbitrary units). Right: Corresponding sinogram of attenuation values (arbitrary units). The gantry rotation angle θ (ordinate direction) covers one full rotation, the detector channels are arranged on the horizontal axis.

input spectrum are neglected and instead of an input spectrum $S(E)$ and a detection sensitivity $D(E)$, an effective detected intensity I_0 is measured in a calibration step, in order to recover an effective attenuation $\bar{\mu}(\mathbf{r})$. Figure 1.17 depicts the set-up of a standard X-ray attenuation measurement. The source **S** emits a flux of X-ray quanta at an object **O**. The object consists of X-ray attenuating materials. They are described by the spectral attenuation coefficient $\mu(E, \mathbf{r})$ at position $\mathbf{r}$. The detector **D** registers the quanta which have passed through the object. Two independent measurements without and with the object are performed. The first measurement yields the measured intensity in air, called I_0, the second one yields the attenuated intensity:

$$I(\theta, t) = I_0 e^{-\int_0^{+\infty} \bar{\mu}(\mathbf{l}_{\theta,t}(\alpha))\mathrm{d}\alpha}. \tag{1.7}$$

This equation can be re-formulated to:

$$P(\theta, t) = \ln\left(\frac{I(\theta, t)}{I_0}\right) = -\int_0^{+\infty} \bar{\mu}(\mathbf{l}_{\theta,t}(\alpha))\mathrm{d}\alpha. \tag{1.8}$$

The collection of all measured values $P(\theta, t)$ is called *sinogram* because each point $\mathbf{r}$ in the world coordinate system can be associated with a sinusoidal trace in the projection space of θ and t. Figure 1.18 illustrates relation between the spatial distribution of attenuation values $\mu(E, \mathbf{l}_{\theta,t}(\alpha))$, the resulting intensities $I_{\theta,t}$ and the projected attenuation values $P(\theta, t)$ on a simple phantom for a circular single-slice CT scan.

Equation (1.8) is called a *Radon Transform* [Rado 17]. Unlike Eq. (1.6), it can be solved for $\bar{\mu}(\mathbf{r})$ analytically. Many different reconstructions exist, all of which serving specific purposes. Currently, the most popular reconstruction technique in CT is *Filtered Back Projection* (FBP) [Kak 01]. Several variants of FBP have been developed for different acquisition geometries. A variant for 3-D cone beam reconstruction is called *FDK* [Feld 84]. Helical tube and detector trajectories are used to quickly cover larger fields of view. This requires an adapted reconstruction technique called *Spiral* or *Helical CT reconstruction* [Kale 90]. Special reconstructions are also required for non-circular acquisition trajectories (for instance *saddle trajectories* [Pack 04]) or circular short scan acquisitions [Noo 02] which do not cover the minimally necessary acquisition angle for FBP of 180° plus cone / arc angle. This is especially interesting for C-arm CT reconstruction, where a full circle trajectory is not always possible.

Compressed sensing reconstruction techniques are supposed to cope with limited projection data. Prior image constrained compressed sensing (PICCS) [Chen 08], for example, may be used to reconstruct data even for under-sampled projection data, where standard FBP reconstructions suffer from strong artifacts. *Iterative reconstruction* schemes like the Ordered Subset Expectation Maximization (OSEM) algorithm [Huds 94, Mang 95] provide good insensitivity to measurement noise at the cost of increased computational efforts. These techniques are commonly used for PET / SPECT reconstruction as FBP does not cope well with the typically bad signal to noise ratio (SNR) of PET / SPECT data. Recently, these techniques become increasingly attractive for CT reconstruction as well, since the performance of modern multi-core processors, field-programmable gate array (FPGA) boards or general-purpose computing on graphics processing units (GPGPU) allows to perform these reconstructions in an acceptable computation time even for CT. The reconstruction times of current CT systems for common scan protocols are in the range of several seconds to up a few minutes depending on the type of the CT scan.

Indirect Fan-Beam FBP Reconstruction

In this section we briefly introduce a basic *indirect fan beam* FBP reconstruction. Many of the algorithms introduced in this work make use of FBP-based reconstruction algorithms. The following one can be used for very basic realizations of these algorithms. This reconstruction consists of three steps which are illustrated in Fig. 1.19 for a single line of the sinogram shown in Fig. 1.19a:

1. Rebinning of the fan-beam data to parallel-beam data by interpolation (Fig. 1.19b).

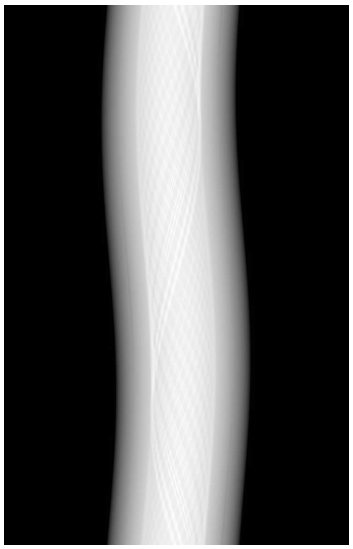

(a) Original fan-beam sinogram.

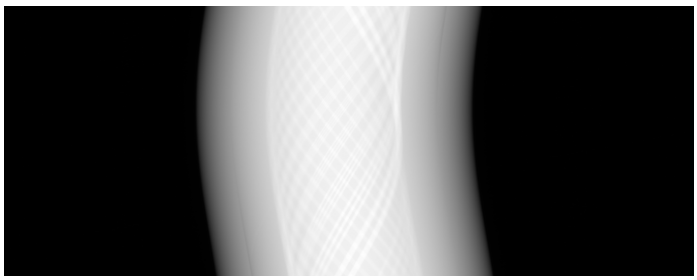

(b) Re-binned sinogram.

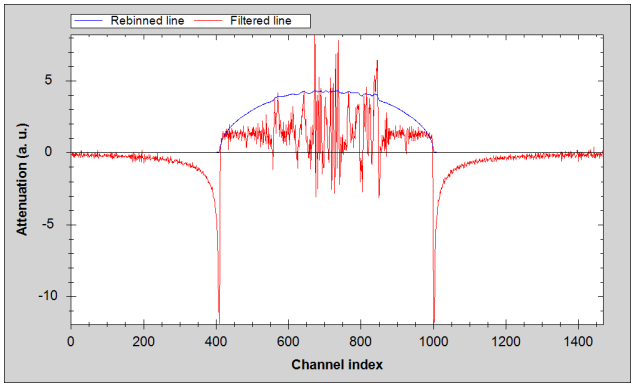

(c) Line excerpt before and after filtering.

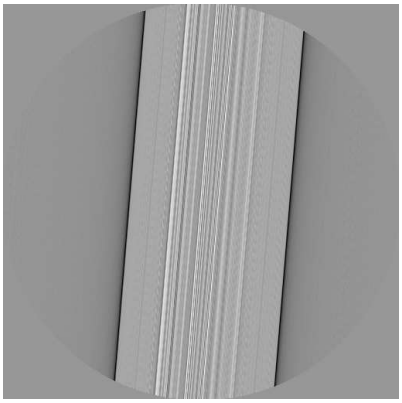

(d) Back-projected filtered line.

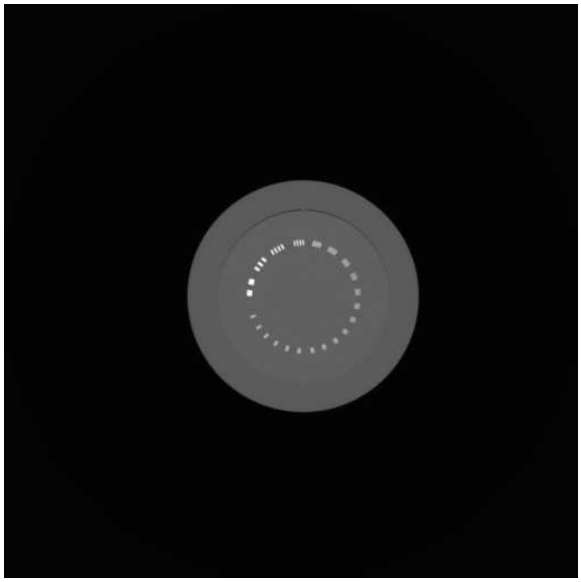

(e) Reconstructed slice image after 1152 back-projections (c: $0.03\,\mathrm{mm}^{-1}$, w: $0.06\,\mathrm{mm}^{-1}$).

Figure 1.19: Example illustration of the indirect fan-beam FBP reconstruction steps.

2. Filtering of the data with a high-pass kernel (Fig. 1.19c).

3. Back-projection of all projections into image space (Fig. 1.19d).

We denote the fan beam projections $\hat{P}(\nu, \beta)$, where ν is the gantry angle and β is the channel angle (see Fig. 1.16). The rebinned data is denoted $P(\theta, t)$.

The transformation between fan beam and parallel beam coordinates is given by $\theta = \beta + \nu$ and $t = D\sin(\beta)$. D is the distance between X-ray source and coordinate origin.

The filtering is usually performed in frequency space in detector channel direction. First, a discrete Fourier transform (DFT) is performed on a line of detector channels, the transformed line is multiplied with the filter kernel and an inverse Fourier transform (IDFT) is applied. The *ideal* reconstruction kernel is a high pass kernel of the form $H(w) = |w|$ for the frequency coordinate w. As the DFT has its maximum frequency w_N at one over half the sample distance (*Nyquist frequency* f_N), the kernel has to be cut-off at this frequency. This kernel is called *Ram-Lak* kernel. High frequencies are usually suppressed by practical reconstruction kernels as these usually have a bad SNR. The Shepp-Logan kernel, for instance, uses a cosine-window which attenuates higher frequencies. Figure 1.20 compares some well known kernels. In practice, each CT manufacturer uses an individual set of reconstruction kernels which are adapted to specific applications. For comparisons with respect to image quality and noise reduction, we use the above mentioned standard kernels and an additional set of modified cosine kernels with an easily steerable trade-off between noise and sharpness. We refer to these kernels as Cos*XXX* kernels where *XXX* stands for a two or three digit number indicating the cut-off frequency f_c relative to the Nyquist frequency. Cos50 represents a kernel with a cut-off frequency at 50 % of the Nyquist frequency, Cos675 means $f_\mathrm{c} = 0.675 \cdot f_\mathrm{N}$.

The calculation rule for the discrete filter of length l samples is as follows:

$$K[i] = K[l - i - 1] = \frac{i}{l} \cdot \frac{\pi}{N_\mathrm{r}} \cos\left(\frac{\pi \cdot i}{i_\mathrm{c}}\right) \tag{1.9}$$

for $\left\{i \in \mathbb{N} | 0 \leq i < \frac{1}{2} \cdot l\right\}$. The cut-off index is defined as $i_c = l \cdot \frac{f_\mathrm{c}}{f_\mathrm{N}}$ and N_r is the number of readings per rotation.

The back-projection requires the computation of t for all projection angles angles θ and all spatial samples $\mathbf{r}$ in the image space. This requires an additional interpolation of the filtered projection data in order to find the projection value for the distance coordinate t.

1.6.3 Beam Hardening

As mentioned in the previous section, the polychromatic characteristics of the radiation are neglected in single energy CT reconstruction. If the input spectrum was mono energetic at energy E_eff, the equation $\bar{\mu}(\mathbf{r}) = \mu(E_\mathrm{eff}, \mathbf{r})$ would hold. Applying Eq. (1.7) to measurements with polychromatic radiation causes artifacts in the reconstructed images. When X-ray spectra are attenuated by matter, their effective energy shifts towards higher energies, as lower energy components are attenuated more strongly than higher ones. This effect is called beam hardening and causes an

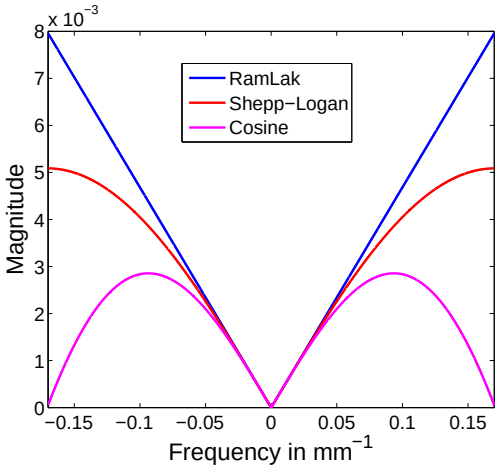

Figure 1.20: Reconstruction kernels for parallel-beam FBP.

under-estimation of the effective attenuation of strong attenuators. If this property is not dealt with, it leads to artifacts in the reconstructed images. This causes homogeneous areas in reconstructed images to become darker towards the inside. Figure 1.21 shows a simulated example of an elliptical water phantom with two dense bone insets. The *cupping* and *streak artifacts* are due to the beam hardening of the water and especially the strongly attenuating bone insets.

We illustrate this effect and its correction on a simple example for beam hardening in water: For the filtered 120 kVp tube spectrum from Fig. 1.4a and the detector's spectral sensitivity of Fig. 1.8, we get an effective energy of approx. 69.1 keV. This energy is the centroid of the product of tube spectrum and detector sensitivity. The attenuation coefficient for water is $0.194\,\mathrm{cm}^{-1}$ at 69 keV (see Fig. 1.14b). This is the desired value which will be scaled to 0.0 HU. For the center point of a slice through a water cylinder of 10 cm diameter, the beam hardening causes the effective energy to rise to approx. 74.0 keV corresponding to an attenuation coefficient of $0.189\,\mathrm{cm}^{-1}$ for water. The center of the reconstructed slice through the water cylinder will have the erroneous value of −25.8 HU (including the effects of reconstruction of beam-hardened data). The task of a beam hardening correction is to replace the measured projected attenuation value 1.89 with the value 1.94 ($0.194\,\mathrm{cm}^{-1} \cdot 10\,\mathrm{cm} = 1.94$) that would be observed with mono-energetic radiation of 69.1 keV.

Various beam hardening correction algorithms exist. For a soft-tissue calibration, projection measurements through soft-tissue like materials of variable known thicknesses are performed. For these, the equivalent water thicknesses are known. A simple function is fit through the pairs of measured and expected values. This function is inverted and then used as a look-up table: For each measured attenuation, the equivalent water thickness is looked up, which then replaces the measured attenuation. If bone-induced beam hardening is also corrected, a separation into bone and water components can be performed (see for instance [Jose 78, Nalc 79]). An approach that additionally deals with the presence of the prevalent contrast agent iodine is given in [Jose 97]. For Dual Energy CT, special quantitative correction methods exist. These take advantage of the two measurements at different energy weightings and special properties of the attenuation functions of body tissues. Examples for this type of

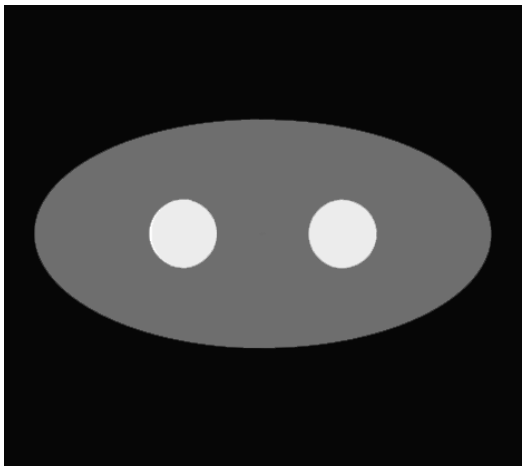

(a) CT simulation result with mono-energetic radiation.

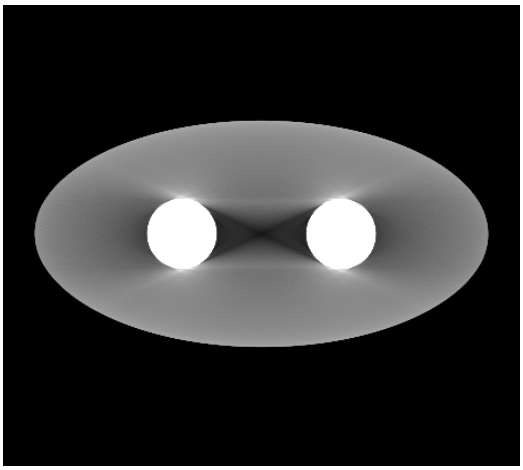

(b) CT simulation result with 120 kV tube spectrum with visible beam hardening artifacts.

Figure 1.21: Beam hardening example: (a) A simple phantom set-up consisting of water (gray), bone (white) and air (black). (b) Reconstruction of the phantom with visible beam hardening artifacts. We observe a superposition of the typical cupping artifact caused by the patient water background and the funnel-shaped artifact between strong bone absorbers.

methods can be found in [Jose 97, Yan 00]. The latter publication suggests an iterative method with a linearized polychromatic forward projection. The concept of the *Local Spectral Weighting function* [Heis 09, Heis 10] can also be used for a quantitative beam hardening correction. It is introduced in Sec. 3.3.

1.6.4 Basic CT Calibration Steps

In order to suppress artifacts and deliver the image quality required for medical CT, several calibration steps of the CT system have to be performed on a regular basis. The most important ones are:

- **Air calibration:** The computation of the beam attenuation from the received detector signal requires a precise measurement of the detector signal in air with no attenuator in between source and detector. This quantity is denoted I_0 in Eq. (1.7). The I_0 values are measured for every detector channel on a regular basis. Multiple measurements are averaged, so that the I_0 values carry as little noise as possible.

- **Water scaling:** The spatial distribution of output values is usually given in Hounsfield units instead of attenuation values. Whereas attenuation values totally depend on system characteristics, the HU values are fixed for air (-1000 HU) and water (0 HU). However, the HU values are not quantitative in a sense that a specific tissue or material composition gets identical HU values for varying CT scanners and/or scan parameters. A evaluation of the energy dependence was performed in [Zatz 77]. Some typical HU values for a variety

Tube voltage	gall	pus	pus+blood	blood	urine
80 kV	15-26	25-36	40-55	42-50	0-70
140 kV	7-15	13-28	32-45	35-45	0-50

Table 1.2: HU value ranges for various body fluids according to [Heis 06].

of body fluids and two different tube voltage settings are shown in Tab. 1.2. The water scaling measures the attenuation values $\bar{\mu}_{\mathrm{W}}$ of water for all available scan protocols. During each scan, the attenuation values are normalized to the HU scale using the according $\bar{\mu}_{\mathrm{W}}$ value.

- **Beam hardening calibration:** Beam hardening corrections require some reference projection measurements of materials with known composition and thickness. These measurements are used by the beam hardening correction to correct the measurement values. The exact type of reference measurements depends on the used beam hardening correction.

1.7 CT Image Quality Metrics

The image quality of CT can be assessed with various quality measures. These are governed by noise and signal properties such as sharpness and contrast. In this section, three important quality metrics are introduced and ways of computing these measures from specific measurements are shown. The metrics are called *Modulation Transfer Function* (MTF), the *Noise Power Spectrum* (NPS) and the *Detective Quantum Efficiency* (DQE).

MTF: The MTF is similar to the magnitude of a system response function. The MTF is normalized so that the constant component is always one. The *detector MTF* measures the frequency transfer behavior of the detection process, the *image* or *system MTF* measures the behavior of the whole CT system. Due to the reconstruction process, the image MTF is inhomogeneous throughout a CT image or volume. This means it is two- or three-dimensional and varies with respect to space. In order to reduce complexity, the system MTF is often characterized by giving only a 1-D MTF for the iso-center or a radial and tangential MTF for a specific location. The MTF is influenced by many system parameters. The most important ones are X-ray focus size, detector pixel layout and dimensions, detector cross-talk and the reconstruction method.

The image MTF can be measured with various techniques. For a 2-D slice MTF, a very thin high contrast object, for instance a tungsten wire perpendicular to the slice plane is imaged [Bisc 77]. From this measurement, the *Point Spread Function* (PSF) can be extracted. The MTF can be computed using the magnitude of the Fourier transform of the point spread function (see Fig. 1.22 for an illustration). For 1-D MTFs in a specific direction an image of an edge may be used [Judy 76]. This yields the *Edge Spread Function* (ESF). A 1-D MTF corresponding the orthogonal

edge direction can be computed using the Fourier transform of the derivative of the ESF (Fig. 1.23). The detector MTF can be measured with similar approaches.

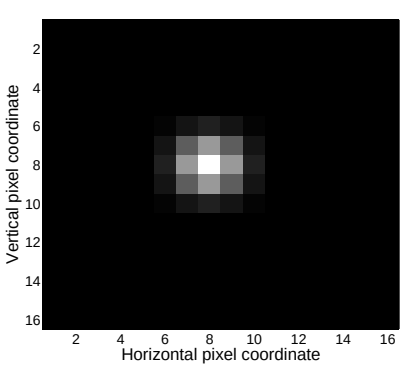

(a) Example of a point spread function, for instance from a cross section of a thin tungsten wire.

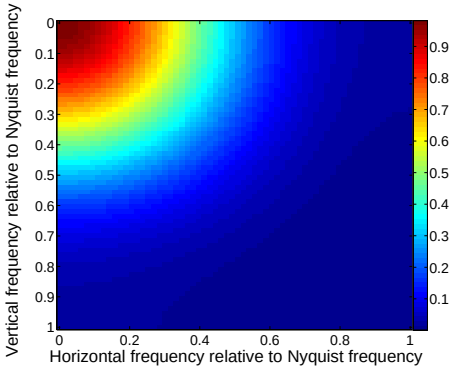

(b) Corresponding 2-D MTF.

Figure 1.22: MTF computation from a point spread function.

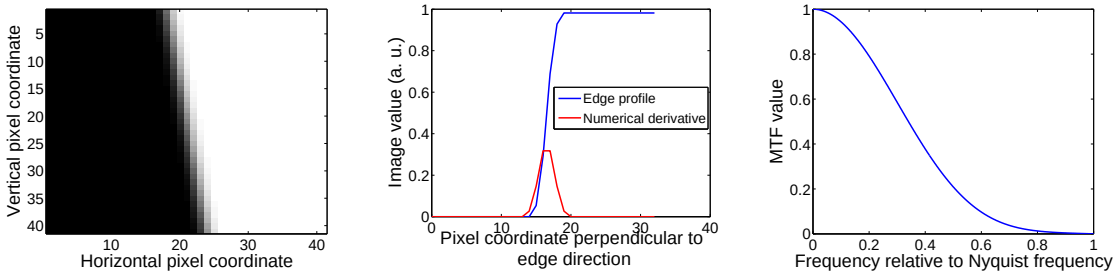

(a) (b) (c)

Figure 1.23: MTF computation from an edge spread function: Figure (a) shows an example edge image, (b) is the corresponding edge spread function extracted perpendicularly to the edge direction and (c) is the corresponding 1-D MTF.

NPS: The NPS characterizes the spectral composition of image noise. It carries information on the noise structure and correlations. The image NPS is also inhomogeneous and two- or three-dimensional. It represents the noise power with respect to frequency. Its main influences are similar to those of the image MTF except for focus size, which has no major influence on the NPS.

The detector NPS can be measured by acquiring a flat field image. This is a projection image with a homogeneous irradiation of the detector. Subtracting the constant component gives a representation of the projection noise signal $n(c_x, c_y)$. The NPS can be computed from this signal by computing the Fourier transform of its autocorrelation function. This corresponds to the squared magnitude of the Fourier transform of the original signal:

$$\begin{aligned} \mathrm{NPS}_{\mathrm{D}}(f_x, f_y) &= \mathcal{F}\{R_{nn}(\nu_x, \nu_y)\} = & (1.10)\\ &= \mathcal{F}\left\{\int_{-\infty}^{+\infty}\int_{-\infty}^{+\infty} n(c_x, c_y)n(c_x+\nu_x, c_y+\nu_y)\mathrm{d}c_x\mathrm{d}c_y\right\} = & (1.11)\\ &= |\mathcal{F}\{n(c_x, c_y)\}|^2 & (1.12)\end{aligned}$$

with $\mathcal{F}\{\cdot,\cdot\}$ being the 2-D Fourier transform[7], c_x, c_y the detector channel coordinates, f_x, f_y the frequencies in horizontal and vertical direction and $R_{nn}(\nu_x, \nu_y)$ the autocorrelation function of the noise signal. The NPS itself is denoted $\mathrm{NPS}_{\mathrm{D}}(f_x, f_y)$.

Image NPS calculation is a very complex process for CT images due to the non-stationarity of the noise. Unlike for the detector NPS, it is not sufficient to get a noise-representation in the image domain. Instead, all influences of the reconstruction process have to be modeled. Early approaches like [Ried 78] or [Kije 87] present limited theories on the prediction of the image NPS from the projection NPS. In [Bors 08a], an analytic noise propagation model is presented that matches the indirect fan-beam reconstruction frequently used in this work. In [Bald 10a] a noise back-projector is presented. It is based on a projection noise model and computes local image noise representations and local noise power spectra for arbitrary image locations.

DQE: The DQE is a measure for the dose efficiency of the detector. It quantifies the loss in *Signal-to-Noise Ratio* (SNR) caused by the detection process. As X-ray generation and detection is a Poisson distributed random process, measurement of X-ray quanta is always impaired by quantum noise and the input SNR has a finite SNR value. This *optimal* detection SNR is defined by the square root of the ratio of signal power over quantum noise variance. The input SNR increases with increasing dose. It marks the upper SNR bound for any X-ray detection process. The DQE measures to what extent the detection process additionally decreases the SNR relative to the optimal SNR. The DQE can either be a scalar value corresponding to the squared ratio of SNRs after and before detection (single channel DQE) [Rose 46, Zwie 65]. In this case, the DQE value is always between 0 and 1. An alternative definition in the frequency domain exists: The *spectral* DQE defines the relative SNR loss on a given range of frequencies [Rabb 87, Cunn 99]. In this case it is dependent on detector NPS and detector MTF. The spectral DQE is defined in the international standard IEC 62220-1 [IEC 06].

The DQE computation in the frequency-domain requires measurements of the detector Modulation Transfer Function $\mathrm{MTF}_{\mathrm{D}}(f_x, f_y)$, the detector NPS, the detector gain factor G and the X-ray flux Φ in quanta per unit area. From these quantities, the DQE is computed with the following formula:

$$\mathrm{DQE}(f_x, f_y) = \frac{G^2 \cdot \mathrm{MTF}_{\mathrm{D}}^2(f_x, f_y) \cdot \Phi}{\mathrm{NPS}_{\mathrm{D}}(f_x, f_y)} \tag{1.13}$$

[7]The expression $\cdot,\cdot$ indicates that a transform takes a two-dimensional function of the form $\mathbb{R}^2 \to \mathbb{R}$ or $\mathbb{R}^2 \to \mathbb{C}$ as input. The transformed function is also two-dimensional.

The gain G is an amplification factor that maps the detected X-ray energy to the output quantity of the detector. This definition expects the detector's response function to be linear. If this is not the case, the DQE changes with respect to X-ray flux.

1.8 Scientific Contributions of this Work

This contents of this thesis can be divided into three major parts covering different aspects of Quantitative CT: The first part is dedicated to spectral detection of X-ray radiation which marks the basis for Quantitative CT. Part two is dedicated to algorithms for QCT applications. The topic of part three is image enhancement and noise reduction for spectral CT data.

1. **Spectral Detection:** We introduced a very efficient and precise way of simulating these detection systems called look-up table-based detector simulation. It enables a standard workstation PC to conduct a full-scale Monte-Carlo style CT data acquisition simulation within several hours. Two variants of this simulation concept were developed for integrating scintillation and counting, directly-converting semiconductor detectors. Especially the latter variant was used to study the behavior of such detector systems in a variety of medical application scenarios as these detectors are not yet commercially available for medical CT and research relies mostly on simulation results.

    - **Scintillator Simulation:** *Look-up Table-Based Simulation of Scintillation Detectors in Computed Tomography*, IEEE Medical Imaging Conference 2008 [Bald 08]
    - **Semiconductor Simulation:** *Lookup Table-Based Simulation of Directly-Converting Counting X-Ray Detectors for Computed Tomography*, IEEE Medical Imaging Conference 2009, Orlando [Bald 09]

    Scientific results making use of these simulations were published at MIC and SPIE Medical Imaging conferences in 2009 and 2010: In [Kapp 09a] a comparison of quantum-counting with dual-layer and dual-kVp scintillation detectors is presented. Various quality measures for quantum counting CT are derived from simulations in [Kapp 10b] and [Kapp 10a] presents a prototype system of a quantum counting detector which was developed using simulation results.

2. **Quantitative Reconstruction:** The major contribution here is the development of a novel QCT framework called *Local Spectral Reconstruction*. This method provides a unified framework for QCT applications, it can for instance be used to formulate and perform SPECT or PET attenuation correction, energy calibration, material concentration estimation and material identification with one common approach.

    - **QCT Framework** *Quantitative image-based spectral reconstruction for computed tomography*, Medical Physics [Heis 09]

- **Application Overview:** *Evaluation of an image-based algorithm for quantitative spectral CT applications*, SPIE Medical Imaging 2010 [Heis 10].

3. **Noise Reduction for Spectral CT:** Reconstruction CT datasets have very specific, non-stationary noise properties that are spatially non-homogeneous. We developed an analysis method for local noise properties. A novel post-reconstruction method for de-noising multi-energy CT data. It introduces a purely histogram-based denoising approach for multi-energy CT data that can be combined with standard frequency-based filters to enhance the quality of QCT data and enable low-dose QCT applications. Patient dose is one of the key issues of multi-spectral medical CT acquisition. With our approach, QCT applications are possible at the dose level of a standard CT acquisition. The last section of this part introduces a iterative, frequency-based pre-reconstruction filter that combines the advantages of image-based filters with projection-based filters to achieve strong noise reduction while maintaining image details and sharpness. This method is an adaption of the well-established concept of bilateral filtering which makes use of specific properties of the CT projection and reconstruction process.

   - **Local Noise Property Analysis:** *Non-stationary CT image noise spectrum analysis*, Bildverarbeitung für die Medizin (BVM) 2010 [Bald 10a]
   - **Multi-Energy Denoising:** *Value-Based Noise Reduction for Low-Dose Dual Energy Computed Tomography*, 13th International Conference on Medical Image Computing and Computer Assisted Intervention (MICCAI) 2010 [Bald 10b]
   - **Pre-Reconstruction Filtering:** *Ray Contribution Masks for Iterative Structural Sinogram Filtering*, submitted to IEEE Transactions on Medical Imaging

Chapter 2

Detector Simulation

This chapter covers the spectral detection part of quantitative CT. We provide a detailed analysis of different detection concepts based on detector simulations. The simulation concepts were developed within the scope of this thesis. CT detectors are constantly improved in terms of resolution, coverage and signal quality to provide better images and a broader range of applicability. The development of a new detector requires precise evaluation of proposed designs, so that properties like pixel dimensions or material composition can be optimized. As building detector prototypes is very expensive, the evaluation of many parameters relies on simulations. For this purpose, we provide efficient and precise detector simulations for different detector types. We give a short introduction into detector simulation and introduce two simulation concepts that are applicable to a variety of different detector layouts based on scintillators or semiconductors. Two realizations of the simulation concepts are discussed in detail: One for integrating scintillation detectors and one for directly converting semiconductor detectors. The simulations are validated with data from full-scale Monte-Carlo simulations and measured data to show that this simulation approach offers the same precision as a full-scale Monte-Carlo particle simulation. The computation speed is over 200 times faster for complete scan simulations with standard MC particle interaction simulations.

2.1 Simulation Concepts

2.1.1 Monte-Carlo Simulation of X-Ray Detectors

The stochastic behavior of X-ray detectors is too complex to be characterized analytically. The basic idea behind Monte Carlo (MC) simulation of detector behavior is conducting a huge number of random experiments. Precise simulation of the behavior of X-ray detectors usually requires an MC simulation of the particle interactions within the detector material. For this task, a variety of tools is available. Geant [Agos 03, Alli 06] is a frequently used general purpose tool for MC simulation of particle interactions. It was used to generate interaction events for some of the simulations introduced in this chapter. Other general purpose MC particle interaction simulations are PYTHIA [Beng 87] or ISAJET [Baer 00]. Giersch et al. [Gier 03]

demonstrate the application of the Geant-based MC simulation tool ROSI to various simulation problems for medical X-ray detectors.

A full detector simulation from the incoming X-ray spectrum to the resulting detector has to include additional effects which depend very much on the investigated detector type, e. g.

- for scintillation detectors, the light transmission in the scintillator material has to be covered (see [Wirt 03]),
- for directly converting semiconductor detectors, the charge transport in the semiconductor has to be taken into account [Krei 08]. Additionally, effects of the detector electronics due to amplification, quantization etc. have to be simulated.

Precise MC-based approaches offer a superior precision for the full range of input parameters. The huge demand in terms of computation time, however, prohibits full scale simulations on regular PC hardware. For the design of CT systems the impact of physical effects on image quality has to be studied. Simulations of complete CT scans including all relevant effects have to be carried out to inspect reconstructed images. Image quality characteristics can directly be related to detector properties. These correlations need to be understood prior to building detector prototypes.

2.1.2 Look-Up Table-Based Detector Simulation

In this chapter we introduce a look-up table (LUT)-based approach to detector simulation. In general, a look-up table holds precomputed data that can be accessed via indices or keys. For look-up table-based detector simulation, this data can, for instance, incorporate photon-interaction events, electrode pulses or light transport properties. It is usually indexed by spatial location and / or event energy.

This approach enables a precise evaluation of a variety of different detector designs at Monte-Carlo level and helps finding optimized detector settings for parameters like pixel size and depth etc. Its superior simulation speed compared to pure MC simulations makes simulations of whole CT scans on standard hardware feasible. The basic concept is to separate the detection process into logical and / or physical steps and define the interfaces between these steps. Then, each step is either modeled analytically or numerically or a look-up table containing a huge number of precomputed events is generated. Random events are selected from the LUTs according to the requirements of the interface. A common example for X-ray detection is the interaction of incoming X-ray quanta with the detector material. Here, the look-up table holds a huge number of sample interactions. The interface to the next step may require the respective energy and a quantized interaction location so that the following effect can be simulated for a limited number of source locations.

Look-up table-based approaches can be used for various detector types: In [Bald 08] we have shown an application to the simulation of integrating scintillator CT detectors, in [Bald 09] we have applied look-up table based detector simulation on counting semiconductor detectors. However, different detector types usually require individual look-up table set-ups for all detection stages, so the re-usability of simulation code and data between different LUT-based simulations is limited.

2.2 Integrating Scintillator Detectors

2.2.1 Simulation Principles

Several effects have to be taken into account when simulating the detection process of integrating scintillator detectors in order to get a realistic output signal. The basic working principle of this kind of detectors was described in Sec. 1.4. The detection process can be separated into several stages and each stage is described by physical effects which have to be covered by the simulation:

1. Poisson distributed measurement noise: The generation and detection of X-ray quanta is a random process. The numbers of detected quanta per energy are Poisson distributed (see keyword *quantum noise* in [Pett 98]).

2. The interaction between incoming X-ray photons and the scintillator material depends on the photon energy and the material composition of the detector and its pixel geometry.

3. There are different types of interactions which may deflect or create X-ray photons on different paths (see Sec. 1.6.1). These escape photons may cause additional interaction events which may take place in another pixel (X-ray cross-talk).

4. Optical photons are scattered and absorbed within the scintillator.

5. The transport of optical photons may be delayed by defects within the scintillator material (afterglow) [Leco 06].

6. Optical photons may penetrate the septa and leave the detector or reach the photodiode of another pixel (optical cross-talk).

7. The read-out electronic adds electronic noise, hence influences the signal to noise ratio.

Figure 2.1 illustrates the stages 2 to 5 of the detection process.

These effects are directly or indirectly influenced by the geometry of the scintillator pixels, for example by the ratio of septa and active pixel area or the pixel height. The introduced simulation can be used to investigate the influence of these detector properties on the resulting quality of the reconstructed CT-image. It is capable of simulating X-ray measurements with pixelized scintillation detectors. This also covers many special types of spectral CT measurements as introduced in Sec. 1.5. Dual layer detectors may require only minor adaptations if escape photons between layers should be covered. Dual Energy, Dual Source and kVp-switching do not require any adaptations. *Optical counting*, i. e. counting detectors based on scintillators or scintillation detectors using special photodiodes such as avalanche photodiodes require a redesign of the signal processing part of the simulation.

Figure 2.2 shows the steps of the integrating scintillator detection process and the interfaces between the steps. These steps have to be considered for each incoming

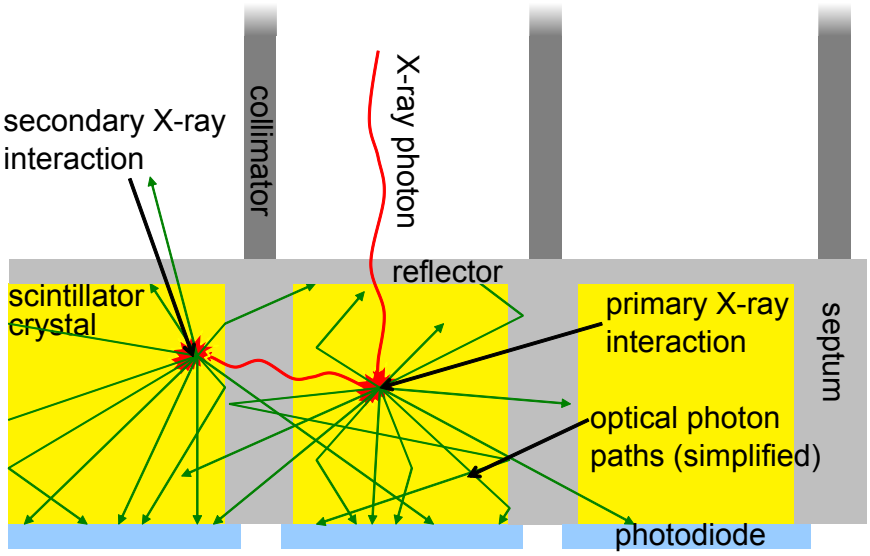

Figure 2.1: Signal generation in scintillation detectors.

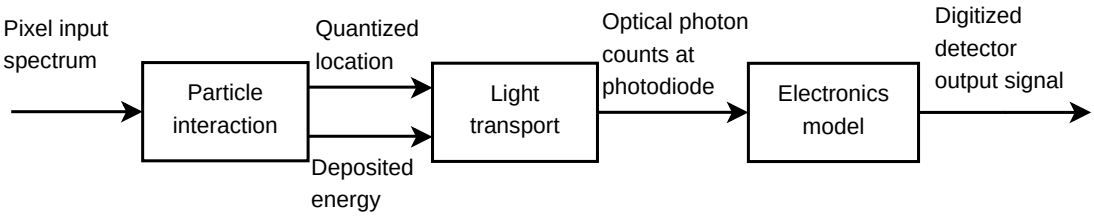

Figure 2.2: Detection steps and interfaces for integrating scintillation detectors.

X-ray photon in each detector pixel. The following section shows how this scheme can be efficiently integrated into a LUT-based detector simulation.

Kappler et al. [Kapp 09b] have integrated this simulation into a full CT simulation chain which generates simulated, reconstructed CT-volumes and contains all relevant physical effects of the CT acquisition process.

2.2.2 Simulation Workflow

The effects mentioned in the previous section are usually modeled by an X-ray- and light photon-based simulation. This approach is very time consuming since the amount of photons to be dealt with is usually very large. We use precomputed interaction events and separate the X-ray photon interaction and the transport of optical photons [Heis 08]. The data is provided in look-up tables, which have to be computed only once for a specific detector geometry and material composition. Figure 2.3a shows the components of the simulation. These components are described in the following sections. Table 2.1 gives an overview of the used LUT and simulation data types.

X-Ray Photon Interaction: The photon interaction LUT holds data of precomputed X-ray interaction events for a uniformly irradiated detector pixel. The incoming X-ray photons hit the detector orthogonally. Covering arbitrary angles of incidence is

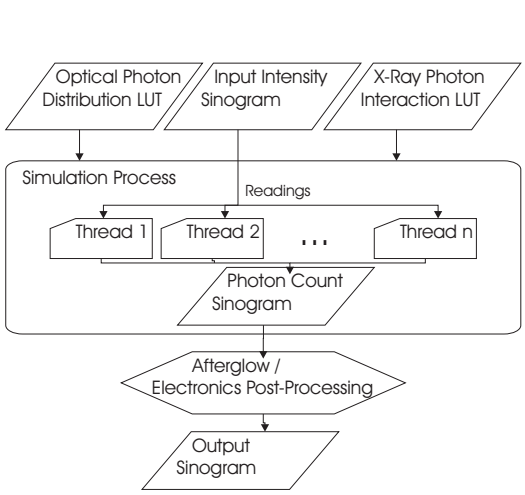

(a) Basic simulation layout

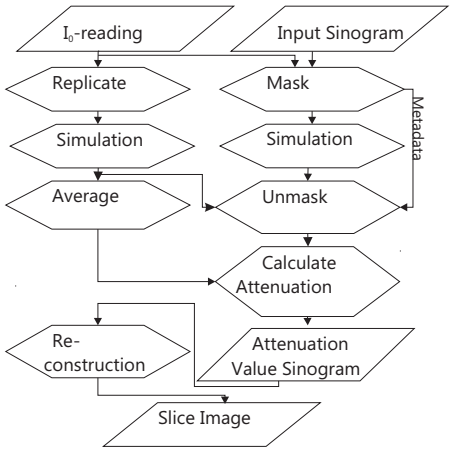

(b) Workflow for slice image generation with masking for complete CT scan simulation

Figure 2.3: Signal flow diagrams for detection- and complete CT scan simulation.

LUT / data type name	**Indexed by**	**Content type**
Input data	Channel, reading, energy bin number	Mean X-ray photon number
PhotonInteractionLUT	Energy bin number	Interaction data
OpticalPhotonDistributionLUT	Voxel position within detector pixel	Histogram of optical photon distribution

Table 2.1: LUT and simulation data types used for integrating scintillation detector simulation.

not necessary for the CT case, as the anti-scatter grid eliminates most X-ray photons from other angles.

This data can be provided by a Monte-Carlo simulation of particle interactions like ROSI [Gier 03] or Geant4 [Agos 03, Alli 06]. The events are grouped into energy bins with respect to the energy of the corresponding incoming photon. We chose to have one million events available for all energy bins of 5 keV width. For these settings, the simulation results do not show any regularity caused by the usage of this LUT. One event contains an arbitrary amount of interaction data-sets, since an incoming photon might not interact at all or might produce one or more interactions. An interaction data-set contains the following entries:

- Relative 2-D detector pixel location of the interaction (non-zero in case of X-ray cross-talk)
- Number of generated optical photons (depends on the deposited energy of the interaction)
- Discrete 3-D location within the scintillator element. The location is quantized to a discrete voxel position $\mathbf{v}$ within the pixel. The sampling of the voxel coordinates has to be sufficiently dense so that changes in light transport properties between voxel locations are very small (see Fig. 2.5).

Figure 2.4 visualizes the LUT-data for two energy bins at 25 keV and 100 keV. Figure 2.4a shows the interaction locations and the respective energy deposition of several thousand 100 keV events. The photon interaction LUT stores the interactions positions in quantized form as 3-D-voxel coordinates.

Figures 2.4(b) and (c) show two histograms of the energy deposition within the scintillator material with respect to the interaction voxel indices. In this case we used $20 \times 20 \times 20$ voxels in ϕ-, z- and depth-direction for each scintillator pixel. The figure shows only the central voxels with respect to the z-direction. This data is computed for a photon interaction LUT that contains 10^6 X-ray photons (events) per energy bin. Energy deposited within the septa is discarded and the corresponding interactions are not stored in the LUT as they do not contribute to the output signal. The figures show that most of the energy is deposited in the scintillator of the illuminated pixel and, as expected, the energy deposition decreases exponentially with increasing depth (see Sec. 1.6.1). The neighboring pixels show the energy deposition due to X-ray cross-talk as they are not exposed to direct radiation. Here, the energy deposition does not show such a clear dependence on depth, but decreases with distance to the center pixel.

Optical Photon Distribution: The optical cross-talk is modeled as a set of two-dimensional histograms $d_{\mathbf{v}}(\mathbf{x_p})$ for each discrete position $\mathbf{v}$ within the pixel. The histograms $d_{\mathbf{v}}(\mathbf{x_p})$ yield the probability that an optical photon released at $\mathbf{v}$ reaches the photodiode at relative pixel position $\mathbf{x_p}$. As the intensity of the optical cross-talk drops exponentially with the distance to the originating pixel, it is sufficient to limit $d_{\mathbf{v}}(\mathbf{x_p})$ to a small region. A significant amount of optical photons does not reach a photodiode pixel, therefore $\sum_{\mathbf{x_p}} d_{\mathbf{v}}(\mathbf{x_p})$ is smaller than 1. The data needed for this

look-up table can be acquired by simulating the light transport within the scintillator material, reflector and septa [Wirt 03]. With this data we form a so called optical photon distribution LUT, which contains a distribution function for each voxel center of the interaction LUT.

The total amount of optical photons generated in one interaction is distributed over pixels within the neighborhood with the respective LUT-entries as weighting factors. Poisson noise is applied to the optical photon numbers of each event and pixel. Figure 2.5 shows the typical properties of this LUT by comparing the detection probabilities for some specific voxel locations. Figure 2.5a shows the log-scaled 2-D histogram for the center voxel.

The influence of the interaction location on the optical cross-talk can be seen in the absolute detection probabilities as well as the amount of cross-talk in the respective neighboring pixels: Figure 2.5b shows only a slight shift in the detection probability if an optical photon is created on the very right or left edge of the scintillator pixel at the same depth. The influence of the depth of interaction is considerably larger (see Fig. 2.5c): Photons created far off the photodiode (PD) have a high cross-talk probability and are less likely to be detected at all.

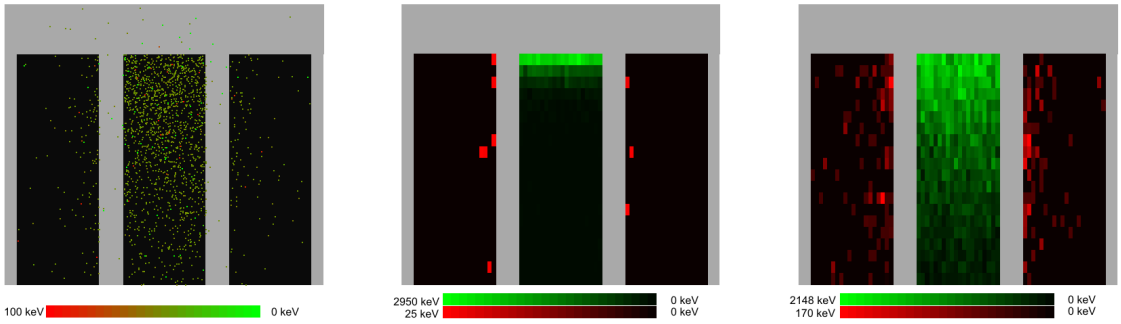

(a) (b) (c)

Figure 2.4: (a) Interaction locations of 2500 randomly picked X-ray photon events (100 keV); (b) and (c) show excerpts of the histogram of energy deposition within scintillator voxels for homogeneous irradiation of center pixel with mono-energetic X-ray photons. Central slice in z-direction is shown. (b) mono-energetic 25 keV photons, (c) mono-energetic 100 keV photons.

Input Data: For a complete scan simulation the input sinogram contains data for all channels and readings. This data consists of mean values of incoming X-ray photons at specific energies. The input sinograms can be computed by an analytic projection tool like NCAT [Sega 03]. For this purpose geometric phantoms have to be defined. For each ray from the focal spot of the X-ray tube to the detector pixels the according lengths within the phantom materials are computed. The total attenuation for the ray can then be estimated using the attenuation coefficients of the phantom materials and the corresponding intersection lengths. These attenuations are applied to an appropriate tube spectrum.

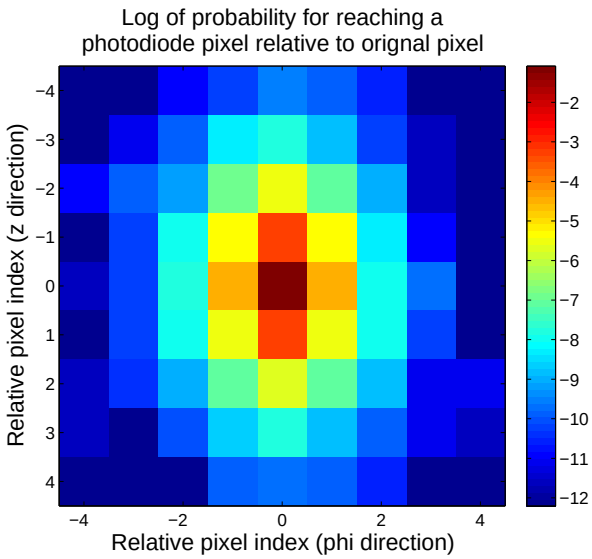

(a) Optical photon distributions for top center region of scintillator pixel

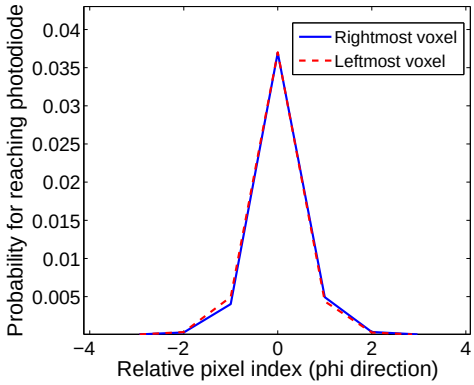

(b) Comparison between rightmost and leftmost voxel with respect to ϕ-direction (central depth- and z-coordinate)

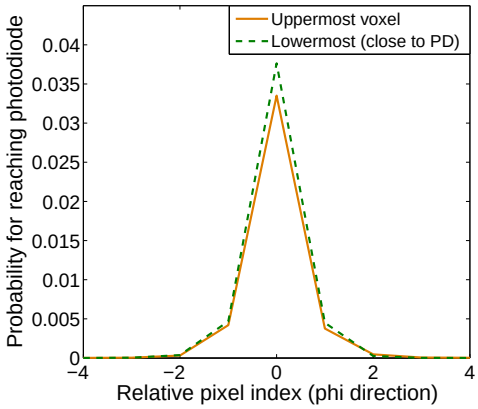

(c) Comparison between topmost and bottommost voxel with respect to interaction depth (central ϕ- and z-coordinate)

Figure 2.5: Optical photon distribution-LUT example and comparisons between voxel positions

Simulation Process: The simulation consists of the following steps:

1. Get the mean number of incoming X-ray photons for each channel, reading and energy level.
2. Get the number of X-ray photons by taking a random sample of a Poisson distribution with mean value from previous step.
3. For each X-ray photon, pick a random event and get all interactions. This yields the number of created optical photons and voxel locations of interactions.
4. For each interaction: Distribute the optical photons to the according photodiode pixels using the matching optical photon distribution LUT entries.
5. Get number of optical photons by taking a random sample of a Poisson distribution with mean value from optical photon distribution LUT entry. Add the resulting number to the output signal of the respective pixels.

The result of this process are optical photon counts at each photodiode pixel. The process can be parallelized for subsequent readings to utilize multiple and/or multi-core processors. The run-time of the simulation is linearly dependent on the total number of incoming X-ray photons of all detector channels and read-outs per channel. The energy distribution of the incoming X-ray photons can have a minor influence on the simulation run-time as the average number of interactions varies with X-ray photon energy.

Electronics and Afterglow Post-Processing: Electronics properties like quantization or amplifier noise additionally influence the measurement. These effects can be modeled as a post-processing step on the photon count data.

Scintillator afterglow is modeled as temporal cross-talk between subsequent measurements. It cannot be handled within the simulation process as this approach does not resolve temporal behavior. If the simulation of afterglow effects is desired, it is treated in a post-processing step as well. It is approximated by a convolution of the measurement signal of each channel at multiple readings with an appropriate impulse response function that models the afterglow characteristics. In this case, a sum of decaying exponential functions can be used. The model parameters can be acquired by measuring the afterglow characteristics of the scintillator material [Leco 06].

Performance Improvement

Additional modifications were developed to allow to sacrifice precision for reducing the simulation time. These speed-up techniques are optional and some can be parameterized to provide a fine grained adaption of the simulation process:

Masking: The computation time is linearly dependent on the total amount of incoming X-ray photons. For simulating whole CT-scans most time is spent on simulating sinogram regions that are exposed to direct radiation even though these regions

contain little information on the detector performance and do not have a major influence on the image quality after reconstruction. In many cases the computation time can be reduced by masking those regions prior to simulation. This can be done by comparing the input sinogram with an I_0-reading which is only exposed to direct radiation. It is necessary to simulate at least one I_0-reading for a full scan simulation, since it is needed to convert measured intensities into attenuation values. This operation called *air calibration* was introduced in Sec. 1.6.4. The simulated air calibration data allows to unmask the result using the simulated I_0-reading. It is recommended to simulate multiple I_0-readings for two reasons: Firstly, a low-noise I_0-reading is needed to generate a sinogram of attenuation values from intensity values, secondly varying I_0-readings can be used for unmasking, otherwise the same noise pattern would repeat in the unmasked regions. Pre-computed I_0-reading results may be reused for later simulations with same detector geometry and X-ray tube settings as they are object-independent. Figure 2.3b shows a diagram containing all necessary steps for a complete CT scan simulation including masking and I_0 simulation.

Total Cross-Talk Simulation: The usage of a total cross-talk LUT offers the possibility to trade accuracy for speed. The total cross-talk LUT combines X-ray photon interaction and optical photon transport properties. It contains numbers of detected optical photons in a defined neighborhood around an irradiated pixel for a fixed amount of incoming X-ray photons. This LUT can be computed in advance from the photon interaction LUT and the optical photon distribution LUT data for a very large amount of incoming X-ray photons. This is done separately for each energy bin to preserve the energy dependence of the input data. This LUT offers only one total optical photon distribution for each energy bin.

The usage of this LUT requires the following steps for each channel, reading and energy bin of the input data:

1. Retrieve the number of detected optical photons in each pixel within the neighborhood of the current channel (look-up in total cross-talk LUT).

2. For each pixel in this neighborhood: Scale this value with respect to the number of X-ray photons in the current energy bin of the input data.

3. Take a random sample of a Poisson distribution with its mean value from previous step.

4. Add the resulting value of detected optical photons to the respective pixel signal of the output data.

The decision for using this LUT or the separated X-ray interaction and optical photon transport LUTs can be triggered with a threshold: If the amount of incoming X-ray photons exceeds the threshold within an energy bin, the scaled values of the total cross-talk LUT can be used to directly calculate the amount of optical photons reaching the neighboring photodiodes. This approach is several orders of magnitude faster than computing the optical cross-talk separately for each X-ray photon. Its time consumption is independent of the X-ray flux and depends linearly on the number of detector channels and read-outs per channel. However, it does not offer the high

precision of the approach using separated LUTs. The threshold value can be used to steer the trade-off between speed and precision.

2.2.3 Results

We evaluate two possible applications of this type of simulation: The estimation of the image MTF and the detector NPS. All results presented in the following section are based on simulations of Gd_2O_2S:Pr scintillators. The X-ray photon interaction events were precomputed using a proprietary particle interaction simulation[1]. In all cases the total cross-talk simulation was not used to get the maximum accuracy of the simulation.

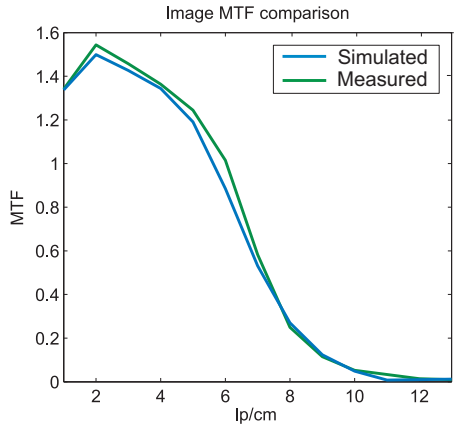

(a) Image MTF comparison

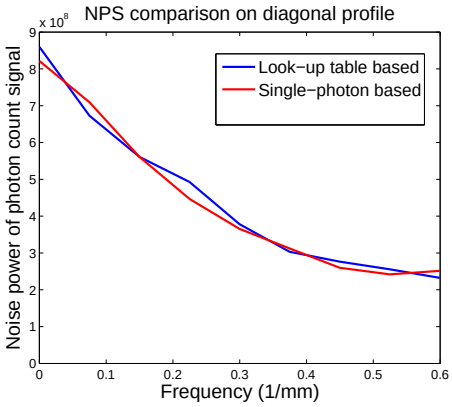

(b) Simulated NPS comparison

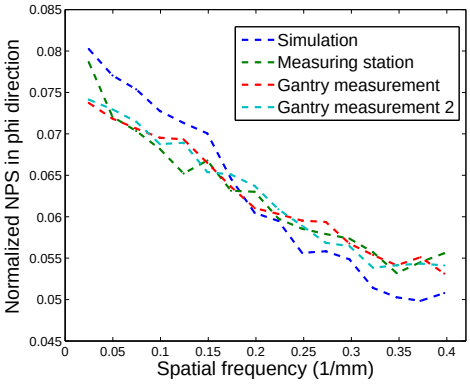

(c) NPS in ϕ-direction

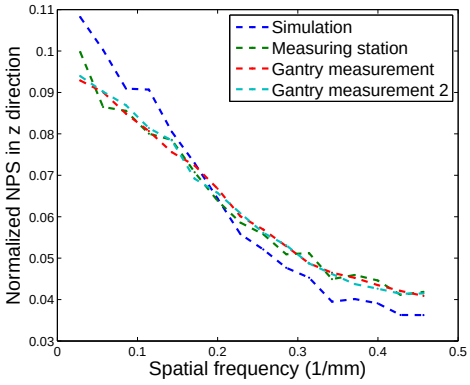

(d) NPS in z-direction

Figure 2.6: (a) Image-MTF comparison; (b) detector NPS comparison (profile of 2D-NPS along diagonal of 1st quadrant) between proposed simulation and full scale Monte-Carlo simulation; (c) and (d) NPS comparison between simulation and different measurements in measuring station and CT gantry. Measurements were conducted by Daniel Niederlöhner, Siemens Healthcare, Forchheim, Germany.

[1]The proprietary X-ray particle interaction simulation *moccasim* by Karl Stierstorfer (Siemens Healthcare, Forchheim, Germany) was used to obtain the interaction data for the CloudLUT.

Image MTF Comparison: With this experiment we examine the principal possibility to conduct complete CT scan simulations with this simulation framework. A detector with 672 channels in 32 rows with 1.3 mm ϕ-pitch and 1.1 mm z-pitch was simulated. The results were compared to measured data of a Siemens Sensation 64 CT-scanner. A high-contrast phantom was used[2]. The phantom contains inlays of line-patterns with increasing number of line pairs per cm (lp/cm). It is used to estimate the frequency resolution of the reconstructed image.

Figure 2.6a shows a comparison of measured and simulated image MTFs for an average body reconstruction kernel. In general, we observe a very good agreement between measured and simulated MTF with a slight underestimation of the MTF in the low to middle frequency range. The average error of the simulated MTF in the range of 1 to 10 lp/cm is 3.68%.

This kind of simulation, however, includes many parameters that are not related to the detector characteristics, for instance tube and reconstruction properties. Therefore we performed further tests that focus on the detector properties.

Detector NPS Estimation: In order to verify the simulation performance independently of the influence of other system parameters we compute the detector NPS from simulated and measured data. The NPS can be computed from the detector signal response to an X-ray flat-field. It contains information on the signal noise level and the modulation transfer characteristics of the detector. For a detailed explanation of the detector MTF see Sec. 1.7.

First we compare simulated NPS results of our look-up table-based approach with those of a fully single-photon based Monte-Carlo simulation. Both do not include electronics simulation. The later approach is very precise but extremely time consuming and therefore not feasible for most simulation scenarios. The detector NPS estimates from a flat-field image of 512×512 detector pixels and low intensity radiation are compared for both approaches. The simulation with our approach took 8:15 minutes on an Intel Core2Duo T5500 at 1.66 GHz with single-threaded simulation and total cross-talk optimization turned off (see Sec. 2.2.2 for details). The average deviation of the NPS values is 3.06%. Figure 2.6b shows a comparison of a diagonal profile of the 2-D NPS. This approach is about 200 times faster than the full-scale MC simulation.

The second detector NPS evaluation compares measurements taken from the CT gantry and a detector measuring station and the simulation tool. The simulation includes electronics post-processing, total cross-talk optimization is turned off. The results are shown in Fig. 2.6(c) and (d). The NPS values between simulation and gantry measurement again show a good agreement with an average relative deviation of 5.23 % in ϕ-direction. A comparison of the shapes of the NPS shows a faster drop off towards higher frequencies in the simulated NPS. This indicates a slight overestimation of the cross-talk.

[2]Catphan 500, *http://www.phantomlab.com/catphan.html*, The Phantom Laboratory, Salem, NY, USA

2.3 Directly Converting Counting Detectors

2.3.1 Simulation Principles

The scintillation detectors covered by the previously introduced simulation are currently the standard in medical CT, nevertheless there are alternative X-ray detector technologies available. One of these detector types is called directly-converting detector. The basic working principles of this technology were introduced in Sec. 1.4. Medical CT can benefit from directly-converting counting detectors due to their superior low-signal properties and there ability to perform energy selective measurements. As yet there is little expertise with this type of detectors in commercially available clinical CT systems, a precise detector model is required for developing such a system. This section presents a realization of the look-up table-based approach for the simulation of counting detectors on X-ray photon level.

The proposed simulation approach processes incoming spectra of X-ray photons, simulates the measurement process shown in Fig. 1.9 and yields photon count numbers measured by the detector. Like the previously introduced simulation it uses precomputed look-up tables that hold complex simulation data covering different physical effects. The contents of the LUTs are either taken from Monte-Carlo simulations or contain data gathered from measurements. Each LUT is valid for a specific set of detector layout parameters. Changing a layout parameter requires re-calculation of the affected LUTs. Independent effects of the detection process are grouped into simulation modules. The detector simulation efficiently cascades these modules and can be adapted to various counting detector types and layouts.

The following physical effects are covered by this approach:

- **Poisson distributed measurement noise:** The generation of X-ray quanta is a random process. The numbers of detected quanta per energy are Poisson distributed (similar to Sec. 2.2).

- **Photon interactions in the detector material:** Similarly to the simulation introduced in Sec. 2.2, the interaction events caused by the photoelectric effect or Compton scatter within the detector have to be simulated according to X-ray energies and detector composition and layout. Unlike the scintillators covered in the previously introduced simulation, the semiconductor is fully homogeneous. Septa made of a different material do not have to be considered. Therefore it is sufficient to store interaction positions relative to the photon impact location instead of absolute locations within the pixel. This greatly reduces the required amount of precomputed random interactions.

- **Electrode pulse generation:** X-ray interactions in the semiconductor material generate electron clouds which travel towards the anode. This process has to be modeled analytically in order to compute the induced electric current signals on the electrodes.

- **Read-out electronics:** The electric current signals are processed by a comparator and the resulting photon count signals are digitized. The influence of the sampling frequency of the simulated signals has to be considered.

- **Electrode signal processing:** The digital electrode signal is processed in order to compute the photon count output values. Different processing strategies have to be supported.

The photon interaction data as well as signal characteristics are provided in the form of detector-specific look-up tables. The photon interaction data is generated by a Monte-Carlo simulation of particle interactions. For this simulation, the ROSI framework [Gier 03] was used. The associated electrode signals are precomputed for a limited number of discrete locations based on a physical model [Krei 08]. The detector electronics behavior is also modeled. The validity of the simulation results is verified with measured data.

Figure 2.7 shows the steps of the detection process of a counting semiconductor detector. This illustration corresponds to Fig. 2.2 for integrating scintillator detectors.

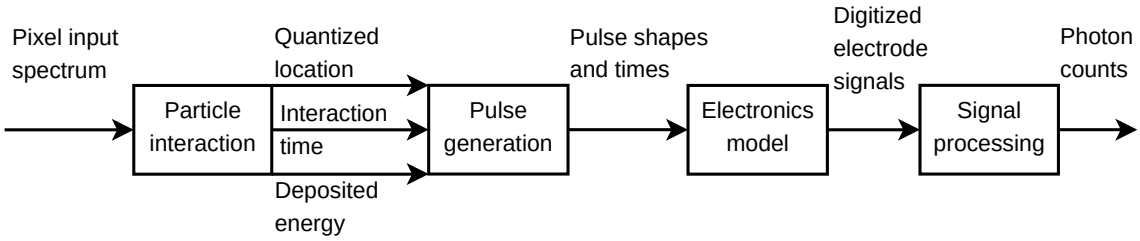

Figure 2.7: Detection steps and interfaces for counting semiconductor detectors.

2.3.2 Simulation Elements and Workflow

Table 2.2 shows an overview of all LUT and simulation data types.

LUT / data type name	**Indexed by**	**Content type**
Input data	Channel, reading, energy bin number	Mean X-ray photon number
CloudLUT	Energy bin number	Interaction data (see Tab. 2.3)
PulseLUT	Relative interaction location	Sampled electrode pulse
PulseShapingLUT	Pulse energy	Pulse stretch factor
ThresholdLUT	Threshold type, threshold number	Threshold value
Output data	Channel, reading, threshold type, threshold number	Photon count value

Table 2.2: LUT and simulation data types used for counting semiconductor detector simulation.

Description	Example value
Interaction number	0
Relative 3-D location (μm)	$(0.6; 1.0; 665.4)$
Deposited energy	47.4 keV
Interaction number	1
Relative 3-D location (μm)	$(229.6; -67.0; 898.6)$
Deposited energy	23.0 keV

Table 2.3: Example event dataset taken from the energy bin from 70 to 75 keV and consisting of two interactions.

Input Data: The input data consists of discretized energy spectra of mean values of incoming X-ray photons for all detector pixels and readings. For a complete CT scan simulation an input sinogram can be generated with an analytic projection tool. It calculates the intersection lengths of all rays with a geometrically defined phantom. The attenuated tube spectrum for each ray can be computed using the attenuation coefficients of the phantom materials and the corresponding intersection lengths.

CloudLUT: This LUT is produced with a Monte Carlo particle interaction simulation like ROSI [Gier 08] resp. Geant [Agos 03, Alli 06]. It yields electron cloud data generated by interactions of X-ray photons impinging perpendicular on a bulk semiconductor sensor, saved relative to the position where the photon penetrated the sensor. One X-ray photon may interact at several locations in the sensor caused e.g. by Compton scattering or fluorescence photons. This results in energy deposition in several charge clouds. The CloudLUT contains many random events per energy bin, in our tests we used 10^5 events per bin. This amount turned out to be sufficient to avoid LUT-induced regularities in the results. The incoming photon energy distribution is assumed to be homogeneous within any energy bin. Each photon event is described by the number of charge clouds and the center of mass location, cloud size and the deposited energy for each charge cloud. An example event dataset is shown in Tab. 2.3.

As this layout only saves relative interaction locations, it only supports simulating homogeneously illuminated detector pixels. Several applications, however, require inhomogeneously irradiated pixels. MTF measurements, for instance, are conducted using a slit collimator placed onto the detector. Here, the slit-width may be well below the pixel size. In order to simulate such a measurement, the interaction locations of the CloudLUT can be converted to absolute locations by randomly placing events from the standard CloudLUT at absolute locations that represent the slit geometry. The modified CloudLUT with absolute event locations can be used for simulations with arbitrary irradiation patterns and only minor adaptions in the simulation work flow are necessary, but one absolute CloudLUT is only valid for one given geometry.

PulseLUT and PulseShapingLUT: These LUTs contain data on how charge clouds generated at specific discrete positions are converted into time dependent signals. The conversion is done in two subsequent operations: First, the location and

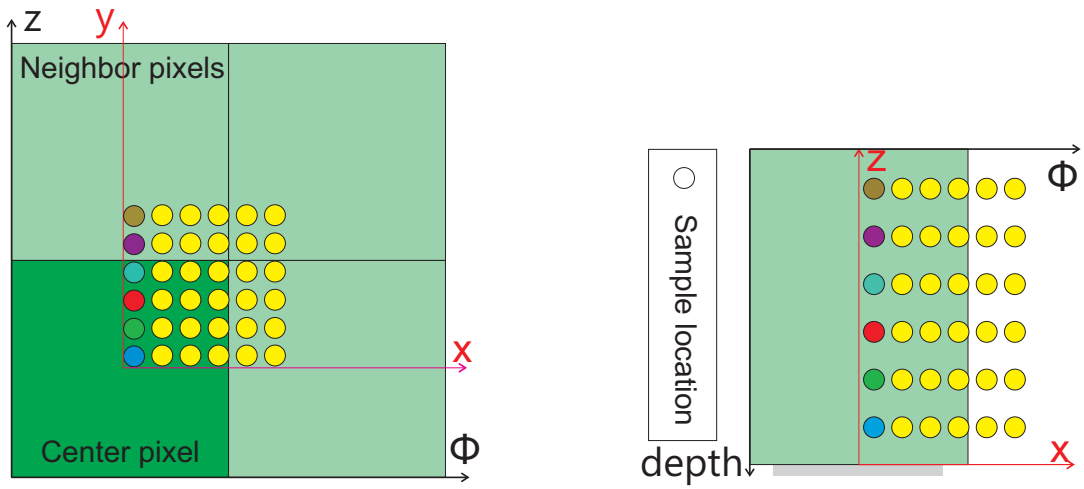

(a) Top view (b) Side view

Figure 2.8: Pulse sample locations of a standard PulseLUT. Locations outside center pixel denote induced pulses by interactions in neighboring pixels. Color coded locations correspond to pulses plotted in Figs. 2.9 and 2.10. Color codes do not indicate a correspondence between Figs. (a) and (b). The red coordinate axis indicate the LUT-internally used detector pixel (x, y, z)-coordinate system also used in Figs. 2.9 and 2.10.

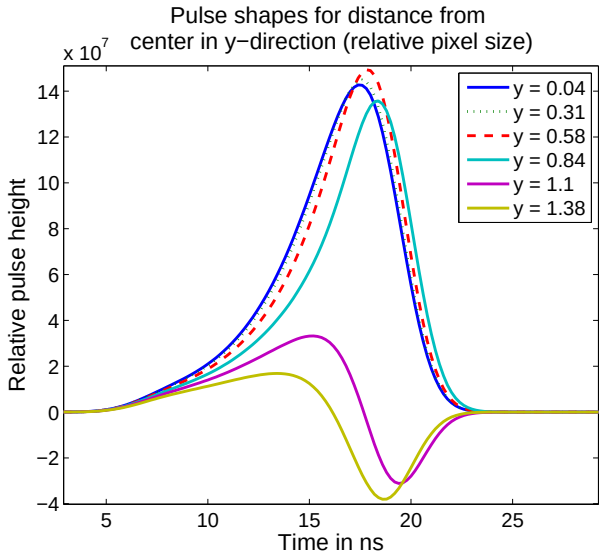

Figure 2.9: Example pulses for pulse locations marked in top view of Fig. 2.8. The colors of bullets marking the sample locations in Fig. 2.8a and function plots are matched.

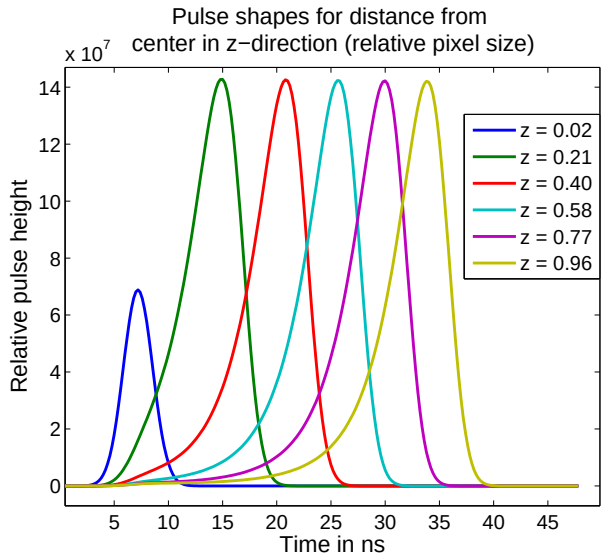

Figure 2.10: Example pulses for pulse locations marked in side view of Fig. 2.8. The colors of bullets marking the sample locations in Fig. 2.8b and function plots are matched.

energy information is transcribed into a signal pulse by the PulseLUT, and secondly more complex correlations of the pulse shape can be modeled by the PulseShapingLUT which modifies the pulse height at given area. The PulseLUT is the result of the adjoint induction problem [Krei 08] solved with the finite element software COMSOL (COMSOL AB, Stockholm, Sweden). The adjoint induction problem results in the *charge-induction-map* (CIM) for each time step. The CIM is converted into a electric current pulse for any location of the charge cloud inside the corresponding pixel volume. For every position inside the hit pixel also the induced signals on all directly neighboring pixels are stored and processed for a 3×3 pixel neighborhood. Each current pulse is convolved with the shaping characteristics of the electronics. The stored pulses yield a direct correlation of pulse height and amount of charges (pulse area). The PulseShapingLUT allows to change the pulse height-to-charge relation with respect to the energy of a pulse.

Figure 2.8 shows the sampling grid of a standard PulseLUT and Figs. 2.9 and 2.10 show sample pulses for the marked grid locations. Note that for pulses induced by charge clouds in neighbor pixels ($y = 1.1$ and $y = 1.38$ in Fig. 2.9) the current gets negative as the charge cloud reaches the neighbor electrode.

Since the pulses of PulseLUT are simply scaled with the respective energy, pulse height and area are related linearly. In order to model a realistic relation between pulse height and area, these quantities have been assessed with a measurements from a probe card (see Fig. 2.11). These results are incorporated in the PulseShapingLUT, which provides an energy dependent stretch factor that is used to alter the area-to-height ratio of each individual pulse by resampling.

Electronics Noise Generator: The signal processing stage is influenced by various effects of the detector electronics like amplification or quantization noise. These

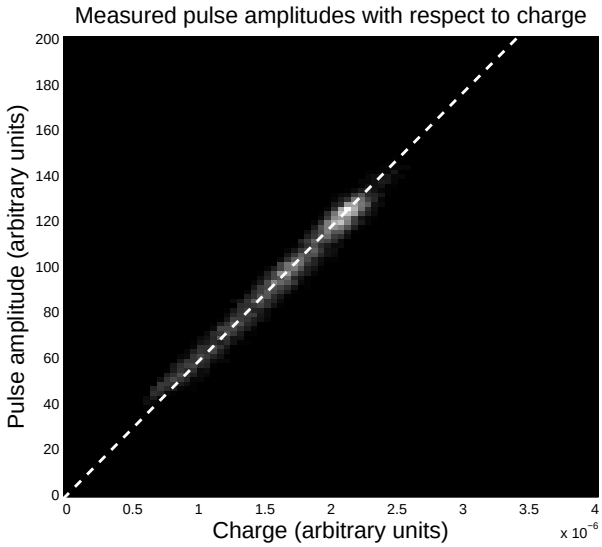

Figure 2.11: Measured relation between pulse amplitude and charge. Hatched line indicates ideal linear relationship. Slight deviations from the ideal line can be observed for low charges. Data from Daniel Niederlöhner, Siemens Healthcare, Forchheim, Germany.

effects are incorporated into the simulation by adding a colored noise signal to the ideal electrode signal from the signal generation stage. This noise signal can be provided by noise measurements or an electronics noise simulation which takes noise correlations and variance into account.

ThresholdLUT: The ThresholdLUT contains a set of discriminators which are used to process the signal. Each discriminator is associated with an arbitrary number of signal thresholds and optional additional discriminator parameters. A very simple discriminator counts the times a given detector signal exceeds a threshold (*rising edge discriminator*). The *clocked discriminator* sub-samples the signal and counts the number of samples where the signal exceeds a threshold. More sophisticated discriminators can be introduced that reduce paralysis effects caused by the fact that with increasing flux, pulse signals overlap (*pile-up*) and the characteristics of the individual pulses can hardly be identified from the signal.

Basic Simulation Work Flow: Figure 2.12 shows the basic signal flow of the simulation process. The *Interaction Event Generator* picks random events from the *CloudLUT* according to the input spectra. A Poisson distributed noise operator is then applied to the mean photon numbers of each energy bin. The events are distributed equally over the respective pixel surface and the absolute locations of the resulting electron clouds are computed. Each drawn event gets a random time offset within the selected reading time. An event may contain an arbitrary number of interactions. For all absolute interaction locations a quantized position within the according detector pixel is calculated. From the quantized interaction location the according pulse shape indices are gathered from the *PulseLUT*. An interaction

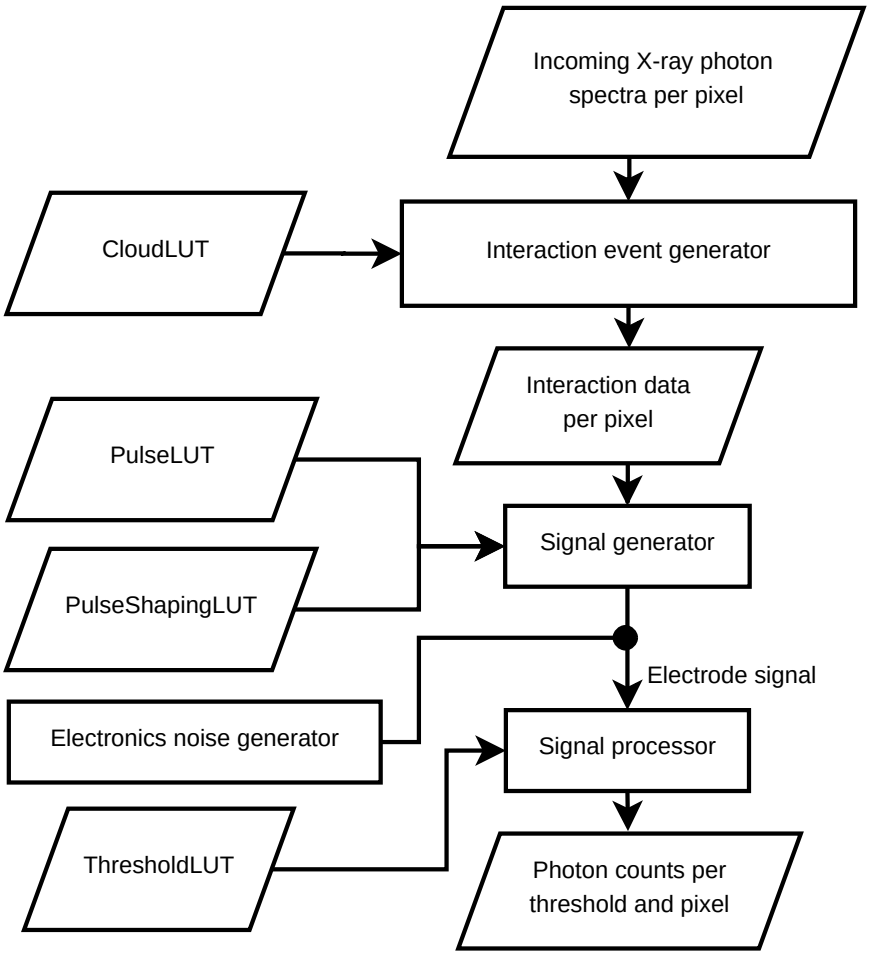

Figure 2.12: Basic model of the simulation signal flow.

location can be associated with multiple pulses on different anodes as an electron cloud induces pulses on several proximate anodes. For each detector pixel all pulse data are gathered in an intermediate *Interaction Data Stack*. When all interactions are generated, the *Signal Generator* processes the interaction stacks: Firstly, a noise signal is generated that covers the whole reading time. Then, for each interaction the according pulse is scaled and shaped according to the interaction energy and added to the signal with respect to its time offset. The resulting signal represents the read out electrode signal of one reading. The *Signal Processor* generates the pixel photon counts from this signal. It uses an arbitrary number of thresholds which can be defined individually for each pixel in the *ThresholdLUT* together with a discriminator. The output sinogram consists of counts for each threshold, detector pixel and reading.

Complexity and Optimization: The influence of the simulation parameters on the simulation time is very different for the two simulation stages *signal generation* and *signal processing*. These two stages are alternated for each pixel.

The computation time of the signal generation stage mostly scales with the total number of incoming photons and their average energy, as these two quantities influence the number of interactions. The computation time of the signal processing stage is mostly governed by the total integration time over all readings and the pre-defined sampling frequency of the pulses and signals. The X-ray flux has only a minor influence on the computation time of this stage. The computation time of phase one scales linearly with the total number of interactions, phase two scales with product of the number of simulated pixels times the number of samples per signal.

Two optional preprocessing steps are available to speed up the simulation: Directly irradiated areas can be removed by comparison with an input reading of an air scan. As the computation time of the signal generation part scales with input X-ray intensity, removing directly irradiated areas may reduce the simulation time significantly, depending on the size of these areas.

Secondly, the input data is divided into sub-regions that are processed in parallel, so each sub-region is processed by an individual computation thread. As the effect of cross-talk from neighboring pixels has to be covered, the sub-regions should overlap. The size of the overlap is determined by the maximal cross-talk range. Each thread writes its result data into an exclusive region of the common result structure. Thus, almost no synchronization between threads is needed and the simulation time scales well with the number of simulation threads. The optimal size of the sub-regions depends on the total number of interactions within one sub-region and the desired memory consumption for one computation thread. Performance and memory usage can benefit from a non-equidistant division into sub-regions that takes the input photon numbers within the sub-regions into account and assures similar photon counts in each sub-region.

2.3.3 Results

Run-Time and Memory Usage: Run-time and memory usage depend very much on the input data and the sampling time for the electrode signals. Setting the maximum size of the interaction data stack allows to steer a trade off between performance

and memory usage. This way full scan simulations may consume from less than one up to several GBs of memory depending on input data and signal sampling rate. A full scan of a water cylinder phantom with a diameter of 40 cm with a detector of 2475 pixels, 1600 readings and a reading time of 1 ms using a sampling time of 2 ns takes 8 h on a workstation equipped with 4×2 AMD 885 Opteron cores at 2.6 MHz and 16 GB of RAM.

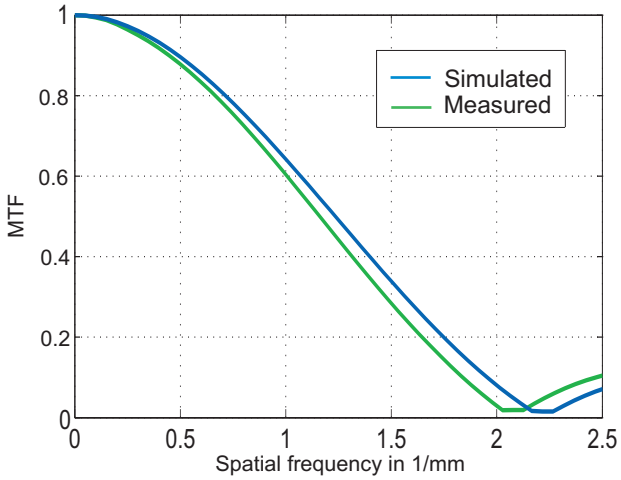

Figure 2.13: Comparison of measured and simulated MTF estimate. The fluorescence photons yield a crosstalk-like behavior which results in a slightly decreased MTF.

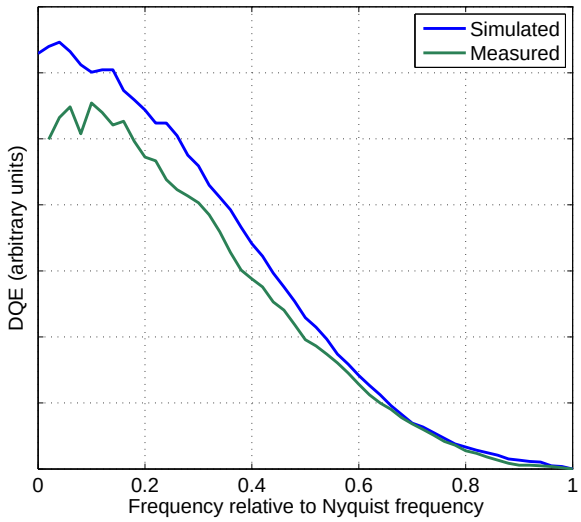

Figure 2.14: Comparison of measured and simulated DQE estimate.

Comparison with MTF and DQE Measurements: For comparison of simulation and measurements we used various quantities like linearity, spectral behavior, DQE, etc. As an example we compare the measured and simulated detector MTF of

one combination of detector parameters here. All the results produced by our simulation are in good agreement with the measurements we have acquired[3]. Figure 2.13 compares the MTF curves from the simulation and a measurement conducted with a single detector module. The simulation was conducted using the proposed modified CloudLUT for inhomogeneous pixel illumination (see Sec. 2.3.2).

This MTF estimate was used together with a NPS estimated from a simulated and measured flat-field illumination to compute the DQE of the detector model. This comparison is shown in Fig. 2.14. Here, a good agreement in terms of shape can be observed. The difference with respect to scale can be attributed to an increased noise level in the measured data due to the detector module, which is not covered by the noise signal generator part of the simulation.

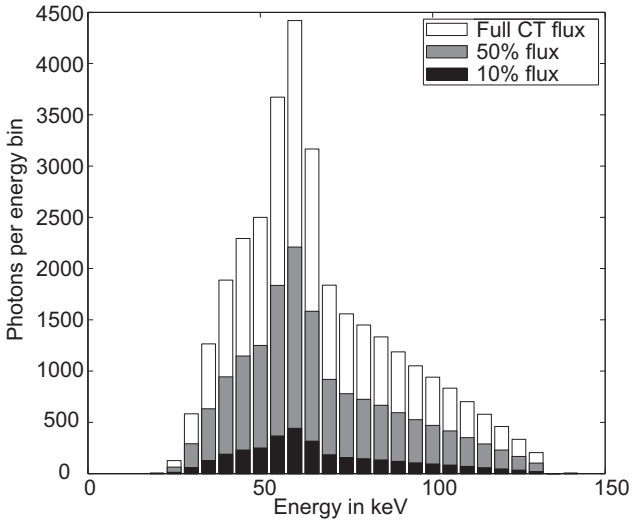

Figure 2.15: Discretized 140 kVp input spectra for full, half and 10% CT flux with an energy bin width of 5 keV.

Detector Signal at Various Flux Levels: For this experiment a detector with a pixel area of 0.05 mm^2 and 1.0 mm depth was simulated. For each pixel, a typical 140 kVp tube spectrum containing a total of approximately $3.2 \cdot 10^4$ X-ray photons for the full flux case was used as input (see Fig. 2.15). The total signal length for one reading is 2.14 ms and the sample time of pulses and signal was 2.0 ns. Pulses where shaped to 21 ns *full width half maximum* (FWHM). Figure 2.16 shows excerpts of the according detector signal prior to the signal processing stage. The 10 % flux case shows distinguished pulses, in the half flux case, some pile-up can be observed. The full flux case shows a huge amount of pile-up which renders the detection of individual events and their respective energy very difficult.

[3]All measurements were conducted at Siemens Healthcare CT (Forchheim, Germany) by Daniel Niederlöhner and Edgar Kraft.

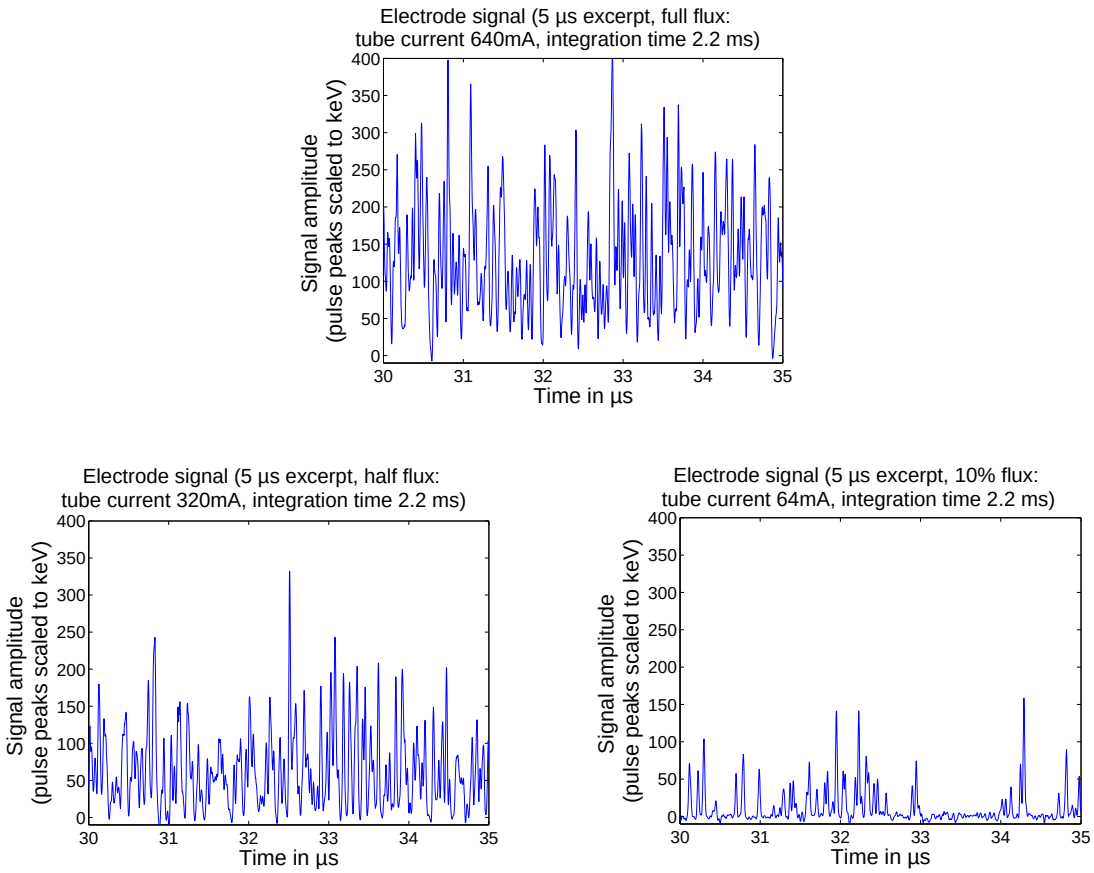

Figure 2.16: Resulting detector signals for spectra of Fig. 2.15.

Detector Linearity: In order to demonstrate the influence of signal pile-up we show the performance of a simple rising edge discriminator on signals like the ones depicted in Fig. 2.16. Figure 2.17 shows the resulting counts for thresholds from 15 to 75 keV with respect to the relative CT flux. Up to approx. 10% of the full CT flux, all thresholds show a linear counting behaviour. For higher flux, the count signals start to paralyze especially for lower thresholds. At a flux level at approx. 90 % of the maximum CT flux, the signal level remains above a low threshold when strong signal pile-up is observed. This causes a decrease in counted photon numbers with increasing flux. In order to deal with high flux levels, a more sophisticated discriminator and additional linearity corrections are required. Figure 2.18 shows a linearity comparison between measured data from a prototype detector element and simulated data on a logartihmic scale. Deviations between measurement and simulation are mostly present in the low-flux area with a slight overestimation of the counts for the 30 keV threshold whereas the 60 keV threshold shows an underestimation of the counts. For the very low-flux case and the 60 keV threshold the error is maximal with approx. 30 %. In the high-flux areas the paralysis of the detector can be observed at the same flux in both results. In this region, the match between simulated and measured counts is very good with errors well below 5 %.

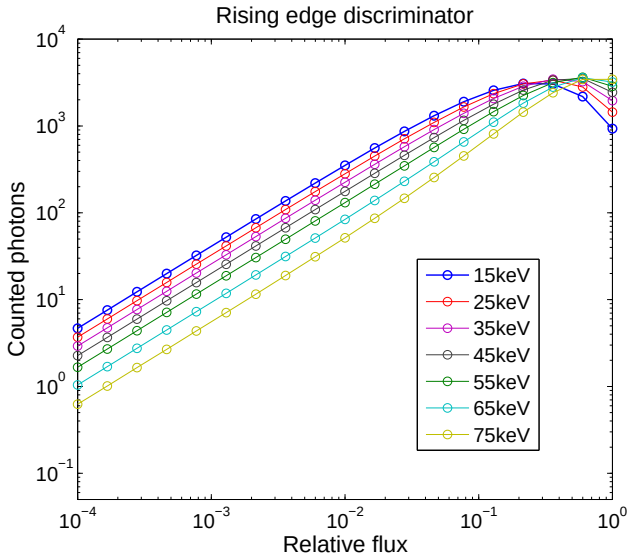

Figure 2.17: Count rate behavior of rising edge discriminator for various thresholds and flux levels.

Energy Transfer Probability: The spectral sensitivity of a counting detector is dependent on the selected thresholds. This property can be examined with the energy transfer probability of the detector. It shows the probability density for an X-ray photon of energy E of triggering a threshold corresponding to energy E'. Ideally this would be 1 for $E = E'$. In practice, of course, various physical effects and detector properties degrade the spectral detection performance as shown in Fig. 2.19. Besides the local maximum of the probability at $E = E'$, another prominent local maximum is observed at $E = E' - E_{\mathrm{f}}^{(i)}$. This is caused by fluorescence photons, which escape the

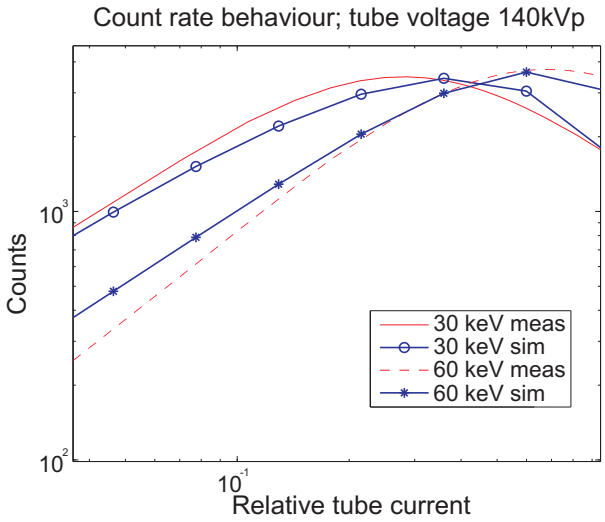

Figure 2.18: Simulated and measured linearity for two thresholds at 30 and 60 keV.

respective detector pixel and may be detected in another pixel. The energy / energies $E_{\mathrm{f}}^{(i)}$ depend(s) on the K-edges of the materials in the semiconductor. Here, i denotes the number of significant K-edges of the detector material. This effect also causes several counts at energies below the respective K-edge energy due to escape photons entering from neighboring pixels. The large number of counts at very low energies is mostly due to electronics noise. The observed effects are more prominent for the small pixel case, the difference image in Fig. 2.19c shows that the probability of correctly detecting photons at $E \approx E'$ decreases for smaller pixels in favor of erroneously detected photon energies at $E' < E$. This effect is caused by increased X-ray cross-talk and charge sharing within small pixels. Large pixels, however, show increased signal pile-up and paralysis for high flux levels. These effects were previously shown and discussed in the linearity and electrode signal evaluations.

2.4 Conclusions

We have introduced a new type of detector simulation that combines the precision of a Monte-Carlo particle simulation with the performance that is necessary to cover realistic scenarios such as complete CT scans. The simulation concepts can be used to study the influence of various parameters of a proposed detector design on the reconstructed CT image. Two realizations were presented: The first one covers the still most common CT detector technology of integrating scintillator detectors. The second simulation deals with photon-counting semiconductor detectors. This technology is still in an experimental stage for medical CT applications.

Both concepts were successfully validated with measured data. Two possible applications for the scintillator simulation were shown: Investigation of the effects of the detector on the MTF of the reconstructed image and a detector NPS estimation. The results show that our look-up table-based simulation models the detector performance sufficiently precise, so that its effects on CT image quality can be ex-

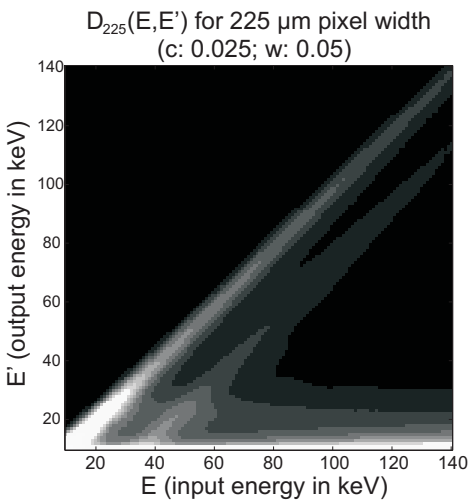

(a) $0.05\,\mathrm{mm}^2$ pixel size.

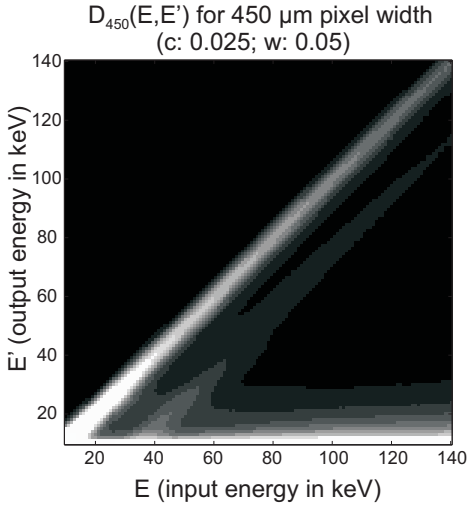

(b) $0.20\,\mathrm{mm}^2$ pixel size.

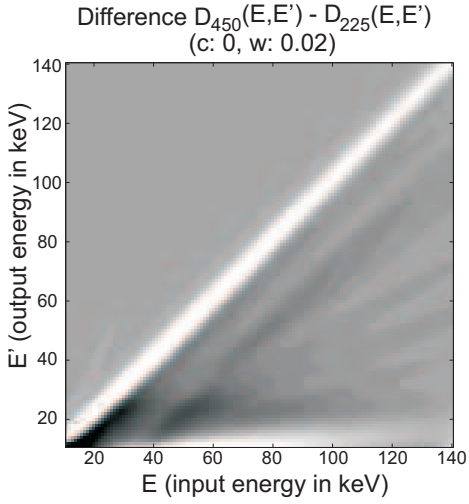

(c) Difference image.

Figure 2.19: Energy transfer probability for X-ray photon of energy E and thresholds corresponding to energies E'. (a): Small pixels ($0.05\,\mathrm{mm}^2$), (b): large pixels ($0.20\,\mathrm{mm}^2$), (c): difference image. Intensity windows are for left and center image: Center 0.025, width: 0.05; Right image: Center 0, width: 0.02. The values reflect detection probabilities.

amined. In the investigated cases, the level of precision matches that of a full-scale MC simulation. For the semiconductor concept, a DQE comparison and a detector linearity test was performed in addition to the MTF test. Additional experiments were conducted that yield information which can hardly be retrieved from measurements with a prototype system. These additional studies comprised energy transfer probability assessment, electrode signal examination at various flux levels and a fine grained count rate behavior analysis.

Chapter 3

Quantitative CT

This chapter gives a general introduction into Quantitative CT and explains its most important elementary methods. Several basic scientific works on this topic are introduced and discussed. The main part focuses on a novel QCT framework called *Local Spectral Reconstruction* (LSR) and describes its application to a variety of traditional QCT problems. Additionally, new diagnostic possibilities of LSR are demonstrated and an in-depth evaluation of various performance aspects of LSR applications is performed. Theory and applications of the LSR were published in [Heis 09].

3.1 Concepts of Quantitative CT

Traditional single energy CT measures Hounsfield units $H(\mathbf{r})$ at position $\mathbf{r}$. They correspond to weighted attenuation coefficients $\bar{\mu}(\mathbf{r})$. Physically, the ground truth of the scanned object (e.g. patient) is the *energy-dependent* attenuation coefficient $\mu(E, \mathbf{r})$. The measurement process corresponds to a weighting of the physical ground truth $\mu(E, \mathbf{r})$ to the weighted $\bar{\mu}(\mathbf{r})$.

The spectral weighting is determined by both the measurement system and the scanned object itself. The main components of the measurement system are the X-ray source and the CT detector. The X-ray tube spectrum $S(E)$ defines the energy distribution of the tube quantum field (see Sec. 1.3). The CT detector has an energy-dependent detector responsivity $D(E)$. It describes the relative signal contribution of a quantum of energy E (see Sec. 1.4).

The product of the tube spectrum and the detector response function is normalized to one to yield $w(E)$ as the *System Weighting Function* (SWF):

$$w(E) = \frac{S(E)D(E)}{\int_0^\infty S(E')D(E')\mathrm{d}E'}. \tag{3.1}$$

For small objects, it approximates the local energy weighting. However, typical patient and object diameters in practical CT reach several tens of centimeters. In this case the self-absorption of the object shifts the local energy weighting to higher energies (see Sec. 1.6.3 *Beam Hardening*). Commercial CT systems typically employ beam hardening correction algorithms. Single energy beam hardening corrections reduce the typical beam hardening artifacts and provide homogeneous HU values for

identical material compositions throughout the CT volume. Generally, these methods cannot guarantee that the identical material gets the same HU values among scans of different surrounding objects or alternative system settings. Quantitative beam hardening corrections use multi-energy data to completely eliminate the effects of the surrounding object from the HU values of a given material. Methods like the polychromatic CT reconstruction from Yan et al. [Yan 00] incorporate the polychromatic nature of the tube radiation into a special iterative dual energy reconstruction method.

Fully quantitative CT approaches generally yield measures that are directly related to physical properties of the imaged object or tissue. Unlike Hounsfield units, these measures should not be system-dependent or be influenced by the surrounding object. The following sections introduce two quantitative methods: *Basis Material Decomposition* (BMD) [Alva 76] and Local Spectral Reconstruction [Heis 09]. The first one yields two or more effective basis material densities to characterize underlying material compositions. LSR provides a unified framework for QCT applications.

3.2 Basis Material Decomposition

In general, the spectral attenuation coefficient of a material can be expressed as a linear combination of M energy-dependent basis functions $f_j(E)$:

$$\mu(E, \mathbf{r}) = \sum_{j=1}^{M} c_j(\mathbf{r}) f_j(E). \tag{3.2}$$

We have shown in Sec. 1.6.1 that the spectral attenuation coefficients of body materials are dominated by two effects in the energy range of medical CT: photoelectric absorption and Compton scattering. This is the basic principle behind BMD. Since two basis materials are sufficient to express $\mu(E, \mathbf{r})$ for body materials with very small errors in the energy range of medical CT, a separation of the the energy-dependent basis functions $f_j(E)$ from the spatially-dependent coefficients $c_j(\mathbf{r})$ is possible. The typical choice for basis functions in medical CT is a set of water and bone mass attenuation functions [Hawk 86, Vett 86]. We denote the basis functions $f_{\mathrm{W}}(E)$ and $f_{\mathrm{B}}(E)$. The $f_{\mathrm{W}}(E)$-component corresponds to the mass attenuation coefficient of water and $f_{\mathrm{B}}(E)$ to femur bone. The compositions were chosen according to [ICRU 92]. The according basis material coefficients are denoted $c_{\mathrm{W}}(\mathbf{r})$ and $c_{\mathrm{B}}(\mathbf{r})$. For this basis material set, Eq. (3.2) reads:

$$\mu(E, \mathbf{r}) = c_{\mathrm{W}}(\mathbf{r}) \cdot f_{\mathrm{W}}(E) + c_{\mathrm{B}}(\mathbf{r}) \cdot f_{\mathrm{B}}(E). \tag{3.3}$$

In the original BMD publication, Alvarez et al. [Alva 76] suggested the physically motivated basis-material set of mass attenuation functions corresponding to a Compton scatter and a photoelectric absorption component. The mass attenuation due to photoelectric absorption can be modeled as $f_{\mathrm{PA}}(E) = \frac{1}{E^3}$. The Compton scatter basis function is modeled with the Klein-Nishina formula $f_{\mathrm{KN}}(E)$. See [Klei 29] for a definition of $f_{\mathrm{KN}}(E)$.

For this parametrization, however, the accuracy of the basis material representation is reduced, as the basis function $f_{\mathrm{PA}}(E)$ does not model the photoelectric

absorption (see Fig. 1.15b) exactly. Thus, basis functions that represent compositions of dominant materials or compositions like water and bone are used. Generally, solving the BMD is an ill-posed problem which results in an increased sensitivity to noise in the measured data. Weaver and Huddleston [Weav 84] alleviate this effect by performing a principal-components analysis on various body tissue attenuation functions. This yields an optimally separated set of orthogonal basis-functions. Stenner, Kachelrieß et al. [Sten 07, Kach 06] have proposed an empirical Dual Energy calibration that yields a set of decomposition functions that does not require the knowledge of X-ray spectra, detector sensitivities and attenuation coefficients.

The water / bone set is still very popular as it offers a good separation of the basis functions and physically meaningful basis material coefficients. Special attention has to be paid to the presence of contrast agents as these usually contain elements with an atomic number greater than 25, for instance, iodine or gadolinium. This means that their K-edge lies in the relevant energy range of medical CT. The elements have to be contained in the set of basis materials in order to be able to model the observed spectral attenuation coefficients precisely [Hawk 97].

3.2.1 Projection Data-Based BMD

Inserting Eq. (3.2) into the line integral of the spectral attenuation law of Eq. (1.6) yields:

$$\int_0^\infty \mu(E, \mathbf{l}_{\theta,t}(\alpha))\mathrm{d}\alpha = f_\mathrm{W}(E)\int_0^\infty c_\mathrm{W}(\mathbf{l}_{\theta,t}(\alpha))\mathrm{d}\alpha + f_\mathrm{B}(E)\int_0^\infty c_\mathrm{B}(\mathbf{l}_{\theta,t}(\alpha))\mathrm{d}\alpha \quad (3.4)$$

We denote the line integral over the water coefficients $A_\mathrm{W}(\theta,t) = \int_0^\infty c_\mathrm{W}(\mathbf{l}_{\theta,t}(\alpha))\mathrm{d}\alpha$, the integral $A_\mathrm{B}(\theta,t)$ over the bone coefficients is defined analogously. The beam geometry is illustrated in Fig. 1.16b.

Conducting a dual energy measurement at two energy weightings $S_1(E)D_1(E)$ and $S_2(E)D_2(E)$ gives the following system of non-linear equations:

$$I_1(\theta,t) = \int_0^\infty S_1(E)D_1(E)\exp\left\{-f_\mathrm{W}(E)A_\mathrm{W}(\theta,t) - f_\mathrm{B}(E)A_\mathrm{B}(\theta,t)\right\}\mathrm{d}E \quad (3.5)$$

$$I_2(\theta,t) = \int_0^\infty S_2(E)D_2(E)\exp\left\{-f_\mathrm{W}(E)A_\mathrm{W}(\theta,t) - f_\mathrm{B}(E)A_\mathrm{B}(\theta,t)\right\}\mathrm{d}E \quad (3.6)$$

This system has to be solved for $A_\mathrm{W}(\theta,t)$ and $A_\mathrm{B}(\theta,t)$. For a survey on numerical solvers for systems of non-linear equations see [Burd 01] pp. 600. Then the basis material coefficients $c_\mathrm{W}(\mathbf{r})$ resp. $c_\mathrm{B}(\mathbf{r})$ can be recovered from $A_\mathrm{W}(\theta,t)$ resp. $A_\mathrm{B}(\theta,t)$ with a plain inverse Radon transform as used for standard CT reconstruction. However, this approach is prone to reconstruction artifacts as noise in the measured $I_1(\theta,t)$ and $I_2(\theta,t)$ may lead to inaccurate solutions of the system of non-linear equations (Eqs. 3.5, 3.6). This causes inconsistencies in the forward projected basis material coefficients $A_\mathrm{W}(\theta,t)$ and $A_\mathrm{B}(\theta,t)$ which appear as streak artifacts in the reconstructed $c_\mathrm{W}(\mathbf{r})$ and $c_\mathrm{B}(\mathbf{r})$ values, as the contributions from different directions do not match accurately. This generally produces streak-artifacts in FBP-like reconstruction methods.

A general drawback of projection data-based methods is the requirement of perfectly matched raw-datasets and not all dual-energy detection techniques (see Sec. 1.5) are able to produce perfectly matched raw-data.

3.2.2 Image-Based BMD

Image-based BMD avoids this problem by performing the BMD in the image domain. For this purpose, the reconstructed attenuation values need to correspond to a constant, known energy weighting throughout the CT volume. For data measured with a polychromatic source, this can be achieved by a quantitative beam hardening correction such as [Yan 00]. It homogenizes the energy weighting throughout the reconstructed CT volume. The homogenized energy weighting is denoted $\tilde{w}_i(E)$. Here, i numbers the N_i spectral measurements. As for projection data-based BMD, multiple measurements at different energy weightings are required. The relation between spectral attenuation coefficient and measured attenuation coefficient after beam hardening correction $\tilde{\mu}_i(\mathbf{r})$ is defined by the energy weighting:

$$\tilde{\mu}_i(\mathbf{r}) = \int_0^\infty \tilde{w}_i(E)\mu(E,\mathbf{r})\mathrm{d}E \tag{3.7}$$

With an arbitrary BMD of $\mu(E,\mathbf{r})$ (3.2), we get:

$$\tilde{\mu}_i(\mathbf{r}) = \int_0^\infty \tilde{w}_i(E)\sum_{j=1}^{M} c_j(\mathbf{r})f_j(E)\mathrm{d}E \tag{3.8}$$

Here, we can exchange summation and integration,

$$\tilde{\mu}_i(\mathbf{r}) = \sum_{j=1}^{M} c_j(\mathbf{r})\int_0^\infty \tilde{w}_i(E)f_j(E)\mathrm{d}E \tag{3.9}$$

and form the matrix $\tilde{\mathbf{K}} = [[\tilde{k}_{ij}]]$ with

$$\tilde{k}_{ij} = \int_0^\infty \tilde{w}_i(E)f_j(E)\mathrm{d}E. \tag{3.10}$$

The complete BMD with all measurements then leads to the following linear system of equations:

$$\tilde{\boldsymbol{\mu}}(\mathbf{r}) = \tilde{\mathbf{K}}\cdot\mathbf{c}(\mathbf{r}) \tag{3.11}$$

with $\tilde{\boldsymbol{\mu}}(\mathbf{r}) = (\tilde{\mu}_1(\mathbf{r}),\tilde{\mu}_2(\mathbf{r}),\ldots,\tilde{\mu}_{N_i}(\mathbf{r}))^T$ and $\mathbf{c}(\mathbf{r}) = (c_1(\mathbf{r}),c_2(\mathbf{r}),\ldots,c_M(\mathbf{r}))^T$ and $\tilde{\mathbf{K}} \in \mathbb{R}^{N_i\times M}$. Solving this system for $\mathbf{c}(\mathbf{r})$ yields the basis-material coefficients at location $\mathbf{r}$.

The quantitative accuracy of the image-based BMD approach depends on the accuracy of the beam-hardening correction and the image quality of the resulting basis-material images is reduced since the solution of Eq. (3.11) is very sensitive to noise in the input data. Advanced image-based material decomposition methods such as [Maas 09] have been developed to overcome these drawbacks.

3.3 Local Spectral Reconstruction

This section presents an image-based quantitative framework for spectral CT applications. It is referred to as *Local Spectral Reconstruction* [Heis 09]. The LSW approach can be used to perform a BMD without the need of a beam hardening correction. It calculates the spatially dependent local spectral weighting $\Omega(E, \mathbf{r})$ instead of homogenizing the energy weighting. Its application to BMD is demonstrated in Sec. 3.3.2.

3.3.1 Concept of Local Spectral Weighting

The central element of LSR is the *Local Weighting Function* (LWF) $\Omega(E, \mathbf{r})$. The LWF serves as the weighting function in the spectral integration of the physical ground truth $\mu(E, \mathbf{r})$ to the measured CT data $\bar{\mu}(\mathbf{r})$.

This has two main implications: On a fundamental level, it allows us to evaluate the spectral weighting process in arbitrary CT images. Energy weighting shifts can be expressed and evaluated in terms of the local energy weighting function. From an application point of view, the image-based link between ground truth and measured data enables a unified formulation of many spectral CT applications. These include beam hardening corrections, energy calibrations for CT, attenuation corrections for SPECT and PET as well as image-based Basis Material Decompositions or decompositions into density and atomic number.

We first review the impact of source, detector and scanned object in a spectral CT measurement. Based on this, an image-based formulation of the measurement process is derived. The main element is the LWF. We provide a novel iterative LSR algorithm for its calculation. In order to verify the framework, we investigate measured and simulated CT image data. We use measured images of a water and an abdomen phantom as well as simulated images of a human thorax with ground truth representations of the spectral attenuation coefficients. Both data sources are used to calculate and discuss the main properties of the LWF. As exemplary applications we perform beam hardening corrections to various target energy weightings, a calculation of an attenuation map for SPECT/CT and PET/CT and a quantitative iodine density estimation. The resulting attenuation coefficients are compared to the respective ground truth of the measured and simulated objects. The algorithmic convergence, as well as the quantitative accuracy and precision are analyzed. A direct material identification using the LWF result is demonstrated. We conclude by summarizing the potential applications of the LSR framework in quantitative spectral CT.

3.3.2 Theory

We briefly review the properties of X-ray attenuation measurements in general and the spectral measurement process in CT in particular. The dilemma between a correct physical description of the X-ray measurement and the limited measurement information in single-energy CT is discussed. The local energy weighting in CT is analyzed.

Spectral CT Measurements

With the parameterizations of source, object and detector introduced in Sections 1.3-1.6 we can integrate the concept of the System Weighting Function (SWF) into the description of the measurement process: The measured attenuation A is given by the ratio of the two measured intensities I and I_0 as

$$A = \frac{I}{I_0} = \frac{\int_0^\infty S(E)D(E)\exp\left(-\int_0^\infty \mu(E,\mathbf{l}_{\theta,t}(\alpha))\mathrm{d}\alpha\right)\mathrm{d}E}{\int_0^\infty S(E')D(E')\mathrm{d}E'} \tag{3.12}$$

The projection path is again parameterized with $\mathbf{l}_{\theta,t}(\alpha)$. For the sake of simplicity, the parameters angle θ and distance to origin t are omitted for A and I. We can write this as

$$A = \int_0^\infty w(E)\exp\left(-\int_0^\infty \mu(E,\mathbf{l}_{\theta,t}(\alpha))\mathrm{d}\alpha\right)\mathrm{d}E \tag{3.13}$$

with the definition of the SWF $w(E)$ of Eq. 3.1.

The SWF can be calculated from parameterizations of $S(E)$ and $D(E)$ or obtained by transmission measurements [Yan 99, Ruth 97, Sidk 05]. Figure 3.1 shows two SWFs for a typical Dual-kVp CT scan. The corresponding tube and detector parameterizations are found in Figs. 1.5a and 1.8.

For mono-energetic radiation with energy $E = E_0$ we have $w(E) = \delta(E - E_0)$[1], and Eq. (3.13) simplifies to

$$\ln(A) = -\int_0^\infty \mu(E_0,\mathbf{l}_{\theta,t}(\alpha))\mathrm{d}\alpha. \tag{3.14}$$

This is equivalent to the Radon Transform [Rado 17] which will be denoted $\mathcal{R}\{\cdot\}$ consecutively.

Equation (3.13) and its mono-energetic version Eq. (3.14) reveal a basic dilemma of standard single-energy CT imaging: The physical ground truth values of the scanned object are the spectral attenuation coefficients $\mu(E,\mathbf{r})$. The measurement process is correctly described by Eq. (3.13). However, the corresponding data $\mu(E,\mathbf{r})$ cannot be reconstructed from standard CT measurements. We would require spectrally resolved sinogram data $A(E)$ to fully reconstruct the spectral coordinate of $\mu(E,\mathbf{r})$. Even if these were available, quantum noise would lead to very limited representations of $\mu(E,\mathbf{r})$. Thus, Eq. (3.13) actually describes the experimental data correctly, but the corresponding ground truth variable $\mu(E,\mathbf{r})$ cannot be recovered due to missing information.

In single-energy CT this dilemma leads to a common approximation. The Radon transform and its inverse assume the linear X-ray physics of Eq. (3.14) to reconstruct $\bar{\mu}(\mathbf{r})$ images. The errors generated by this approximation are commonly referred to as beam hardening artifacts. The underlying model assumes that we can use Eq. (3.14) as an approximation for $\bar{\mu}(\mathbf{r})$. The X-ray quanta passing through the object are considered to have an effective energy. When quanta pass through thick or high

[1]The expression $\delta(E)$ resembles Dirac distribution.

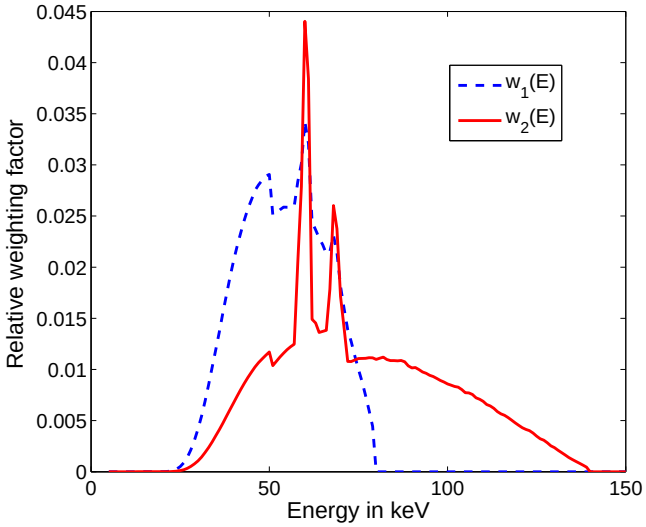

Figure 3.1: System Weighting Functions $w_1(E)$,$w_2(E)$ according to Eq. (3.1) for the 80 kV and 140 kV tube spectra in Fig. 1.5a and the detector responsivity $D(E)$ in Fig. 1.8. The two weighting functions reflect a common Dual Energy measurement case, often referred to as a Dual-kVp CT measurement.

atomic number object regions like bone, the effective energy of the detected quanta increases by several keV due to the characteristics of $\mu(E)$, see Fig. 1.15. The beam spectrum is hardened. As a consequence reconstructed $\bar{\mu}(\mathbf{r})$ are decreased with increasing beam hardening. The quantity $\bar{\mu}(\mathbf{r})$ is obtained applying a standard monoenergetic reconstruction (Sec. 1.6.2) to projection data from a polychromatic source without performing any beam hardening correction.

We can analytically derive the error of the approximation. The attenuation formula Eq. (3.13) can be written as

$$A = \exp\left(-\int_0^\infty \bar{\mu}(\mathbf{l}_{\theta,t}(\alpha))\mathrm{d}\alpha + R\right) \tag{3.15}$$

with

$$R = \frac{1}{2}\int_0^\infty w(E)\left(\int_0^\infty \mu(E,\mathbf{l}_{\theta,t}(\alpha))\mathrm{d}\alpha\right)^2 \mathrm{d}E + \ldots \tag{3.16}$$

The dots $(\ldots)$ indicate the higher orders of the Taylor series expansions used for this approximation.

The first term in R generally leads to an overestimation of A and a consequent underestimation of $\bar{\mu}(\mathbf{r})$ in the reconstructed image. We present a derivation of this approximation in the Appendix of [Heis 09].

Beam hardening corrections can alleviate most of these artifacts in practical single-energy CT. When we assume that R is small due to limited object attenuations or a beam hardening correction, we obtain an important result. The weighted attenuation

coefficient $\bar{\mu}(\mathbf{r})$ of a CT image and the underlying physical ground truth $\mu(E, \mathbf{r})$ are approximated by

$$\bar{\mu}(\mathbf{r}) \approx \int_0^\infty w(E)\mu(E, \mathbf{r})\mathrm{d}E \tag{3.17}$$

for small, low attenuation objects.

Note that this is a local relationship at each point $\mathbf{r}$ in the CT data set. It allows us to link measured and reconstructed CT data to the ground truth object variable $\mu(E, \mathbf{r})$. Equation (3.17) underlines an important fact of single-energy CT imaging. The reconstructed CT attenuations $\bar{\mu}(\mathbf{r})$ depend on the SWF $w(E)$. When we change the X-ray source spectrum characteristics $S(E)$ or use a different detector responsivity $D(E)$, the reconstructed attenuation values change. Contrasts of the image are altered. In practice, for water-like materials only minor deviations are expected in the HU numbers due to the water normalization, however, quantitative measures of attenuation values and contrast of non-waterlike structures may not be identical between CT systems.

Local Weighting Function

Following Eq. (3.13) we have the physical projection formula

$$\mathcal{P}\left\{\mu(E, \mathbf{r})\right\} = -\ln\left(\int_0^\infty w(E)\exp\left(-M_{\theta,t}(E)\right)\mathrm{d}E\right) \tag{3.18}$$

with the measurement operator $\mathcal{P}\left\{\cdot\right\}$ and

$$M_{\theta,t}(E) = \int_0^\infty \mu(E, \mathbf{l}_{\theta,t}(\alpha))\mathrm{d}\alpha \tag{3.19}$$

as an abbreviation for the spatial path integration. The reconstructed effective attenuation coefficient is

$$\bar{\mu}(\mathbf{r}) = \mathcal{R}^{-1}\left\{\mathcal{P}\left\{\mu(E, \mathbf{r})\right\}\right\} \tag{3.20}$$

with $\mathcal{R}^{-1}\left\{\cdot\right\}$ as the inverse Radon transform operator.

Subsequently we derive an iterative scheme to solve Eq. (3.20). Unlike typical minimization schemes derived from

$$\hat{\mu}(E, \mathbf{r}) = \arg\min_{\mu(E,\mathbf{r})}\left\{\left|\bar{\mu}(\mathbf{r}) - \mathcal{R}^{-1}\left\{\mathcal{P}\left\{\mu(E, \mathbf{r})\right\}\right\}\right|\right\}, \tag{3.21}$$

it has the same mathematical form as Eq. (3.17). This allows the direct application of the method to image-based spectral CT methods like the image-based basis material decomposition, featuring a high computational efficiency and fast convergence: Only one forward and one backward projection per iteration and input image is required and one to two iterations lead to a sufficient accuracy for all evaluated practical applications. We insert a factor $1 = \int_0^\infty w(E)\mathrm{d}E$ into Eq. (3.20),

$$\bar{\mu}(\mathbf{r}) = \int_0^\infty w(E)\mathrm{d}E \cdot \mathcal{R}^{-1}\left\{\mathcal{P}\left\{\mu(E, \mathbf{r})\right\}\right\}, \tag{3.22}$$

and use that the projected sinogram data $\mathcal{P}\{\mu(E,\mathbf{r})\}$ is independent of E. This yields

$$\bar{\mu}(\mathbf{r}) = \int_0^\infty w(E)\mathcal{R}^{-1}\{\mathcal{P}\{\mu(E,\mathbf{r})\}\}\,\mathrm{d}E. \tag{3.23}$$

Expanding with $\frac{\mu(E,\mathbf{r})}{\mu(E,\mathbf{r})}$ yields

$$\bar{\mu}(\mathbf{r}) = \int_0^\infty w(E)\frac{\mathcal{R}^{-1}\{\mathcal{P}\{\mu(E,\mathbf{r})\}\}}{\mu(E,\mathbf{r})}\mu(E,\mathbf{r})\mathrm{d}E. \tag{3.24}$$

This can be written as

$$\bar{\mu}(\mathbf{r}) = \int_0^\infty \Omega(E,\mathbf{r})\mu(E,\mathbf{r})\mathrm{d}E, \tag{3.25}$$

which yields the following definition of the LWF:

$$\Omega(E,\mathbf{r}) = w(E)\frac{\mathcal{R}^{-1}\{\mathcal{P}\{\mu(E,\mathbf{r})\}\}}{\mu(E,\mathbf{r})}. \tag{3.26}$$

Equation (3.25) connects the spectral attenuation coefficient to the measured weighted attenuation coefficient. It yields an image-based quantitative description of the CT measurement and reconstruction process.

The LWF $\Omega(E,\mathbf{r})$ given by Eq. (3.26) describes the effective spectral weighting at an arbitrary object position. It depends on the scanned object $\mu(E,\mathbf{r})$, the image reconstruction process given by $\mathcal{R}^{-1}\{\cdot\}$ and the measurement process described by $\mathcal{P}\{\cdot\}$. The weighting function $w(E)$ is given by the SWF of Eq. (3.1).

In the derivation of Eq. (3.26) the weighting function $w(E)$ was an arbitrary function normalized to one. However, for a small object we have $\mathcal{R}^{-1}\{\mathcal{P}\{\mu(E,\mathbf{r})\}\} \approx \mu(E,\mathbf{r})$ and thus $\Omega(E,\mathbf{r}) \approx w(E)$. This means that Eq. (3.25) turns into the small object approximation given by Eq. (3.17) and $w(E)$ is indeed given by the CT tube and detector characteristics.

Calculation of the LWF

In practical CT we measure weighted attenuation coefficients $\bar{\mu}(\mathbf{r})$. In order to calculate the LWF, we need an estimate of $\mu(E,\mathbf{r})$ based on the input data. There are various ways to produce estimates of $\mu(E,\mathbf{r})$. In this section we assume that we have performed a Dual Energy scan. This yields two sets of attenuation value data $\bar{\mu}_1(\mathbf{r})$ and $\bar{\mu}_2(\mathbf{r})$. We employ the BMD in an image-based form [Tagu 07] to obtain a parametrization of $\mu(E,\mathbf{r})$ into two basis material coefficients $c_1(\mathbf{r})$ and $c_2(\mathbf{r})$. Unlike the BMD-definition in Sec. 3.2.2, we can directly use the reconstructed values without beam hardening correction together with the LWF by incorporating Eq. (3.2) into Eq. (3.25) and exchanging the order of summation and integration:

$$\begin{pmatrix} \bar{\mu}_1(\mathbf{r}) \\ \bar{\mu}_2(\mathbf{r}) \end{pmatrix} = \mathbf{K}\begin{pmatrix} c_1(\mathbf{r}) \\ c_2(\mathbf{r}) \end{pmatrix}. \tag{3.27}$$

The elements of the matrix $\mathbf{K}$, k_{ij}, are given by

$$k_{ij} = \int_0^\infty \Omega_i(E) f_j(E)\,\mathrm{d}E. \tag{3.28}$$

Equation (3.27) is solved for the coefficients $c_i(\mathbf{r})$ by inverting $\mathbf{K}$. However, the circular dependency of solving Eqs. (3.25) resp. (3.26) and (3.27) resp. (3.28) has to be resolved. This leads to a two-phase iterative procedure according to the flowchart shown in Fig. 3.2. Initially, we set $\Omega_j^{(k=0)}(E,\mathbf{r}) = w(E)$. With each iteration step, the algorithm updates the estimates of $\mu_j^{(k)}(E,\mathbf{r})$ and $\Omega_j^{(k)}(E,\mathbf{r})$.

This iteration procedure defines the LSR. It yields an estimate of both the LWF and $\mu(E,\mathbf{r})$. We can adapt the LSR procedure to multi-channel spectral CT and Basis Material Decomposition, i.e. a number of $N > 2$ spectral channels and a number of $M \leq N$ basis materials. Note that for medical CT it is questionable to work with more than two basis materials. This is due to the fact that the K-edges of the atoms found in biological tissues lie below the lower threshold energy of around 30 keV in CT imaging.

An algorithmic description of an efficient LSR implementation for Dual Energy CT is given in Algorithm 1.

Input: CT attenuation datasets $\bar{\mu}_0(\mathbf{r})$ and $\bar{\mu}_1(\mathbf{r})$ with corresponding system weighting functions $w_0(E)$ and $w_1(E)$, number of iterations I
Output: Local spectral weighting function estimates $\Omega_0^{(I)}(E,\mathbf{r})$ and $\Omega_1^{(I)}(E,\mathbf{r})$ and spectral attenuation coefficients $\mu^{(I)}(E,\mathbf{r})$

$\Omega_0^{(0)}(E,\mathbf{r}) = w_0(E)$
$\Omega_1^{(0)}(E,\mathbf{r}) = w_1(E)$
for $i = 1$ **to** I **do**
  Basis material decomposition:
  $(\rho_\mathrm{W}(\mathbf{r}), \rho_\mathrm{B}(\mathbf{r})) = \mathrm{BMD}\left(\Omega_0^{i-1}(E,\mathbf{r}), \Omega_1^{i-1}(E,\mathbf{r}), \bar{\mu}_0(\mathbf{r}), \bar{\mu}_1(\mathbf{r})\right)$
  $\mu^{(i)}(E,\mathbf{r}) = \rho_\mathrm{W}(\mathbf{r}) \cdot \mu_W(E) + \rho_\mathrm{B}(\mathbf{r}) \cdot \mu_B(E)$
  Forward projection FP *of basis material coefficients:*
  $R_W(\theta,t) = \mathrm{FP}\left(\rho_W(\mathbf{r})\right)$
  $R_B(\theta,t) = \mathrm{FP}\left(\rho_B(\mathbf{r})\right)$
  $M_{\theta,t}(E) = R_\mathrm{W}(\theta,t) \cdot \mu_W(E) + R_\mathrm{B}(\theta,t) \cdot \mu_B(E)$
  LWF calculation according to Eq. (3.26):
  $\Omega_0^{(i)}(E,\mathbf{r}) = \mathrm{LWF}\left(\mu^{(i)}(E,\mathbf{r}), M_{\theta,t}(E), w_0(E)\right)$
  $\Omega_1^{(i)}(E,\mathbf{r}) = \mathrm{LWF}\left(\mu^{(i)}(E,\mathbf{r}), M_{\theta,t}(E), w_1(E)\right)$
end
return $\Omega_0^{(i)}(E,\mathbf{r}), \Omega_1^{(i)}(E,\mathbf{r}), \mu^{(i)}(E,\mathbf{r})$

Algorithm 1: Local Spectral Reconstruction algorithm. The function BMD() solves Eq. 3.27 and yields the basis material coefficients, FP() is a forward projection of basis material coefficients and the function LWF() calculates the LWF according to Eq. (3.26).

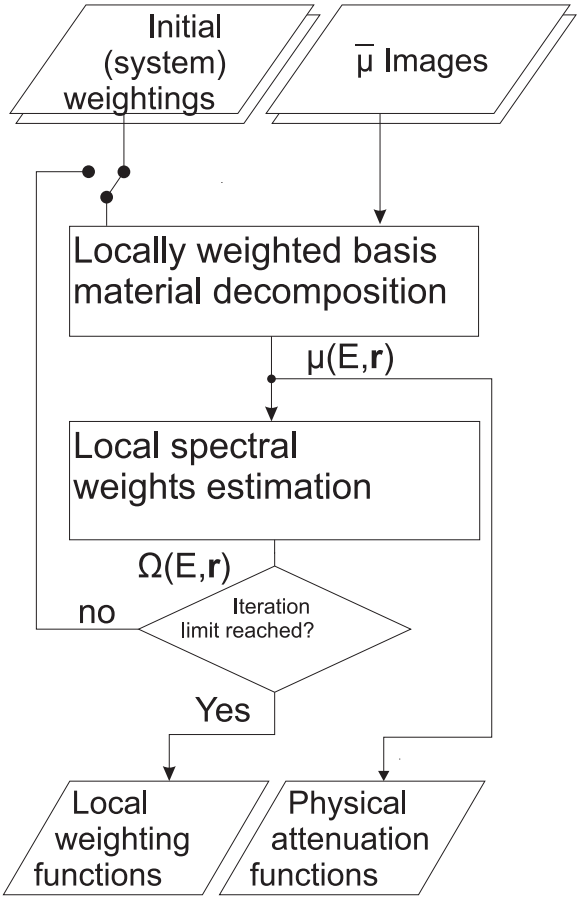

Figure 3.2: The LSR procedure is a two-phase update process, starting with the SWF as an initial estimation of the LWF, updating $\mu^{(1)}(E, \mathbf{r})$, updating $\Omega_j^{(1)}(E, \mathbf{r})$, updating $\mu^{(2)}(E, \mathbf{r})$, etc. After S steps we obtain an estimate for both the LWF and the object attenuation coefficient. Image taken from [Heis 09].

Applications

The LSR framework (Eqs. (3.25), (3.26)) yields an estimate of the LWF and the object ground truth $\mu(E, \mathbf{r})$. For practical quantitative spectral CT applications, three main fields exist:

The first group of applications targets the obtained $\mu(E, \mathbf{r})$ object data. The resulting parameters like basis material coefficients can be displayed and analyzed for specific diagnostic tasks. In comparison to existing image-based calculations, the effects of beam-hardening and system energy weighting properties are incorporated quantitatively into the algorithm. We investigate the quantitative accuracy and precision in the experimental section.

It is important to note that the $\mu(E, \mathbf{r})$ are theoretically independent of object self-attenuation effects and characteristics of the reconstruction and measurement process. For example, the difference in reconstruction kernels between the two Dual-kVp measurements can be incorporated into the measurement model of Eq. (3.20). This can improve pixel registration between the input data sets. Note that the

spatial resolution of the $\mu(E, \mathbf{r})$-estimate, however, is limited by the input image discretization.

In practice, accurate descriptions of $w(E)$ and the measurement operator $\mathcal{P}\{\cdot\}$ are required to ensure quantitative results. Note that the inverse Radon transform operator $\mathcal{R}^{-1}\{\cdot\}$ enters both the input image reconstruction and the LWF calculation in the same way. Hence it has no additional effect on the accuracy and precision of $\mu(E, \mathbf{r})$.

Scatter radiation can be included in the measurement model, Eq. (3.18), or corrected by an appropriate scatter correction algorithm. For the Dual-kVp experiments carried out in this work, scattered radiation plays only a minor role and is not corrected for.

It should be noted that alternative $\mu(E, \mathbf{r})$ parameterizations can be employed in the LSR framework. An example is the image-based Rho-Z projection method [Heis 03]. Here the attenuation coefficient is modeled as

$$\mu(E, \mathbf{r}) = \rho_{\text{eff}}(\mathbf{r}) \left(\frac{\mu}{\rho}\right)(E, Z_{\text{eff}}(\mathbf{r}))\,. \tag{3.29}$$

In this case we obtain effective density and atomic number representations $(\rho_{\text{eff}}, Z_{\text{eff}})$ as a result of the LSR framework.

A second class of applications is energy calibration. Here new images are calculated which, for instance, contain the contrasts of an alternative tube voltage setting. Mathematically, this corresponds to a pre-defined, constant energy weighting $w_c(E)$ throughout the whole CT image data. A number of different target weightings exist: CT beam hardening corrections, for example, typically aim at a constant System Weighting Function throughout the image, see e.g. Fig. 3.1 for the $w(E)$ of CT measurements with 80 kV and 140 kV tube voltage settings.

This can be extended to mono-energetic calibrations with the target weighting function given by $w_c(E) = \delta(E - E_0)$. An application of mono-energetic attenuation coefficients is contrast enhancement for specific tissue differences.

A further energy calibration application is the attenuation correction in SPECT/CT and PET/CT. Mono-energetic attenuation coefficients at e.g. 141 keV and 511 keV for the respective tracer emission lines of $^{99\text{m}}$Tc and ^{18}F-glucose are required.

We can express all of the above energy calibration applications in a common formula:

$$\bar{\mu}_c(\mathbf{r}) = \int_0^\infty w_c(E)\mu(E, \mathbf{r})\,\mathrm{d}E. \tag{3.30}$$

Here $\bar{\mu}_c(\mathbf{r})$ denotes the corrected image data for the LSR-determined $\mu(E, \mathbf{r})$ and a chosen target energy weighting $w_c(E)$.

The third field of applications employs the LWF result. Fundamentally, the LWF offers a deeper understanding of the energy weighting process in CT. In practice it enables a direct identification of an arbitrary object material. Based on the LWF and Eq. (3.25), the measured spectral data $\bar{\mu}_i(\mathbf{r})$ can be compared against reference spectral attenuation functions. This is demonstrated by a proof of concept in Section 3.3.4.

3.3.3 Materials and Methods

In order to verify the LSR framework we have applied it to a number of measured and simulated CT phantom set-ups. In this section we describe the measurement and simulation procedures, the evaluated phantom set-ups and the implementation of the LSR algorithm.

Measurements and Simulations

For the measurements a Siemens Definition AS+ CT scanner (Siemens Healthcare, Forchheim, Germany) was employed. Two consecutive sequential scans at tube voltages of 80 kV and 140 kV were performed for each phantom. The tube current was set to 550 mAs for the 80 kV measurement and 600 mAs for the 140 kV measurement. The rotation time was set to 0.5 s and 1152 readings were acquired during one rotation. We used a standard filtered back-projection (FBP) algorithm with rebinning to parallel beam geometry for reconstruction. For all scans a soft body kernel was used for reconstructing 32 slices of 1.2 mm thickness.

In order to apply the LSR framework to practical CT measurements, the wedge filter at the exit window of the X-ray tube has to be considered. Figure 1.2b shows an example for this type of tube-filter. The material thickness is minimal at the center and increases to the full aluminum thickness towards the edges. A detailed description can be found in Sec. 1.3. This geometry increasingly reduces the primary X-ray intensity – and thus patient dose – towards the borders of the fan beam. As a secondary effect, it changes the spectral composition of the primary X-ray spectrum [Mail 09]. Due to this the effective System Weighting Function has the form

$$w_j(E) = \frac{S(E)D(E)e^{-l_j\mu_F(E)}}{\int_0^\infty S(E')D(E')e^{-l_j\mu_F(E')}\mathrm{d}E'} \tag{3.31}$$

for the j-th sinogram channel, with $\mu_F(E)$ as the attenuation function of the bow-tie filter material (e.g. aluminum) and l_j as its local thickness. It replaces $w(E)$ in Eqs. (3.18) to (3.26).

As a second source of CT data, we have used simulated CT images $\bar{\mu}(\mathbf{r})$. An analytic forward projector software implements Eq. (3.13) to calculate the sinogram from the object phantom data $\mu(E, \mathbf{r})$. The simulated CT scanner X-ray geometry as well as tube and detector properties correspond to those of the CT scanner used in the measurements. The required X-ray tube spectra and detector responsivity functions for 80 kV and 140 kV tube voltages are shown in Fig. 3.1. Detector cross-talk and electronic noise effects were neglected as they contribute only minor errors in our applications. A standard filtered back projection algorithm for indirect fan-beam data with a cosine filter kernel (Fig. 1.20) was used for reconstruction. A detailed description can be found in Sec. 1.6.2. The simulation results were limited to a central single slice.

Phantom Set-Ups

A total number of five measurement and simulation set-ups are used to generate input image data for a verification of LSR applications. Table 3.1 summarizes the chosen configurations A to E.

Configurations A and C are measurement cases. A body abdomen phantom (A) and a water-filled cylinder with 25 cm diameter (C) were scanned. Configurations B, D and E employ simulated data. The phantoms comprise a water cylinder of 40 cm diameter (B) and an anthropomorphic thorax phantom consisting of several different body tissue classes (D and E). Fig. 3.3 shows the phantom set-up E. The tissue classes are defined in Table 3.2. The material compositions are chosen according to Table A1 of the ICRU46 Report [ICRU 92]. Tissue classes XV to XVII correspond to three blood classes with slightly different concentrations of the contrast agent iodine. They are positioned in the heart chambers and the aorta. All three contain $1.06\frac{\mathrm{g}}{\mathrm{cm}^3}$ of blood. Tissue XV additionally contains $5.42 \cdot 10^{-3}\frac{\mathrm{g}}{\mathrm{cm}^3}$ of iodine, tissue XVI $4.76 \cdot 10^{-3}\frac{\mathrm{g}}{\mathrm{cm}^3}$ and tissue XVII $3.40 \cdot 10^{-3}\frac{\mathrm{g}}{\mathrm{cm}^3}$. For configuration D all three blood classes containing iodine are substituted by the standard blood parametrization XIV.

LSR Implementation

The LSR implementation is based on the image-based Basis Material Decomposition given by Eq. (3.27). Basis material function pairs of water / femur bone and blood / iodine are used. The choice between the two sets in Tab. 3.1 aims at a minimization of systematic model errors. Blood / iodine is used as soon as iodine contrast agent material is present, c.f. [Alva 76, Hawk 86]. We evaluated the model mismatch of these basis material pairs on various body material compositions. The results presented in Tab. 3.2 show a good performance of the water / femur bone set on all evaluated body materials. In the presence of iodine, however, this parameterization fails to deliver the required accuracy. The blood / iodine set yields better accuracy in these cases but is not suited to model bone tissue types accurately. Both sets are sufficiently accurate in representing soft tissue types.

As the result of the LSR process for set-ups A to E, we obtain an LWF $\Omega(E, \mathbf{r})$ and the object representation $\mu(E, \mathbf{r})$ after each iteration.

Ground Truth Comparisons

In order to verify the quantitative accuracy and precision of the LSR framework, we compare application results to ground truth values at various points throughout this work. For a predefined object the ground truth attenuation coefficient $\mu_{\mathrm{GT}}(E, \mathbf{r})$ is known. It can be expressed by Eqs. (1.1) and (1.3). We can directly compare the ground-truth $\mu_{\mathrm{GT}}(E, \mathbf{r})$ to the LSR result $\mu(E, \mathbf{r})$. For energy calibration to a defined weighting function $w_c(E)$ according to Eq. (3.30), we define the relative scalar comparison result

Id.	Description	Data Source	Basis material set
A	Upper abdomen phantom	measured	water-bone
B	40 cm water cylinder	simulated	water-bone
C	25 cm water cylinder	measured	water-bone
D	Thorax phantom w/o iodine	simulated	water-bone
E	Thorax phantom with iodine	simulated	blood-iodine

Table 3.1: Measurement and simulation set-ups A to E used for the LSR validation. For each set-up, the phantom, data generation method and chosen basis material functions are listed.

$$D_{\bar{\mu}} = \frac{|\bar{\mu}(\mathbf{r}) - \bar{\mu}_{\mathrm{GT}}(\mathbf{r})|}{\bar{\mu}_{\mathrm{GT}}} = \tag{3.32}$$

$$= \frac{\left|\int_0^\infty w_c(E)\,(\mu(E,\mathbf{r}) - \mu_{\mathrm{GT}}(E,\mathbf{r}))\,\mathrm{d}E\right|}{\int_0^\infty w_c(E)\mu_{\mathrm{GT}}(E,\mathbf{r})\,\mathrm{d}E}. \tag{3.33}$$

The smaller $D_{\bar{\mu}}$, the more accurately the corresponding energy calibration task was performed. In the following section we use the ground truth comparisons to examine the qualitative and quantitative characteristics of the results for a number of spectral CT applications.

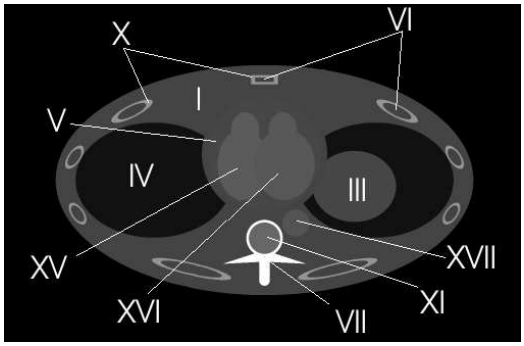

Figure 3.3: Thorax phantom set-up used as set-up D and E in Tab. 3.1. The roman number annotations indicate specific body materials listed in Tab. 3.2. The spectral attenuation coefficient $\mu(E,\mathbf{r})$ is provided for each material type according to the body compositions in the ICRU46 report. At regions XV to XVII, set-up E contains blood with varying iodine contrast agent concentrations, whereas set-up D substitutes the three regions by the standard blood parametrization XIV.

3.3.4 Results and Discussion

We used the measurement and simulation set-ups A to E listed in Tab. 3.1 to evaluate the following properties:

First, we assess the basic characteristics of the LWF for an upper abdomen phantom containing a bone inset and a homogeneous water phantom. Secondly, we evaluate the accuracy and precision of an LSR-based energy calibration procedure. Both

		water / bone		
No.	**Tissue name**	**60 kV**	**100 kV**	**120 kV**
I	Average soft tissue (male)	6.53e-3	8.19e-4	4.06e-4
II	Kidney	2.84e-3	5.27e-4	2.74e-4
III	Liver (healthy)	2.16e-3	4.28e-4	2.17e-4
IV	Lung (healthy, inflated)	1.31e-3	3.92e-4	2.15e-4
V	Skeletal muscle	3.19e-3	5.93e-4	3.10e-4
VI	Red marrow	1.70e-2	2.14e-3	1.20e-3
VII	Bone cortical	6.97e-3	1.00e-3	5.58e-4
VIII	Bone cranium	4.97e-3	6.74e-4	3.78e-4
IX	Bone femur (30 years, male)	4.76e-6	1.99e-6	3.82e-6
X	Bone rib 2 to 6	3.12e-3	4.02e-4	2.53e-4
XI	Bone spongiosa	6.20e-3	8.99e-4	5.42e-4
XII	Bone humerus	2.31e-3	3.32e-4	1.76e-4
XIII	Cartilage	8.85e-3	1.18e-3	7.33e-4
XIV	Blood	5.92e-3	1.07e-3	6.47e-4
XV	Blood (high contrast)	1.54	2.14e-1	1.44e-1
XVI	Blood (medium contrast)	1.40	1.93e-1	1.29e-1
XVII	Blood (low contrast)	1.07	1.45e-1	9.65e-2
		blood / iodine		
No.	**Tissue name**	**60 kV**	**100 kV**	**120 kV**
I	Average soft tissue (male)	2.49e-1	3.09e-2	2.01e-2
II	Kidney	6.89e-2	8.58e-3	5.60e-3
III	Liver (healthy)	4.95e-2	6.11e-3	3.99e-3
IV	Lung (healthy, inflated)	2.74e-2	3.39e-3	2.24e-3
V	Skeletal muscle	6.46e-2	8.06e-3	5.26e-3
VI	Red marrow	4.15e-1	5.12e-2	3.32e-2
VII	Bone cortical	4.04	6.95e-1	4.91e-1
VIII	Bone cranium	3.58	5.93e-1	4.14e-1
IX	Bone femur (30 years, male)	2.92	4.59e-1	3.16e-1
X	Bone rib 2 to 6	3.08	4.89e-1	3.38e-1
XI	Bone spongiosa	1.98	2.90e-1	1.96e-1
XII	Bone humerus	3.27	5.27e-1	3.65e-1
XIII	Cartilage	3.07e-1	4.02e-2	2.63e-2
XIV	Blood	9.12e-7	2.12e-7	2.90e-8
XV	Blood (high contrast)	2.67e-7	6.00e-7	8.53e-7
XVI	Blood (medium contrast)	6.64e-6	6.92e-7	1.02e-6
XVII	Blood (low contrast)	5.79e-6	4.00e-7	2.14e-6

Table 3.2: List of body materials used in the thorax phantom set-ups D and E, with the former shown in Fig. 3.3. Roman numbers provide an index to each material. Columns 3 to 7 contain the relative systematic deviation of the material ground truth to the basis material representation, see Eq. (3.33). The values represent relative deviations, not percent-values. The upper half of the table includes relative deviations for the water / bone $\mu(E, \mathbf{r})$ representation and the lower half includes the deviations for blood / iodine representations. The respective target energy weighting is given by a tungsten spectrum with the tube voltage stated in the column title. Cases where the relative deviation exceeds 1 % are highlighted.

beam hardening corrections to different X-ray tube target weightings and an attenuation correction for SPECT/CT are evaluated. Moreover, the accuracy of an iodine contrast agent density estimation is evaluated. Finally, a direct material identification based on the LWF is demonstrated.

Characteristics of the Local Weighting Function

In order to show the basic characteristics of the LWF, it is evaluated for the measured upper abdomen phantom data (set-up A). Figure 3.4 shows the 80 kV input image with markers at different locations within the thorax phantom slice. Figure 3.5 shows the corresponding LWFs. Several effects are visible. The central red and black soft tissue points have a very similar LWF. In comparison to this the blue point close to the phantom border exhibits a reduced LWF. The shape change within the same tissue class is mainly due to the bow-tie filter. In this case the LWF values are decreased towards the phantom boundaries as the beam hardening of the bow-tie filter is stronger than the object induced beam hardening. Finally, the violet point at the spinal bone inset shows a strong reduction of the LWF for lower energies.

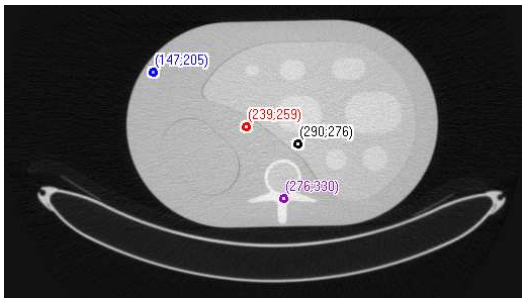

Figure 3.4: CT image of the upper abdomen phantom and location of the sample points for the LWF plots of Fig. 3.5.

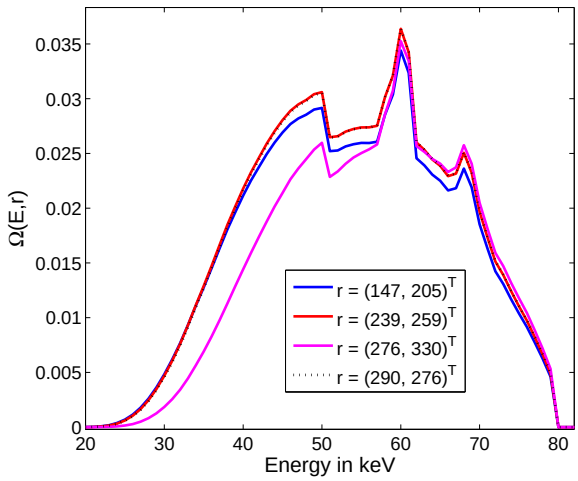

Figure 3.5: Samples of the local spectral weighting function within the thorax phantom.

We can further understand this behavior with set-up B. It comprises a simulation of a 40 cm water phantom. The X-ray tube bow-tie filter is omitted to obtain the pure object effect. Table 3.3 shows the resulting change of the LWF integral value for varying distances from the center of the water cylinder slice. The integral of the LWF at the center is reduced by around 5% compared to the edge of the phantom. Unlike the SWF, the LWF is generally not normalized to one. The integral value over energy decreases with increasing beam hardening. This property reflects the under-estimation of the attenuation values due to beam hardening in the uncorrected input image.

These basic results indicate that the shape of the LWF is originally given by the SWF. Local changes in the shape are governed by the attenuation function of the underlying material. Furthermore, beam hardening mainly affects the integral value of the LWF. This corresponds to the mathematical structure of the LWF definition in Eq. (3.26).

Distance from cylinder center (cm)	**Integral value of the LWF**
80 kV system weighting	1.0000
0	0.9533
4	0.9549
8	0.9551
12	0.9656
16	0.9707
20	1.0047

Table 3.3: Integral values of the SWF and LWFs at different locations within the 40 cm water cylinder slice.

Energy calibration

As the first energy calibration experiment, the 80 kV and 140 kV measurement data of the 25 cm water phantom set-up C is provided to the LSR algorithm. With the resulting $\mu(E, \mathbf{r})$ representations an energy calibration according to Eq. (3.30) is performed. The target weightings $w_c(E)$ are chosen as the SWFs for the 80 kV and 140 kV measurement.

The 140 kV beam hardening correction result is shown in Fig. 3.6 after the first iteration step. A nearly homogeneous water value is obtained in the line plot. We can compare the water values $\bar{\mu}(\mathbf{r})$ against the water attenuation function of Eq. (1.2) weighted by the respective target SWFs. The average ground truth deviations are $D_{\bar{\mu}} = 2.86\,\%$ for the shown 140 kV case and $D_{\bar{\mu}} = 2.05\,\%$ for the 80 kV case. Additional iterations do not lead to further improvements of the accuracy. The remaining ground truth deviations are probably due to inaccuracies in the system descriptions, especially the parameterizations of the SWF and the bow-tie filter. The next section investigates the potential algorithmic inaccuracies.

In order to evaluate the algorithmic accuracy and precision, we use the simulated thorax-phantom set-up D. For the simulated data, the measurement system description is known and accurate by definition. Any remaining ground truth deviations can

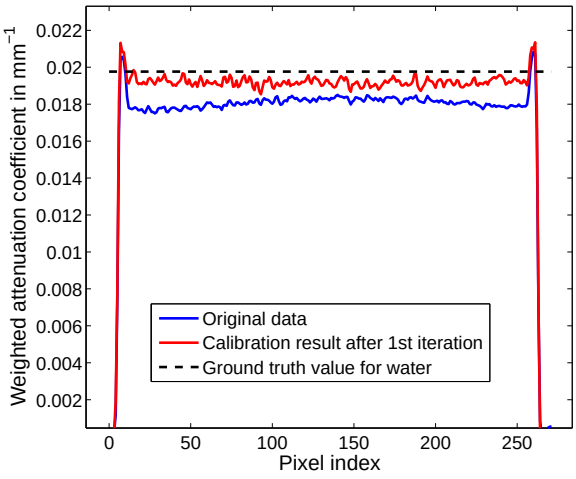

Figure 3.6: Beam hardening correction result after first iteration compared to original and ground truth attenuation values. The higher values at the border of the phantom are caused by the plastic casing of the water phantom.

be attributed to LSR inaccuracies. The simulated image data include Poisson quantum noise. It is determined by maximum input quantum numbers of $N_0^{(1)} = 6.38\text{e}5$ (80 kV) and $N_0^{(2)} = 2.83\text{e}6$ (140 kV) per detector pixel reading. This enables us to evaluate the precision of the LSR iteration results. For the target weighting $w_c(E)$, the detector responsivity is kept constant and spectra for the tungsten tube voltages 60 kV, 80 kV, 100 kV, 120 kV and 140 kV are used. We also evaluate mono-energetic spectra at 141 keV and 511 keV. This corresponds to the emission energy of $^{99\text{m}}$Tc and ^{18}F as the most common SPECT and PET tracers. The resulting attenuation values can be used to perform an attenuation correction in PET/CT and SPECT/CT.

Accuracy, Precision and Convergence

Figure 3.7 shows the absolute error for average soft tissue attenuation values after energy calibration with a 80 kV target weighting. The error is given by the absolute difference to the ground truth attenuation function which has been weighted with the same target weightings. The first four LSR iterations are shown. The mean deviation for each step is shown as the straight blue line. It describes the systematic deviation from the ground truth and thus the accuracy of the obtained soft tissue values. The error bars represent the standard deviation of all soft tissue voxels and the dashed lines indicate the 25% and 75% quantiles. These values represent the precision of the obtained values.

The mean error drops strongly in the first LSR iteration cycle. Here the image inhomogeneities caused by beam hardening are already reduced substantially. After the second iteration step the average deviation is completely eliminated. Further iteration steps do not contribute increasing accuracy. At the same time the standard deviation indicated by the error bars rises. This is due to the image noise which is introduced by the basis material representations and amplified with each step. A trade-off between accuracy and precision has to be defined. For this particular result

one to two iterations are a reasonable choice to obtain a very good accuracy without a major sacrifice in precision. From the results we can also deduce that the convergence rate shows an approximately exponential behavior.

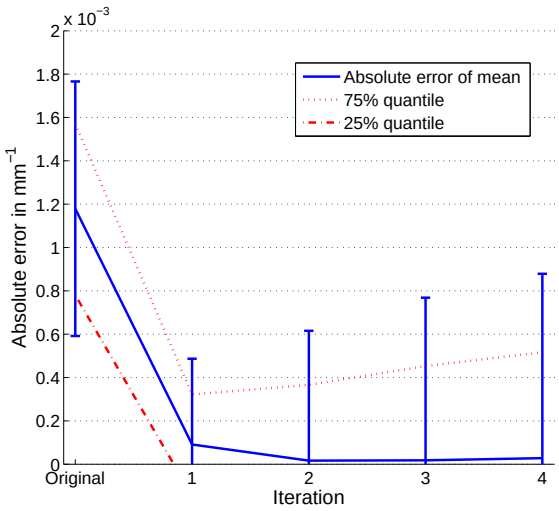

Figure 3.7: Absolute error for average soft tissue attenuation values after energy calibration with 80 kV target weighting.

Accuracy and Convergence for Multiple Target Weightings and Tissue Classes

We can extend the findings of the last sections to all twelve material classes present in phantom set-up D. Since we focus on the accuracy and convergence behavior, Poisson noise is not added to the input data in this case. Figure 3.8 shows the relative errors $D_{\bar{\mu}}$ of the mean attenuation values for all available tissue classes in the uncorrected image and the first four iterations. Again, a 80 kV target weighting has been used.

All materials show a convergence behavior similar to the soft tissue depicted in Fig. 3.7. Note that the bone materials require the strongest value shifts as they are affected the most by beam hardening impacts.

Figure 3.9 demonstrates convergence and accuracy of an energy calibration to a mono-energetic 511 keV spectrum. This is equivalent to the calculation of an attenuation correction map for PET/CT. Again, the LSR process converges exponentially. There is almost no change in the values after two iterations and the errors are in the same range as in the 80 kV beam hardening correction case. Similar results are obtained for a mono-energetic 141 keV target spectrum (Fig. 3.10). The results indicate that the calculation of both PET/CT and SPECT/CT attenuation maps is feasible with appropriate accuracy. This means that LSR can be used for an exact quantitative attenuation correction instead of merely approximative approaches commonly used with single energy CT data.

Figure 3.10 also summarizes the remaining energy calibration cases. Relative errors for energy calibrations to all evaluated target weightings for all available tissue classes are shown. Only the results for the fourth iteration are displayed. In general, the error is smaller for soft tissues. All tissues tend to have smaller errors for

higher polychromatic target energies whereas the error of the monochromatic 141 keV spectrum is larger for some tissues. The range of relative errors is very small for all tissues and mostly below 0.1% deviation from the ground truth tissue attenuation value. The comparably high error in the inflated lung tissue is caused by the very low attenuation values and the resulting high relative error even for minor absolute deviations.

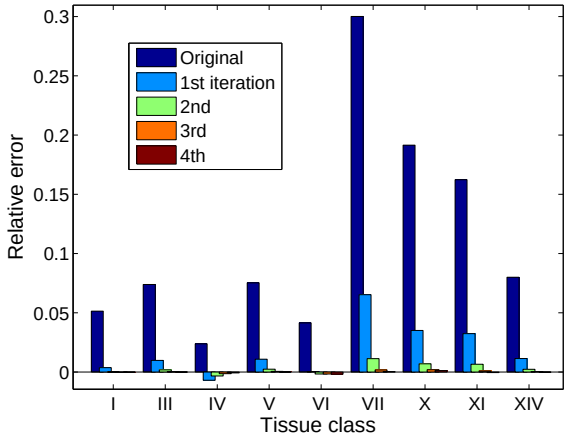

Figure 3.8: Relative error for energy calibration with 80 kV base and target weighting (negative values indicate over-estimation). The tissue classes are described in Tab. 3.2 and illustrated in Fig. 3.3.

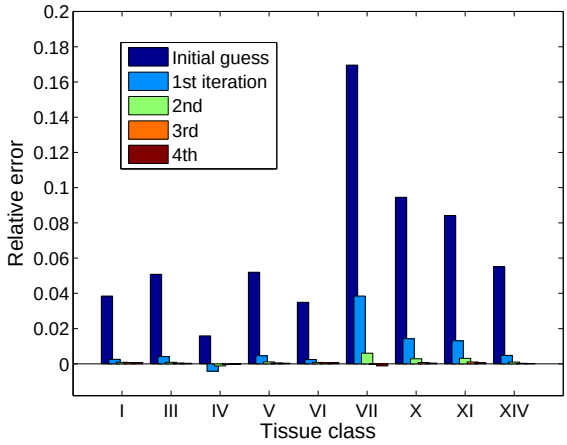

Figure 3.9: Relative error for energy calibration from 140 kV base to mono-energetic 511 keV target weighting (negative values indicate over-estimation).

Iodine Density Estimation

We evaluate the accuracy of the basis material coefficients for the iodine filled blood insets in set-up E of Tab. 3.1. The coefficients should represent the true densities of blood and iodine, since the basis materials exactly correspond to the mixture

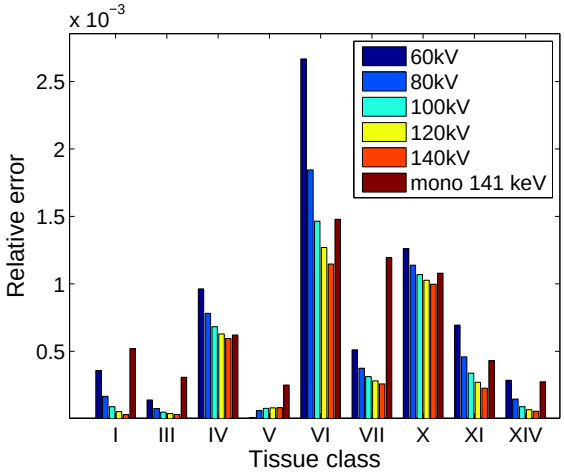

Figure 3.10: Relative errors for energy calibration of 80 kV input data to target spectra from 60 kV to 140 kV and a mono-energetic 141 keV spectrum.

materials of the tissue classes. Figures 3.11a and 3.11b show the resulting absolute deviations.

The estimated blood densities range from 1.0601 to 1.0604 with decreasing iodine concentration which equals a relative error of less than 0.05 %. The iodine concentration values for the three tissue classes are $5.40 \cdot 10^{-3} \frac{\mathrm{g}}{\mathrm{cm}^3}$ (relative error 0.33 %) for high concentration, $4.75 \cdot 10^{-3} \frac{\mathrm{g}}{\mathrm{cm}^3}$ (relative error 0.19 %) for medium concentration and $3.42 \cdot 10^{-3} \frac{\mathrm{g}}{\mathrm{cm}^3}$ (relative error 0.005 %) for low concentration.

Interestingly, the model mismatch of the iodine / blood basis functions to the bone constituents of the phantom (s. Tab. 3.2) does not influence the quantitative accuracy of the obtained densities. This can be attributed to the fact that the bone forward projection errors do not contribute substantially to the error in the evaluated quantities. In bone-dominated regions like shoulder or head slice images, this can potentially lead to more pronounced deviations. A more accurate modeling of the $\mu(E, \mathbf{r})$ could be required then, for instance with a spatially varying basis set.

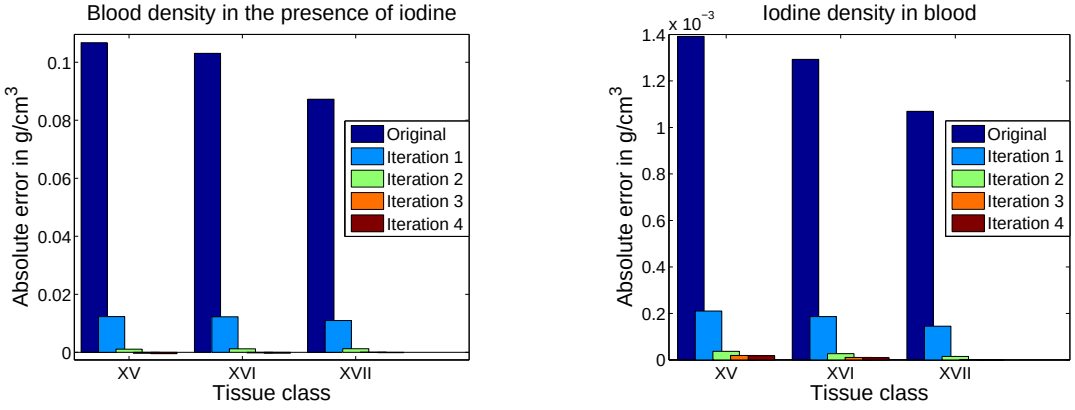

(a) Blood density estimates

(b) Iodine density estimates

Figure 3.11: Absolute error for blood and iodine densities in blood-iodine mixtures estimated with LSR.

Tissue	H	C	N	O	Others	Density (g/cm^{-3})
Average soft tissue	10.5	25.6	2.7	60.2	0.1 Na, 0.2 P, 0.3 S, 0.2 Cl, 0.2 K	1.030
Liver (healthy)	10.2	13.9	3.0	71.6	0.2 Na, 0.3 P, 0.3 S, 0.2 Cl, 0.3 K	1.060
Skeletal muscle	10.2	14.3	3.4	71.0	0.1 Na, 0.2 P, 0.3 S, 0.1 Cl, 0.4 K	1.050
Blood	10.2	11.0	3.3	74.5	0.1 Na, 0.1 P, 0.2 S, 0.3 Cl, 0.2 K, 0.1 Fe	1.060

Table 3.4: Chemical composition of soft tissue reference materials, taken from [ICRU 92]. The table lists mass percentages of the four main elements **H**ydrogen, **C**arbon, **N**itrogen and **O**xygen as well as other elemental contributions. The tissue density is given in the right most column.

Direct material identification

The previous applications are based on the $\mu(E, \mathbf{r})$ result of the LSR procedure. In this section we demonstrate that the LWF result can be used for a direct identification of spectral attenuation functions. Like in the previous section the analysis of the algorithmic accuracy is the main target.

We can rewrite Eq. (3.25) as

$$\left| \bar{\mu}_i(\mathbf{r}) - \int_0^\infty \Omega_i(E, \mathbf{r}) \mu_t(E, \mathbf{r}) \mathrm{d}E \right| = \epsilon_i \tag{3.34}$$

For a known LWF $\Omega_i(E, \mathbf{r})$, a measurement result $\bar{\mu}_i(\mathbf{r})$ can be compared against a model function $\mu_t(E, \mathbf{r})$. The index i corresponds to a spectral measurement channel and t is an index to a list of different spectral attenuation functions. The resulting ϵ_i is a measure for the deviation between the model function and the CT measurement data. For a Dual Energy measurement, the net deviation can be expressed by e.g. a quadratic sum $\epsilon = \sqrt{\epsilon_1^2 + \epsilon_2^2}$. When we compare a comprehensive list of materials $\mu_t(E, \mathbf{r}), t = 1 \ldots T$ against the measurement data, the most probable material can be identified.

We have applied a basic material identification approach to the thorax phantom case D. The LWF estimates were computed in two LSR iterations with 80 kV and 140 kV Dual Energy input data. The 80 kV input data is shown in Fig. 3.12a. The identification process was performed on the soft-tissue components of the phantom. In Table 3.2, this corresponds to the materials 'average soft tissue' (I), 'liver' (III), 'skeletal muscle' (V) and 'blood' (XIV). As shown in Table 3.4, the chemical compositions of these materials differ only slightly.

The results of the identification process are presented in Fig. 3.12b. All color coded voxels were assigned to one of the reference tissues, i.e. no intermediate probabilities are shown. We have average soft tissue marked in yellow, liver tissue shown in green, skeletal muscle in blue and blood is marked in red. Overall, a good separation between the tissue types is achieved, especially considering the significant

beam-hardening artifacts in Fig. 3.12a and the small chemical deviations of the materials. Errors are mainly present for voxels affected by partial volume effects as these cannot be covered by this single voxel oriented approach. Some blood voxels are erroneously identified as liver tissue due to their particular similarity in terms of composition and density.

It should be noted clearly that these results represent a proof of concept. Practical applications are strongly limited by the input image noise and the associated impact on result precision as well as the overall system stability. Even in the absence of noise, the direct material identification cannot distinguish between two a-priori chosen attenuation functions which yield the same two measurement results.

Still, the results demonstrate that an appropriate algorithmic accuracy for demanding soft tissue identification tasks can be achieved. Beam-hardening is treated quantitatively and the tissue is identified correctly over the whole image plane. The method does not suffer from transformation non-linearities or noise correlations typically found in alternative indirect segmentation methods e.g. based on effective atomic number and density or basis material coefficients.

Note also that the results of this simple approach are based on per voxel comparisons only. They do not employ any shape or connectivity information. In practical realizations, the comparison method can be adapted to a specific task and additional image processing might be required to ensure a desired robustness. The distance measures can, for instance, be used as input data to a standard organ segmentation algorithm.

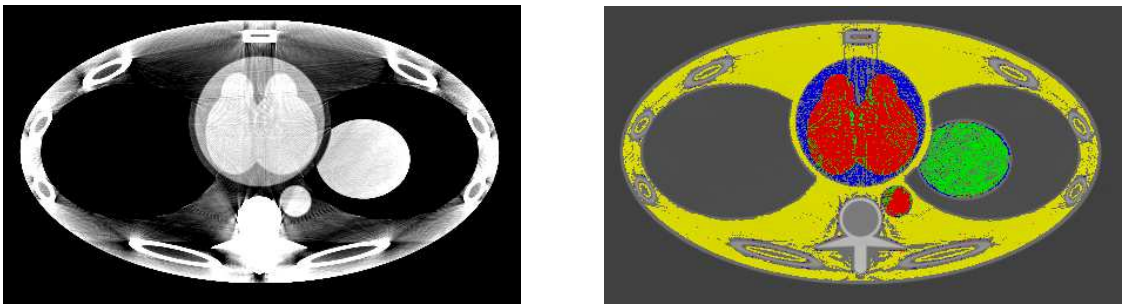

(a) (b)

Figure 3.12: (a) 80 kV input image (attenuation values $\bar{\mu}(\mathbf{r})$, center: $0.220\,\mathrm{mm}^{-1}$, width: $0.012\,\mathrm{mm}^{-1}$); (b) Color-coded identification result. Blue: skeletal muscle, red: blood, green: liver, yellow: average soft tissue

3.4 Conclusions

We have provided an overview on QCT algorithms and presented BMD, one of the basic methods for most QCT algorithms. In the second part of this chapter we introduce a novel quantitative image-based reconstruction framework for spectral CT applications. The LSR algorithm yields two results: First, the LWF $\Omega(E, \mathbf{r})$ can be determined. The LWF defines the local weighting of the object ground truth $\mu(E, \mathbf{r})$

to measured effective attenuation values $\bar{\mu}(\mathbf{r})$. At the same time, estimates for the attenuation coefficient $\mu(E, \mathbf{r})$ as the object's ground truth are obtained.

The LSR process consists of two nested update loops: An initial estimate of the LWF is chosen, for instance the SWF can be used as an initial guess. Then a quantitative spectral CT method like the Basis Material Decomposition yields a first estimate of the spectral attenuation coefficient $\mu(E, \mathbf{r})$. An updated LWF is calculated from this and so forth.

In order to evaluate the properties of the LWF and the accuracy and precision of the obtained spectral attenuation coefficients, we have analyzed five different practical measurement and simulation set-ups:

In a first group of evaluations, we have considered the basic properties of the LWF. As input data, measurement data of an upper abdomen phantom and simulations of a 40 cm water phantom were obtained. The results on the measured abdomen phantom indicate that the basic shape of the LWF is given by the System Weighting Function. The LWF is scaled down by object self-attenuation. Unlike the SWF, the LWF is not normalized to one. For example, its integral value is found to be reduced by about 5% at the center of the simulated 40 cm water phantom. This is equivalent to the reduction of the effective attenuation coefficient in standard CT images. Furthermore, the LWF is shaped by the spectral attenuation coefficient of the local attenuator. The findings correspond to the mathematical structure of the LWF definition.

The second group of evaluations covers energy calibration as a practical application. For a measured 25 cm water phantom, we obtained energy-calibrated effective 80 kV and 140 kV images with no beam hardening artifacts. The remaining ground truth deviations were found to be in the range of 2 to 3 %. This is a remarkable accuracy considering that measurement impacts like the bow-tie filter induced beam hardening, geometrical alignment issues and the uncertainty of SWF had to be included successfully.

The algorithmic accuracy and precision was further evaluated by simulated data of an anthropomorphic thorax phantom. It is based on geometrical definitions of $\mu(E, \mathbf{r})$ regions of body materials. We analyzed the obtained $\mu(E, \mathbf{r})$ data for ground truth accuracy and precision. Energy calibrations to $[60, 80, 100, 120, 140]$ kV tube acceleration voltage SWFs and mono-energetic 141 keV and 511 keV SWFs prove a convergence to ground truth in the iterative process. The convergence is found to be exponential. However, at the same time noise is amplified with each iteration step. This degrades the precision of the obtained $\mu(E, \mathbf{r})$ parametrization.

The optimum choice of iteration steps depends on the chosen application. For the homogenization of tissue values typically found in beam hardening and energy calibration tasks, one iteration might be enough to yield sufficient results in many cases. For quantitative spectral applications two iterations are probably the optimum choice. Since the chosen phantom set-up reflects typical medical CT objects in terms of object diameter and material components, we expect similar convergence results for arbitrary CT slice settings.

As an example for a quantitative spectral CT application we have performed an iodine density measurement in the heart chambers and aorta of the simulated thorax phantom. We find relative deviations in the range of 10^{-3} between the ground truth densities and the estimated iodine concentrations. Finally it was shown that the

LWF result can be used to perform a direct material identification with appropriate algorithmic accuracy.

In terms of computational effort, one LSR iteration step requires one Basis Material Decomposition of the input attenuation value data, one forward projection per each basis material coefficient image and one filtered back-projection for each input weighting. For one to two iteration steps the total computational effort is thus easily manageable in practical applications.

In summary we have shown that potential applications of the LSR framework like energy calibration and image-domain quantitative spectral algorithms are feasible. The expected algorithmic accuracy in the sub-percent range seems to be sufficient for practical applications. Still, the precision of the obtained object parameterizations depends on the noise transfer of the iterative algorithm. For the results of this work, we find that an optimum trade-off exists where the ground truth is reconstructed with only a minor precision decrease. Understanding and controlling the noise transfer of the algorithm warrants further research. Furthermore, we have shown that beam hardening corrections, mono-energetic attenuation coefficient images and attenuation correction maps for SPECT/CT and PET/CT can be written in one common energy calibration formula. It gives an analytic insight into the spectral properties of CT reconstruction. The LSR framework enables quantitative spectral CT applications in the image-domain. In particular, we can include the effects of object self-attenuation as well as the physics of the measurement system and the reconstruction algorithm.

Chapter 4

Dose Reduction

CT image quality is predominantly influenced by the SNR and the image MTF. Noise reduction techniques are an essential tool in medical CT, as image noise greatly influences the detectability of details in a reconstructed CT volume and thus its diagnostic value. As the most dominant noise component in CT, quantum noise, is directly related to detected X-ray intensity, successful noise reduction leads to a reduction of patient X-ray dose [Hilt 04].

As shown in the previous chapter, QCT applications tend to be particularly sensitive to image and measurement noise. The different nature of the input data compared to classical single-energy CT requires special means of pre-processing. This chapter gives a roundup of general principles of noise reduction in FBP-based CT reconstruction and then introduces two novel methods for noise reduction of CT data: The first one is a post-reconstruction technique based on intensity statistics. It is explicitly adapted to multi-energy CT data. The second one is a novel frequency-based filter that combines the advantages of pre- and post-reconstruction techniques to provide an edge-preserving noise reduction that can be adapted to various diagnostic demands. It is an enhanced version of the well-known bilateral filter using a structural similarity term instead of a photometric similarity. The structural similarity takes the CT measurement process into account.

4.1 Noise Reduction in CT

It is commonly agreed that Dual Energy scans should require about the same total X-ray dose as the corresponding single-energy scan. This calls for effective noise reduction techniques in Dual Energy CT. In general, dose efficiency of CT acquisitions is driven by several means including dynamic exposure control [Gres 00], tube filters like the wedge filter [Mail 09] and optimized detector designs that maximize the DQE [Rose 46, Rabb 87] as, for instance, shown in Chapter 2. For FBP-based reconstructions [Feld 84, Kak 01], projection- or image-domain filters are applied to reduce the required patient dose. The most common filtering strategy applied in medical CT scanners consists in modifying the high-pass reconstruction kernel used for FBP in a way that high frequencies are less amplified or blocked [Chew 78]. For most diagnostic tasks, the relevant information is supposed to be primarily contained in the lower-frequency components of the image. Each CT manufacturer offers a

broad spectrum of task-specific reconstruction kernels that block irrelevant frequency components and consequently noise.

More advanced noise reduction techniques use adaptive filters. This type of filters steers the filter strength according to a noise estimate and causes less smoothing in regions where noise is low, i.e. the X-ray intensity is less attenuated. For instance, an adaptive filter for reducing noise induced streak artifacts in very strongly attenuated data is shown in [Hsie 98]. Kachelrieß et al. [Kach 01] have introduced an adaptive filter that is applied in projection domain and features non-linear filtering in channel, reading and z-direction for various types of projection data such as helical cone-beam CT. In [Bors 08b], a method for wavelet-based denoising of projection data is introduced. This approach is especially suited for dual source data [Floh 06] with similar tube-voltage settings for two low-dose data-sets. It utilizes the noise correlations between the two aligned data-sets to construct an adaptive wavelet-based filter.

Well-known edge preserving filters have also been investigated. Edge-preserving anisotropic diffusion filters [Catt 92, Weic 98] can be adapted to CT data as shown in [Wang 05]. The purpose of this filter is to smooth along but not across edges. It relies on gradient information and noise can deteriorate the edge information and erroneously preserve noise-induced structures. As a consequence true edges are weakened or false ones are enhanced. This problem has to be avoided by carefully choosing the smoothing parameters for the gradient estimation based on local noise estimates. Schaap et al. [Scha 08] have developed an image-based fast denoising method based on anisotropic diffusion. This method features an adapted diffusion filter to preserve small structures.

Bilateral filtering [Toma 98] tries to achieve a similar goal by combining frequency- and intensity-based smoothing. This filter type steers the smoothing locally according to distance and similarity of neighboring intensity values. In CT, frequency-based noise reduction filters are usually applied in the projection domain as the spectral noise properties in the CT-image or -volume domain can hardly be derived analytically. The image noise is inhomogeneous and non-stationary and estimating local noise properties is complex, for instance Borsdorf et al. [Bors 08a] demonstrate how to estimate local variance and analyze noise correlations in the image domain for CT-data reconstructed with indirect FBP. A Monte Carlo-based local NPS estimation technique is shown in [Bald 10a].

All of these strategies have one common goal: Reducing the noise level of the reconstructed images while maintaining a desired level of image sharpness and details.

4.2 Value-based Noise Reduction for Multi-Energy CT

In this section we introduce a noise reduction technique that is solely based on joint intensity statistics of the two Dual Energy datasets. Most multi-energy modalities have an unequal noise distribution between images due to tube limitations and/or strong absorption in low-kVp images. The individual images from a multi-energy scan are much noisier than an image of a single energy scan, as the overall scan dose should be in an identical range. Quantitative CT algorithms based on Dual Energy

data are very sensitive to image noise. Basis Material Decomposition (Sec. 3.2.2), for instance, suffers from noise amplification and artifacts in the resulting basis material coefficient images. For image-based BMD this is caused by the ill-posedness of the system of linear equations that defines the link between reconstructed attenuation values and basis-material coefficients. In projection-based BMD, a system of non-linear equations is solved numerically. Projection noise has a negative influence in the precision of the resulting projected basis-material densities and consequently may lead to visible artifacts in the reconstructed basis material images. For other QCT applications, like Rho-Z projection [Heis 03] or LSR (Sec. 3.3), similar problems arise.

The proposed Dual Energy noise reduction improves images from one energy weighting by using knowledge on the joint intensities from both datasets. As it is purely value-based and does not utilize any frequency information, it is compatible with the frequency-based filters explained above. Below, we explain the method and suggest combination strategies with prevalent frequency-based filters.

4.2.1 Method

The noise-reduction method uses a low-kVp CT-volume $\bar{\mu}_1(\mathbf{r})$ and a high-kVp volume $\bar{\mu}_2(\mathbf{r})$ as input data. The voxel coordinate is indicated by $\mathbf{r}$. This method is neither restricted in terms of the number of multi-energy input data-sets nor their dimension. However, for practical reasons, the description focuses on Dual Energy data of two or three spatial dimensions. Our method estimates the most likely object attenuation values $\widetilde{\mu}_1(\mathbf{r})$ and $\widetilde{\mu}_2(\mathbf{r})$ for each measured $(\bar{\mu}_1(\mathbf{r}), \bar{\mu}_2(\mathbf{r}))$-pair by a gradient ascent in the joint probability density.

Due to the attenuation characteristics described in Sec. 1.6.1 and the tube current and dose limitations described in Sec. 1.3, a dual-energy set usually consists of a relatively noisy low-kVp dataset which exhibits high soft-tissue contrasts and a high-kVp dataset with lower SNR but also lower noise. The following method uses these properties to derive noise estimates for both images from the joint statistics of the input images or volumes.

Joint probability density estimation: The first step estimates the joint probability density $P(\bar{\mu}_1, \bar{\mu}_2)$ for all $(\bar{\mu}_1(\mathbf{r}), \bar{\mu}_2(\mathbf{r}))$-pairs. Here, $\bar{\mu}_1$ and $\bar{\mu}_2$ denote the random variables and $\bar{\mu}_1(\mathbf{r})$ and $\bar{\mu}_2(\mathbf{r})$ their measured realizations at location $\mathbf{r}$. Several methods are available for this purpose, e.g. computing histograms, data clustering or Parzen windowing [Parz 62]. We use kernel density estimation using a bivariate, uncorrelated Normal Distribution as kernel function. This method offers the possibility to apply smoothing to the $P(\bar{\mu}_1, \bar{\mu}_2)$-estimate by adjusting the bandwidth of the kernel:

$$\mathcal{N}_{(\sigma_1,\sigma_2)}(\bar{\mu}_1, \bar{\mu}_2) = \frac{1}{2\pi\sigma_1\sigma_2} \exp\left\{-\frac{1}{2}\left(\frac{\bar{\mu}_1^2}{\sigma_1^2} + \frac{\bar{\mu}_2^2}{\sigma_2^2}\right)\right\}. \tag{4.1}$$

The standard deviations σ_1 and σ_2 are the bandwidth parameters. Several different approaches have been investigated to provide optimal bandwidth parameters for multivariate kernel functions in a sense that the joint probability density estimate $P(\bar{\mu}_1, \bar{\mu}_2)$ converges fastest to the true joint density [Scot 92, Jone 96]. Plug-in

bandwidth selectors (e.g. [Enge 94]) or smoothed bootstrap methods (e.g. [Tayl 89, Fara 90]) are among the most commonly used techniques. For our method, however, these bandwidths are not necessarily optimal, since we want to use the smoothing parameter in the joint densities to steer the strength of the denoising. Slightly over-smoothed density estimates yield better noise suppression at the cost of increased bias. The selected bandwidth parameter set is denoted (b_1, b_2) below. Once a set of bandwidth parameters is selected, the density estimate $P_{b_1,b_2}(\bar{\mu}_1, \bar{\mu}_2)$ can be computed by a convolution:

$$\begin{aligned} P_{b_1,b_2}(\bar{\mu}_1, \bar{\mu}_2) &= \mathcal{N}_{(b_1,b_2)}(\bar{\mu}_1, \bar{\mu}_2) * \textstyle\sum_i \delta(\bar{\mu}_1 - \bar{\mu}_1(\mathbf{r}_i), \bar{\mu}_2 - \bar{\mu}_2(\mathbf{r}_i)) \\ &= \textstyle\sum_i \mathcal{N}_{(b_1,b_2)}(\bar{\mu}_1 - \bar{\mu}_1(\mathbf{r}_i), \bar{\mu}_2 - \bar{\mu}_2(\mathbf{r}_i)) \end{aligned} \tag{4.2}$$

The expression $\delta(\bar{\mu}_1, \bar{\mu}_2)$ denotes the Dirac distribution located at $(\bar{\mu}_1, \bar{\mu}_2)$.

Noise estimation: The next step is to estimate true attenuation values for each pair of measured values by analyzing $P_{b_1,b_2}(\bar{\mu}_1, \bar{\mu}_2)$. In order to find the most probable true $\bar{\mu}_1$-value for a measured pair of values $(\bar{\mu}_1(\mathbf{r}), \bar{\mu}_2(\mathbf{r}))$, the $\bar{\mu}_2(\mathbf{r})$-value is kept fixed and a gradient ascent along the $\bar{\mu}_1$-direction within the density estimate is performed.

The gradient direction is given by

$$G_1(\bar{\mu}_1, \bar{\mu}_2) = \left(\operatorname{sgn} \left\{ \frac{\partial}{\partial \bar{\mu}_1} \left(P_{(b_1,b_2)}(\bar{\mu}_1, \bar{\mu}_2) \right) \right\}, 0 \right). \tag{4.3}$$

Figure 4.1 shows an example for this procedure. This gradient ascent approach does not employ any step width control. The step width is implicitly given by the sampling of the joint histogram.

The resulting local maximum for $\bar{\mu}_1(\mathbf{r})$ is called $\widetilde{\mu}_1(\mathbf{r})$. It represents the most probable $\bar{\mu}_1$-value for the measured intensity pair with fixed $\bar{\mu}_1(\mathbf{r})$. The distance

$$d_1(\mathbf{r}) = |\widetilde{\mu}_1(\mathbf{r}) - \bar{\mu}_1(\mathbf{r})| \tag{4.4}$$

is an estimate for the noisiness of $\bar{\mu}_1(\mathbf{r})$. The process of finding the $\widetilde{\mu}_2$-value works analogously: The gradient ascent is performed in $\bar{\mu}_2$-direction. This leads to the estimates $\widetilde{\mu}_2(\mathbf{r})$ and $d_2(\mathbf{r})$. The values $\widetilde{\mu}_1(\mathbf{r}), \widetilde{\mu}_2(\mathbf{r})$ and $d_1(\mathbf{r}), d_2(\mathbf{r})$ can be used for noise reduction using the following key principle: If $d_1(\mathbf{r})$ is small, the actually measured value $\bar{\mu}_1(\mathbf{r})$ is very close to its next local maximum $\widetilde{\mu}_1(\mathbf{r})$. If the according distance $d_2(\mathbf{r})$ is relatively large, this is an indication that $\bar{\mu}_2(\mathbf{r})$ is relatively noisy compared to $\bar{\mu}_1(\mathbf{r})$ and should be replaced by the most likely $\widetilde{\mu}_2(\mathbf{r})$ estimated from the measurement $\bar{\mu}_1(\mathbf{r})$.

Noise reduction: The quality of the estimates $\widetilde{\mu}_1(\mathbf{r})$ and $\widetilde{\mu}_2(\mathbf{r})$ is affected by noise in the original intensity pairs $(\bar{\mu}_1(\mathbf{r}), \bar{\mu}_2(\mathbf{r}))$: High noise in $\bar{\mu}_1(\mathbf{r})$ and $\bar{\mu}_2(\mathbf{r})$ generally worsens both estimates, low noise in the $\bar{\mu}_1(\mathbf{r})$-value increases the quality of the estimate $\widetilde{\mu}_2(\mathbf{r})$ and vice versa. The noise-reduction process should use a measure that takes these properties into account and adjusts the strength of the correction process accordingly. The following measure offers these properties and allows to govern the strength of the filter by a single parameter:

$$\widehat{\mu}_1(\mathbf{r}) = \alpha(\mathbf{r}) \cdot \bar{\mu}_1(\mathbf{r}) + (1 - \alpha(\mathbf{r})) \cdot \widetilde{\mu}_1(\mathbf{r}) \tag{4.5}$$

The correction strength is defined by a parameter α, the final noise-reduced image value is called $\widehat{\mu}_1(\mathbf{r})$; α is computed from the noisiness estimates Eq. (4.4) as follows:

$$\alpha(\mathbf{r}) = \left(\frac{d_1(\mathbf{r})}{d_t(\mathbf{r})} \right)^o \text{with } d_t(\mathbf{r}) = \sqrt{d_1(\mathbf{r})^2 + d_2(\mathbf{r})^2} \tag{4.6}$$

The parameter o determines the correction strength, values of $o = [0, 1]$ generally favor the $\widetilde{\mu}_1(\mathbf{r})$- resp. $\widetilde{\mu}_2(\mathbf{r})$-estimates whereas $o =]1, +\infty[$ directs the filter to use the estimates only when the image noise estimate is close to the overall noise estimate $d_t(\mathbf{r})$. In our experiments, we used $o = 5$.

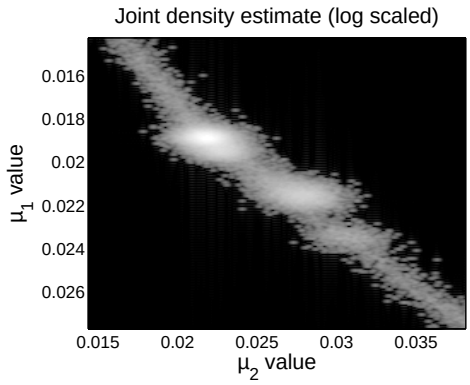

(a) PDF-estimate for small bandwidth.

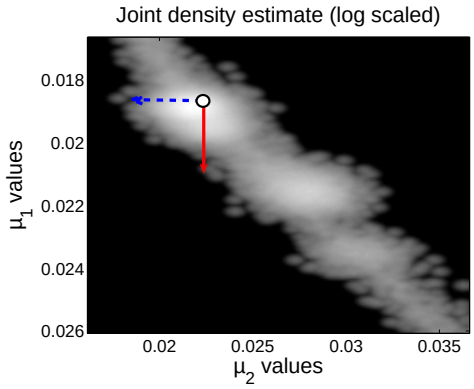

(b) PDF-estimate for large bandwidth.

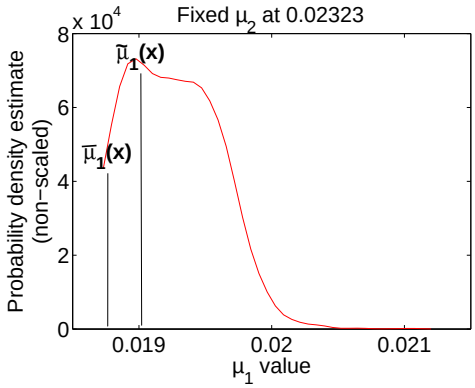

(c) Line plot for $\tilde{\mu}_1(\mathbf{x})$ estimation.

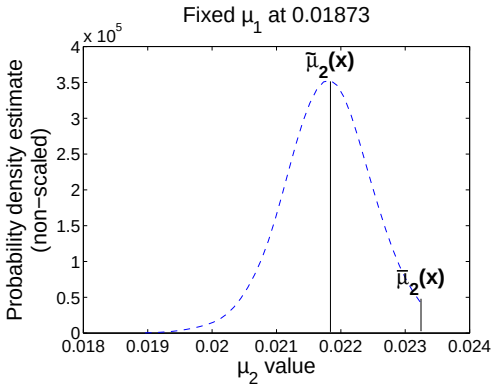

(d) Line plot for $\tilde{\mu}_2(\mathbf{x})$ estimation.

Figure 4.1: Examples for the gradient ascent procedure with $\bar{\mu}_1(\mathbf{r}) = 0.0187\,\mathrm{mm}^{-1}$ and $\bar{\mu}_2(\mathbf{r}) = 0.0232\,\mathrm{mm}^{-1}$. Arrows indicate the gradient direction, the start point is located at the base of the arrows.

Parameter selection: The strength of the intensity smoothing is governed by the two bandwidth parameters. Good values for these parameters depend on image noise and desired tissue contrast. Noise in CT images is non-stationary and depends on dose settings, object attenuation and image location, thus the optimal parameters

vary with the location $\mathbf{r}$ and the measured attenuation values $(\bar{\mu}_1(\mathbf{r}), \bar{\mu}_2(\mathbf{r}))$. The bandwidth parameter b_1 would read $b_1(\mathbf{r}, \bar{\mu}_1)$ and b_2 would read $b_2(\mathbf{r}, \bar{\mu}_2)$ in this case. These degrees of freedom have to be limited since concise knowledge on all noise properties is not available and its application is not feasible due to restrictions in computation time. We aim to apply only a simple model for the bandwidth parameters that relies on few rough estimates but still meets the following criteria:

1. As little free parameters as possible.

2. Good adaption of bandwidth parameters to all input images.

3. Lowest achievable bias for soft-tissue intensities to maintain soft tissue contrast.

4. Appropriate noise-reduction across the whole intensity range.

We can drop the spatial dependency of the bandwidth parameter as the spatial variance of noise properties usually varies little within the important center region of CT slice images. We choose b_1 as the only free parameter. It is selected for the reference intensity of $\bar{\mu}_r = 0\,\mathrm{HU}$ (CT-value for water) in the $\bar{\mu}_1$-image. Automatically computing an appropriate b_2 value for the $\bar{\mu}_2$-image has to take the relative contrast and noise of the second image into account. We generate a set

$$\mathbf{R} = \{\mathbf{r}_i | \bar{\mu}_{1,s_1} < \bar{\mu}_1(\mathbf{r}_i) < \bar{\mu}_{1,s_2}\} \tag{4.7}$$

containing all soft tissue voxels of image 1. The boundaries for soft-tissue intensities are usually known for a specific tube acceleration voltage. Next we estimate the standard deviation $\sigma_{1,s}$ on $\bar{\mu}_1(\mathbf{r}_i)\,\forall\, r_i \in \mathbf{R}$:

$$\sigma_{1,s}^2 = \frac{1}{|\mathbf{R}|} \sum_{\mathbf{r}_i \in \mathbf{R}} (\bar{\mu}_1(\mathbf{r}_i) - m_{1,s})^2. \tag{4.8}$$

The average value over all soft-tissue values in image 1 is denoted $m_{1,s}$. Analogously $\sigma_{2,s}$ is computed on $\bar{\mu}_2(\mathbf{r}_i)\,\forall\, r_i \in \mathbf{R}$. The value $\sigma_{2,s}$ can differ from $\sigma_{1,s}$ for two reasons: A different noise level and/or a different tissue contrast in the second image. A lower noise level or less contrast require a smaller bandwidth whereas a higher noise level or more contrast call for a higher bandwidth. Consequently we set

$$b_2 = b_1 \cdot \frac{\sigma_{2,s}}{\sigma_{1,s}}. \tag{4.9}$$

For the example of a second image with a higher tube acceleration voltage at the same tube current, a lower noise level and reduced tissue contrast is observed. This case leads to a reduced bandwidth b_2. If the tube current is adjusted appropriately so that the noise level is kept similar in both images, the reduced tissue contrast prohibits strong noise reduction on the high-kVp image and the according bandwidth parameter will be reduced.

Combination with Frequency Domain Filters

This noise reduction technique can be used together with frequency domain filters by consecutively applying the value-based filter and the frequency domain filter. In this case, two issues should be taken into account: The order in which the filters are applied influences the result and the filter parameters of both filters have to be adjusted. The optimal parameters for applying one of the filters exclusively are not necessarily optimal for the concatenated application of both filter types.

We propose an alternative way for enhancing frequency domain filters which use side-information computed from the image data: The side information can be computed on the noise reduced image whereas the frequency domain filter itself is applied to the original image. This way, the noise influence on the side information is weakened whereas the filter properties are mostly unaffected. For bilateral filters, the intensity differences with respect to the filtered point may be computed on the value-filtered image. For non-linear, anisotropic diffusion filters, the gradient information can be computed on the processed image whereas the diffusion takes place on the original image or – in case several iterations are needed – both images. Another example for this approach is *Guided Image Filtering* [He 10]. Here, the noise reduced image can be used as guide image whereas the filtering takes place on the original image.

This type of application allows to make use of advantages from both filters: Compared to standard diffusion filters, the gradient information is more reliable and requires less smoothing on the data used for gradient estimation. Compared to exclusively applying value-based noise reduction, it is guaranteed not to introduce any systematic value shifts in the filtering result.

Discrete sample space: As the input data for this algorithm is discrete, it has to deal with discrete estimate $P[\bar{\mu}_1, \bar{\mu}_2]$ of the joint probabilities. This can be achieved by integrating the multivariate Normal Distribution within the bins defined by a desired sampling grid. The choice of the grid size is an important issue, since performing gradient ascents on the estimated $P[\bar{\mu}_1, \bar{\mu}_2]$-function requires interpolation. As $P[\bar{\mu}_1, \bar{\mu}_2]$ is not smooth, interpolation methods like Natural B-Splines or frequency domain methods cause overshoots which lead to erroneous local extrema. Initially estimating $P[\bar{\mu}_1, \bar{\mu}_2]$ on a fine grid and using nearest neighbor interpolation during the gradient ascent procedures is a valid approach. A high grid resolution is necessary as it defines the maximum precision of the estimates in this case. For common 12-bit CT data a 4096×4096 grid exhibits the maximum precision. The gradient ascent is then simply carried out by ascending along the directions where the sample values increase.

4.2.2 Evaluation and Results

In order to evaluate the theoretical limits of the proposed denoising method against ground truth data, we conducted several simulations and a radiological evaluation.

1. *Contrast-to-noise ratio*: Evaluation of the achievable CNR-gain for various contrasts and dose-levels.

2. *Quantitative accuracy and precision*: Noise reduction and quantitative accuracy for energy calibration application using Basis Material Decomposition.

3. *Radiological evaluation*: Perceived and measured noise reduction while maintaining visibility of important image details.

The simulations involve an analytic forward projection of a geometrically defined thorax phantom and a standard filtered back-projection (see Fig. 4.2). The tissue compositions were taken from the ICRU Report 46 [ICRU 92] and the elemental mass attenuation coefficients from [Berg 98]. In order to avoid beam hardening artifacts, we created Dual Energy data-sets with mono-chromatic radiation at 54 keV and 73 keV which corresponds to the effective energy of 80 kVp and 140 kVp scans. The possible improvement in contrast-to-noise ratio of the data was evaluated by placing various small lesions inside the liver (see Fig. 4.2b). The contrast of lesion to healthy liver tissue was varied between scans by varying the density of the cirrhotic liver tissue. The CNR changes are evaluated with respect to varying noise / dose levels, varying tissue contrasts and varying bandwidth settings.

A second synthetic test aims at evaluating the quantitative accuracy and precision when value-based denoising is used as a processing technique for QCT algorithms. It was carried out on the same phantom. We perform a basis material decomposition on the Dual Energy data and investigate the changes in basis material coefficients between ground truth, original data and processed data. This application requires a high accuracy of the CT values. Any shift of these values might deteriorate the quantitative performance of the BMD. On the other hand, the precision of the BMD suffers very much from noise in the input data. The processing should improve the precision of BMD whereas the accuracy may not be affected severely.

(a) (b) (c)

Figure 4.2: (a) Thorax phantom (with a small water cylinder at the top-left corner used for water scaling); (b) Low contrast lesions for CNR evaluation. (c) Lesion example at 80 kVp with 14 HU contrast and 70000 primary photons (intensity window center: 45 HU, width: 35 HU).

Additionally we investigated seven cases of real measurements of patient data. The input images were all Dual-Source images acquired with a Siemens Definition or a Siemens Definition Flash CT-scanner (Siemens AG, Forchheim, Germany). The Siemens Definition device uses 80 kVp and 140 kVp tube voltages, whereas the Definition Flash also uses 100 kVp and 140 kVp with an additional tin-filter for the high-energy spectrum that improves spectral separation. These cases are subjectively evaluated by three radiologists.

Contrast-to-Noise Ratio

The possible improvement in contrast-to-noise ratio of the data was evaluated by placing various small lesions inside the liver (see Fig. 4.2b). Four different contrasts were evaluated at five noise levels. The liver and cirrhotic liver tissue composition was chosen according to the ICRU report 46 with a density of $1.060\frac{\mathrm{g}}{\mathrm{cm}^3}$ for the healthy liver tissue. The liver lesion densities were set to $1.040, 1.045, 1.050$ and $1.055\frac{\mathrm{g}}{\mathrm{cm}^3}$. The resulting contrasts are $29, 24, 19$ and $14\,\mathrm{HU}$ for the effective $80\,\mathrm{kVp}$ spectrum and $23, 18, 13$ and $8\,\mathrm{HU}$ for the $140\,\mathrm{kVp}$ spectrum. The ratio of quanta in the low and high energy spectra was kept fix at 3 to 1. Six different bandwidths were selected for the parameter b_1: $0.5, 1.0, 2.0, 4.0, 7.0$ and $11.0\,\mathrm{HU}$. The according b_2-values were determined automatically according to Eq. (4.9). Figure 4.3 shows an excerpt of the resulting CNR-values. The results show an improvement in all cases as long as an appropriate bandwidth parameter is chosen. The choice of a too large bandwidth can, however, decrease the resulting CNR for very low contrasts. The possible dose reduction can be deduced by comparing the number of primary photons needed to get a CNR value similar to the original one. In the evaluated cases, 70% to 40% of the original photon numbers yield similar CNR values.

Quantitative Accuracy and Precision

For this evaluation we performed a two-material BMD with the basis materials water and femur bone on the thorax phantom introduced above. The liver lesions were removed and the medium noise case with $1.4 \cdot 10^5$ primary photons for the effective $80\,\mathrm{kVp}$ spectrum was selected. Here we use BMD to estimate the spectral attenuation coefficients $\mu(E, \mathbf{r})$ at every voxel position $\mathbf{r}$. These coefficients are then weighted with an effective $120\,\mathrm{kVp}$ spectrum $w_{120\,\mathrm{kVp}}(E)$ to create a virtual $120\,\mathrm{kVp}$ image from the input images by computing

$$\bar{\mu}_{120\mathrm{kVp}}(\mathbf{r}) = \int_0^\infty w_{120\,\mathrm{kVp}}(E)\mu(E, \mathbf{r})\mathrm{d}E. \tag{4.10}$$

The resulting image is compared with the analytically computed ground truth data in terms of mean-shift and standard deviation. The value-based noise reduction may cause a minor shift of the mean attenuation values along with noise reduction. This evaluation is meant to quantify the trade-off between noise reduction and decrease in quantitative accuracy caused by the mean shift.

Table 4.1 shows the results at different bandwidths for the tissues average soft tissue (large area), liver (medium area) and red marrow (small area). Noise suppression is achieved for all tissues at a tolerable mean shift. At lower bandwidths the mean shift is negligible compared to the overall system accuracy. At very high bandwidths the noise standard deviation can get worse in some cases since the gradient ascent tends to the wrong direction for some voxels.

HU Shifts and Noise Reduction on Measured Patient Data

Figure 4.4 shows a dual energy head scan at $80\,\mathrm{kVp}$ and $140\,\mathrm{kVp}$ tube voltage. The acquisition was made with a Siemens Definition CT using a D20f reconstruction

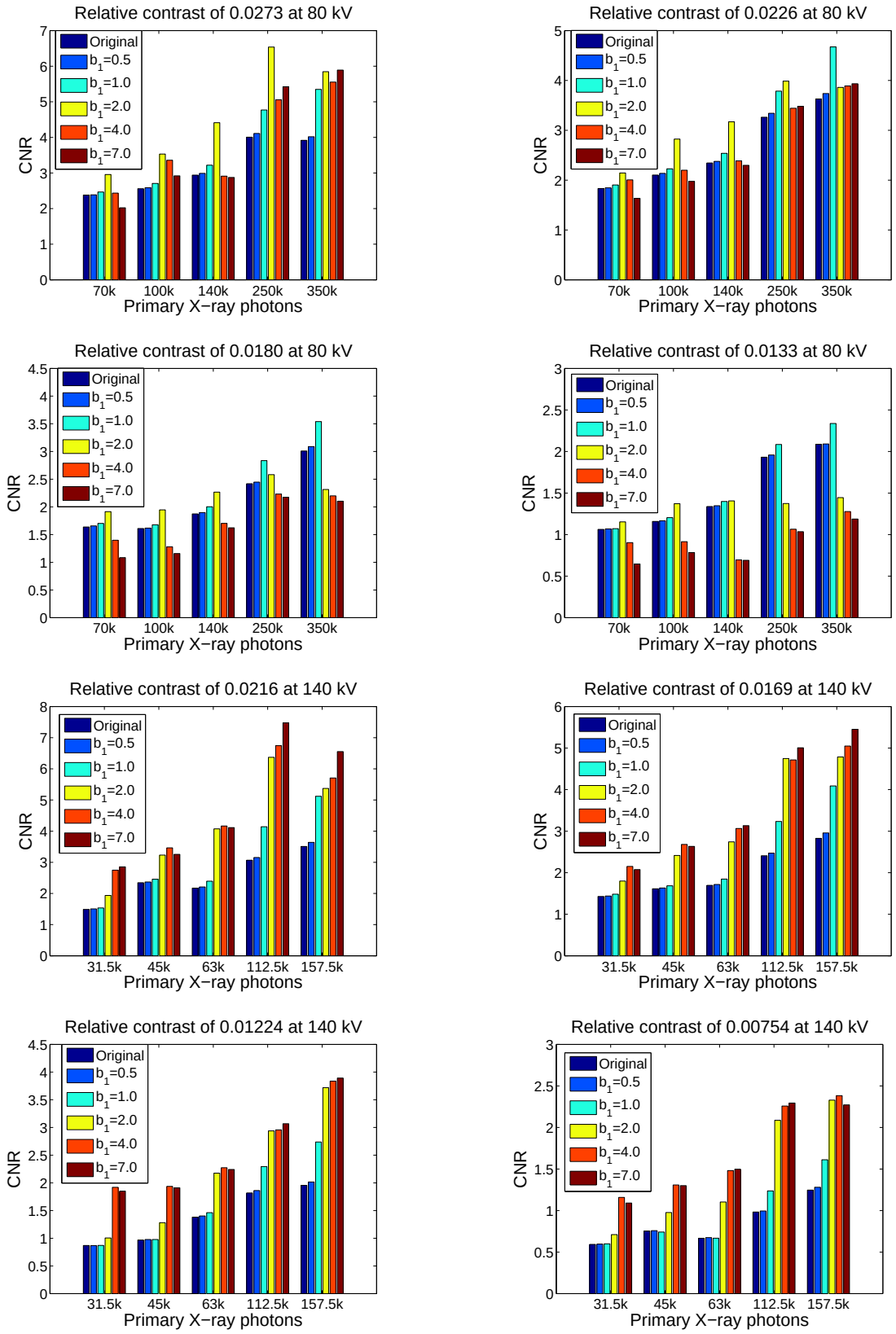

Figure 4.3: CNR test results for different contrasts at 80 kVp and 140 kVp tube voltage and selected noise reduction parameters. Contrasts and bandwidths given in mm^{-1} (integrated attenuation values).

Bandwidth	**Average soft tissue**	**Healthy liver**	**Red Marrow**
Ground Truth	2.072e-2	2.156e-2	2.050e-2
Original	2.060e-2 (1.605e-4)	2.140e-2 (1.655e-4)	2.039e-2 (3.711e-4)
1.08e-5	2.060e-2 (1.583e-4)	2.140e-2 (1.647e-4)	2.040e-2 (3.714e-4)
2.16e-5	2.060e-2 (1.567e-4)	2.140e-2 (1.639e-4)	2.040e-2 (3.708e-4)
4.33e-5	2.059e-2 (1.286e-4)	2.140e-2 (1.526e-4)	2.044e-2 (3.643e-4)
8.66e-5	2.058e-2 (0.859e-4)	2.139e-2 (1.001e-4)	2.051e-2 (3.204e-4)
1.52e-4	2.059e-2 (1.002e-4)	2.138e-2 (1.094e-4)	2.054e-2 (2.665e-4)
2.38e-4	2.059e-2 (0.960e-4)	2.137e-2 (1.145e-4)	2.054e-2 (2.067e-4)

Table 4.1: Ground truth and calculated mean (standard deviation) of attenuation values for virtual 120 kVp image from original and processed images. All quantities given in mm^{-1}. Minor shifts in the mean values of 1 % or less can be observed, the standard deviation resp. noise is reduced with increasing bandwidth except for very large bandwidths. The noise increase at large bandwith is caused caused by occasional gradient ascents into the wrong direction.

kernel. The image field of view (FOV) is set to 253 mm. We evaluated mean and standard deviation in a homogeneous region within the brain: In the 140 kVp example the mean value was shifted by 0.4 HU and the standard deviation dropped from 7.0 to 5.4 HU. In the 80 kVp image the mean shift caused by the filter was 1.9 HU and the standard deviation was reduced from 11.5 to 5.8 HU.

Figures 4.4(a) and (b) show a dual energy foot scan made with the same CT scanner. The FOV is 240 mm and a D50s reconstruction kernel was used. Here we get a mean shift of 2.1 HU (140 kVp) and 2.8 HU (80 kVp) whereas the standard deviation drops from 13.2 HU to 11.2 HU (140 kVp) and from 17.1 HU to 11.5 HU (80 kVp) with the identical filter parameters.

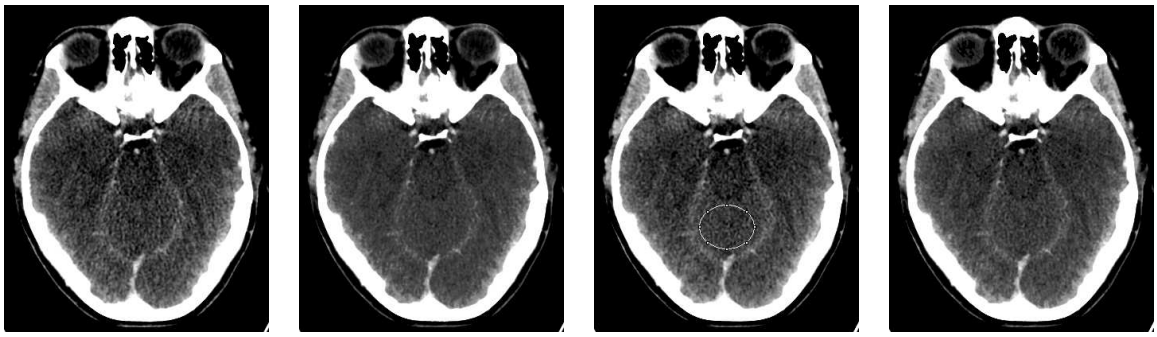

(a) (b) (c) (d)

Figure 4.4: Filter input and result for head image example. (a) Original 80 kVp image, (b) processed 80 kVp image, original 140 kVp image, filtered 140 kVp image. Original images are a courtesy of Prof. Dr. Andreas H. Mahnken, RWTH Aachen.

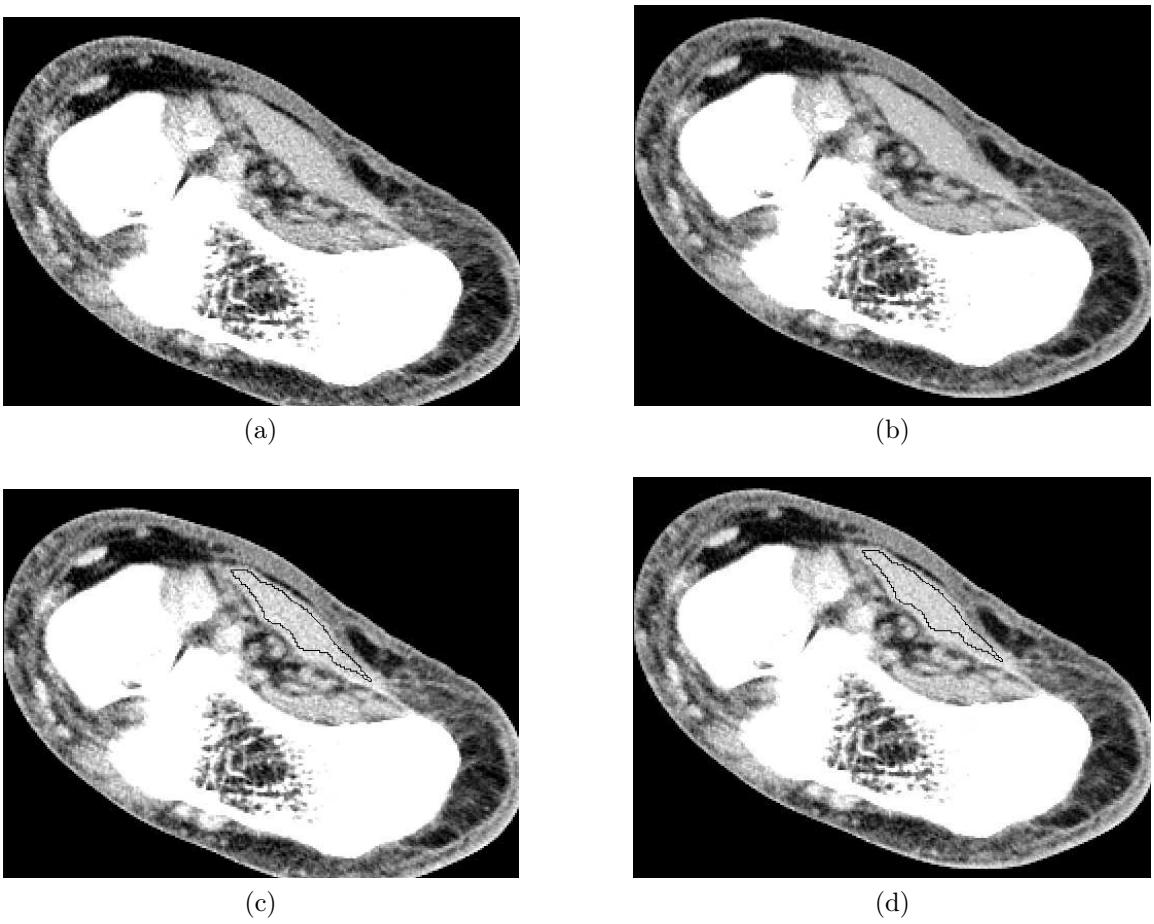

(a) (b)

(c) (d)

Figure 4.5: Filter input and result for foot image example (from left to right): Top row: Original 80 kVp image including evaluated region of interest, processed 80 kVp image (80 kVp, HU-window: center -12; width 108). Bottom row: original 140 kVp image, processed 140 kVp image (140 kVp, HU-window: center 1; width 131). The black outline in Figs. (c) and (d) marks the homogeneous region in which the noise estimate was computed. Original images are a courtesy of Prof. Dr. Andreas H. Mahnken, RWTH Aachen.

Dataset	**Head**	**Foot***	**Liver**	**Lung**
Noise Reduction	$-27\%/-25\%$	$-33\%^*$	$-29\%/-25\%$	$-29\%/-25\%$
Dataset	**Abdomen**	**Lower Abdomen**	**Pelvis**	
Noise Reduction	$-20\%/-32\%$	$-24\%/-18\%$	$-22\%/-22\%$	

Table 4.2: Average noise reduction for several different test scenarios with optimal bandwidth setting. First number corresponds to low-kVp image, second to high-kVp. Image noise was determined by evaluating the standard deviation in homogeneous image regions. (*) only 80 kVp image was evaluated for the *Foot* dataset.

Radiological Evaluation

Images from seven different Dual Energy scans were presented to three radiologists in a clinical environment. We selected data from typical examinations of different body regions with and without contrast agents and varying scan parameters. The input images were all Dual Source images acquired with a Siemens Definition or a Siemens Definition Flash CT-scanner (Siemens AG, Forchheim, Germany). The Siemens Definition device uses 80 kVp and 140 kVp tube voltages, whereas the Definition Flash uses 100 kVp and 140 kVp with an additional tin filter for the high-energy spectrum that improves spectral separation. The images were presented in randomly ordered pairs of original and denoised images with different bandwidth settings. The radiologists were asked to compare the image-pairs in terms of perceived noise level and visibility of important details. We evaluate to which extent the perceived and measured noise level can be reduced without important structures being visibly weakened compared to the original images. The corresponding bandwidth parameter for each dataset is called *optimal bandwidth* subsequently. Table 4.2 lists the average measured noise reduction for the optimal bandwidth on all datasets. All radiologists agreed that using the optimal bandwidth, a noise reduction could be perceived in all Dual Energy datasets.

4.3 Ray Contribution Masks for Iterative Structural Sinogram Filtering

As mentioned in Sec. 4.1, a variety of different filtering strategies for CT data exists. In this section, we give a short overview of the properties of pre- and post-reconstruction frequency-based filters and introduce a novel iterative frequency filter for CT data that combines the advantages of pre- and post-reconstruction filters.

CT noise-reduction filters can be divided into two main categories: Pre- and post-reconstruction filters. Pre-reconstruction filters like [Bors 08b, Hsie 98, Kach 01, Wang 05] are applied to the projection data. The FBP filter-kernel described in [Kak 01] is usually used as a simple pre-reconstruction kernel to steer the trade-off between noise suppression and image sharpness. The advantage of filtering in this domain is the simplicity of the noise characteristics: In the projection-space, the noise is almost white, only minor noise correlations are introduced by the detection process, for instance due to the optical crosstalk of scintillators described in Sec. 2.2. These effects have minor influence and usually can be neglected when designing noise-reduction filters. Additionally, the magnitude of the noise can easily be estimated from the measured attenuation values which enables noise adaption of the filter. Edge-preserving pre-reconstruction filters are, however, limited by the inferior contrast-to-noise ratio in sinogram space. Low-contrast structures in the imaged object can hardly be identified in projection space due to the noise in CT projections at standard dose levels. Additionally the contrast and CNR level even of homogeneous structures varies throughout the projections. Non-linear edge-preserving filters may not be able to preserve those structures throughout the whole sinogram which generally leads to a loss in sharpness. This may also cause inconsistencies in the projection data which results in streak-artifacts in the reconstructed image. Consequently, pre-reconstruction filters may deal with noise properties well, but have a weakness in recognizing the structure of the signal.

Post-reconstruction filters such as [Schi 06, Lu 03, Kese 92, Scha 08] operate on reconstructed images and thus cannot produce or intensify reconstruction artifacts. However, the noise properties are much more complicated in the reconstructed image as most reconstruction steps introduce noise correlations by filtering and interpolation [Bors 08a]. Furthermore, the structure and the local magnitude of the noise is dependent on the whole object instead of merely the local attenuation. As a consequence, edge-preserving frequency-based post-reconstruction filters need to model the quantum and detector noise and the noise propagation of the whole reconstruction process.

We introduce an Iterative Structural Sinogram (ISS) filter that operates in the projection domain and uses a projection model to recover local structures in the projection space from a pre-reconstructed image. It yields an individual local filter kernel for each measurement value. This local kernel adapts its smoothing directions to the local structures, thus the projection noise level can be strongly reduced while the sharpness of low-contrast structures can be preserved. It basically uses two parameters which allow steering its filter strength and smoothing properties so it can be adapted to the demands of specific diagnostic tasks. The filter is an extension of the bilateral filter [Toma 98]. It replaces the photometric similarity measure with

a more robust, CT-specific structural similarity term. It incorporates the measurement process by using a point-based projector and a pre-reconstructed image. The filter itself is not noise adaptive, but can be combined with projection-domain noise adaption techniques which steer the filter accordingly.

4.3.1 Theory of Structure Aware Filtering

The ISS filter uses a point-based forward projector to generate a local structure representation called Ray Contribution Mask (RCM). The similarities between neighboring RCMs are used to compute an individual, non-linear filter kernel for each projection value. Additionally, a RCM-driven range adaption is applied to avoid inconsistencies which may cause reconstruction artifacts.

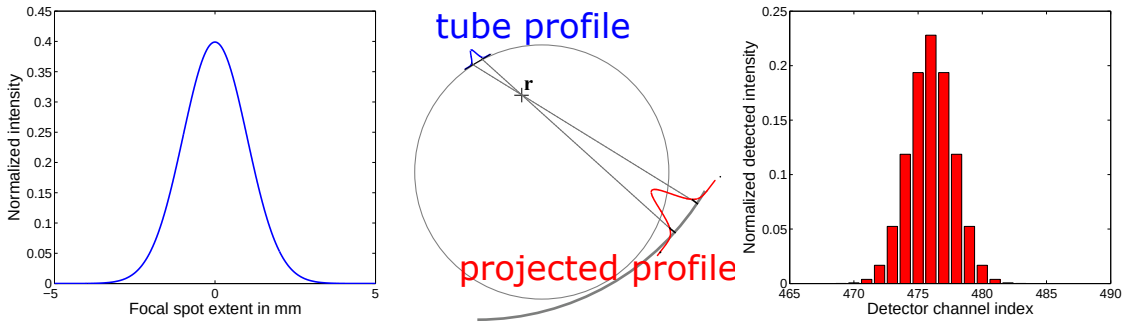

(a) (b) (c)

Figure 4.6: Illustration of the working principle of the projection operator $\mathcal{P}_{\mathrm{P}}(\mathbf{r}, \bar{\mu}(\mathbf{r}))$. Figure (a) shows a Normally distributed tube-profile, (b) illustrates the schematics of projection process and (c) is the according sampled projected tube-profile $\bar{\mu}_{\mathrm{L}}(c, r_1)$ for fixed reading r_1. A complete result of $\mathcal{P}_{\mathrm{P}}(\mathbf{r}, \bar{\mu}(\mathbf{r}))$ is displayed in Fig. 4.7.

Point-Based Analytic Projection

In practice, CT projections deviate from the ideal line-projection model. This is for instance caused by sampling and discretization effects, finite focal spot sizes and detector cross-talk. We use a flexible model of the projection process called point-based analytic projection which can take into account these effects. We denote this single detector row variant $\bar{\mu}_{\mathrm{L},\mathbf{r}}(c, r) = \mathcal{P}_{\mathrm{P}}(\mathbf{r}, \bar{\mu}(\mathbf{r}))$. This operator yields the contribution of a delta impulse at position $\mathbf{r}$ with a local attenuation of $\bar{\mu}(\mathbf{r})$ to the measured values at discrete channel indices $c \in \mathbb{Z}$ and readings $r \in \mathbb{Z}$. It may include effects like the focus beam profile and size and detector channel characteristics. The readings r correspond to the sampled gantry angles ν. In a CT system, this sampling process features a temporal integration of the projections during the reading time. The function $\mathcal{P}_{\mathrm{P}}(\mathbf{r}, \bar{\mu}(\mathbf{r}))$ yields the information where the contributions from a single point in the object space appear in the sinogram.

Figure 4.6 illustrates an exemplary output of the projection operator $\mathcal{P}_{\mathrm{P}}(\mathbf{r}, \bar{\mu}(\mathbf{r}))$ for a single gantry angle without temporal smearing of the projected tube profile. It

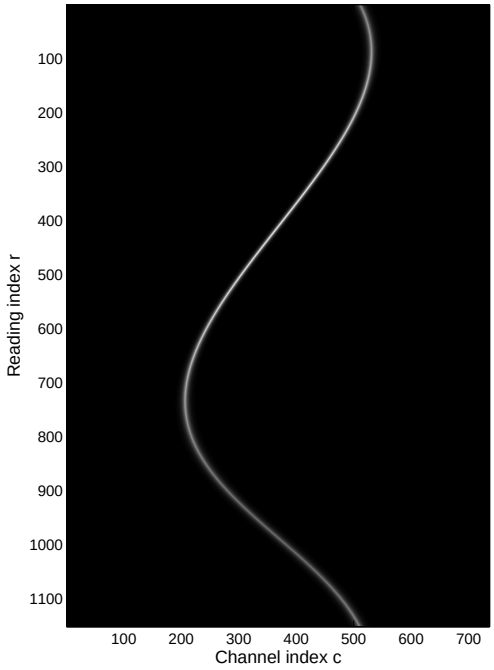

Figure 4.7: Result of point-based projection operator for all channels and readings $\bar{\mu}_{\mathrm{L},\mathbf{r}}(c,r)$ at a fixed location $\mathbf{r}$ (scale: arbitrary units). For visualization purposes, an extremely large X-ray focus of 9 mm FWHM was used.

features a normally distributed tube profile model (Fig. 4.6a), a geometric projection model (Fig. 4.6b) and a detection model (Fig. 4.6c). The latter may include detector pixel geometry, sampling properties like active pixel areas and detector cross talk. $\mathcal{P}_{\mathrm{P}}\left(\mathbf{r},\bar{\mu}(\mathbf{r})\right)$ can be viewed as a transform that takes the function of local attenuation values in object space $\bar{\mu}(\mathbf{r})$ as an input and yields for every location $\mathbf{r}$ the function of all contributions of $\bar{\mu}(\mathbf{r})$ in sinogram space $\bar{\mu}_{\mathrm{L},\mathbf{r}}(c,r)$. Figure 4.7 depicts $\bar{\mu}_{\mathrm{L},\mathbf{r}}(c,r)$ for a specific $\mathbf{r}$.

The simplest variant featuring ideal integration, no cross-talk and ideal temporal sampling reads:

$$\mathcal{P}_{\mathrm{P}}(\mathbf{r},\bar{\mu}(\mathbf{r})) = \bar{\mu}(\mathbf{r}) \cdot \sum_{c'=-\infty}^{+\infty} \sqcap\left(\frac{\beta - c'\Delta\beta}{\Delta\beta}\right) * \mathcal{N}_r^{(\beta_{\mathbf{r},\nu},\sigma^2_{\mathbf{r},\nu})}(\beta), \tag{4.11}$$

where $*$ denotes the convolution. $\mathcal{N}_r^{(\beta_{\mathbf{r},\nu},\sigma^2_{\mathbf{r},\nu})}(\beta)$ is the normally distributed tube profile projected onto the detector for reading r. Its mean value $\beta_{\mathbf{r},\nu}$ is the detector channel angle corresponding to the location $\mathbf{r}$ and the gantry angle ν and its standard deviation $\sigma_{\mathbf{r},\nu}$ is the standard deviation of the tube profile σ_{T} times a stretch factor determined by the pinhole projection model indicated in Fig. 4.6b. $\Delta\beta$ is the fan angle between two channels, $\sqcap(\beta)$ is the rectangle function of width 1, centered at $\beta = 0$. The fan beam geometry is illustrated in Fig. 1.16a.

For a source position $\mathbf{s}_\nu \in \mathbb{R}^2$ and a source-detector distance of d_{SD} we get the projected point location:

$$\mathbf{r}_{\mathrm{D},\nu} = \mathbf{s}_\nu + d_{\mathrm{SD}} \cdot \frac{(\mathbf{r} - \mathbf{s}_\nu)}{\|(\mathbf{r} - \mathbf{s}_\nu)\|_2}. \tag{4.12}$$

From this we can compute the corresponding channel angle $\beta_{\mathbf{r},\nu}$ with the rotated channel location $\mathbf{r}'_{\mathrm{D},\nu}$:

$$\mathbf{r}'_{\mathrm{D},\nu} = \mathbf{R}_{-\nu}\mathbf{r}_{\mathrm{D},\nu} + (d_{\mathrm{SD}}, 0)^T \tag{4.13}$$

$$\beta_{\mathbf{r},\nu} = \arctan_2(r'_{\mathrm{D},\nu,y}, r'_{\mathrm{D},\nu,x}) \tag{4.14}$$

with

$$\mathbf{r}'_{\mathrm{D},\nu} = (r'_{\mathrm{D},\nu,x}, r'_{\mathrm{D},\nu,y})^T \tag{4.15}$$

The function $\arctan_2$ is the well-known variation of the arctangent function for polar coordinate transforms and $\mathbf{R}_{-\nu}$ is the rotation matrix that rotates a point by $-\nu$.

The standard deviation $\sigma_{\mathbf{r},\nu,r}$ can be computed as follows:

$$\sigma_{\mathbf{r},\nu} = \frac{\|\mathbf{r}_{\mathrm{D},\nu} - \mathbf{r}\|_2}{\|\mathbf{s}_\nu - \mathbf{r}\|_2} \cdot \sigma_{\mathrm{T}} \tag{4.16}$$

Ray Contribution Masks

We use the point-based projection operator $\mathcal{P}_{\mathrm{P}}(\mathbf{r}, \bar{\mu}(\mathbf{r}))$ to calculate the contribution of a local measured value to its neighbors by sampling the projection ray that corresponds to the measured attenuation at $\hat{c}$, $\hat{r}$. A single point in the projection space approximately corresponds to a line in object space ($\hat{\mathbf{l}}_{\nu,\beta}(\alpha)$ in Fig. 1.16a). See Figs. 4.8a – 4.8c for examples on a simple phantom. We sample this line at distinct locations and use $\mathcal{P}_{\mathrm{P}}(\mathbf{r}, \bar{\mu}(\mathbf{r}))$ to quantify contributions of the projection line at $\hat{c}$, $\hat{r}$ to neighboring sinogram channels. The result of this operation is the RCM. We call the sampled locations $\hat{\mathbf{r}}_{\hat{c},\hat{r},k}$ with k indexing the line samples.

Using these definitions we compute the RCM $R_{\hat{c},\hat{r}}(c, r)$ as

$$R_{\hat{c},\hat{r}}(c, r) = \sum_k \mathcal{P}_{\mathrm{P}}\left(\hat{\mathbf{r}}_{\hat{c},\hat{r},k}, \bar{\mu}(\hat{\mathbf{r}}_{\hat{c},\hat{r},k})\right) \tag{4.17}$$

In order to reduce the RCM to the most dominant structures, we neglect all ray samples for which $\bar{\mu}(\mathbf{r})$ falls below a given fraction p_{S} of the maximum attenuation value along the sampled ray, so $\hat{\mathbf{r}}_{\hat{c},\hat{r},k}$ includes only the samples above the scaled maximum value. This percentage is an important filter parameter which is called *Structure Preservation Parameter* p_{s} consecutively. In practice, values in the range of $p_{\mathrm{s}} = 0.75$ to $p_{\mathrm{s}} = 0.95$ lead to best results.

The RCM drops very fast with respect to distance from the center position $(\hat{c}, \hat{r})$ so in practice, it can be limited to a neighborhood of 5 to 11 readings. We call this parameter $\Delta r_{\max}$. The size limitation in terms of channels can be determined by computing the outmost non-zero points of the integrated projections.

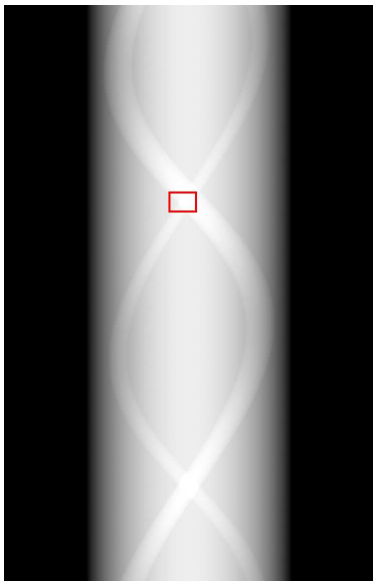

(a) Example sinogram (box indicates the magnified excerpt of Fig. (b)).

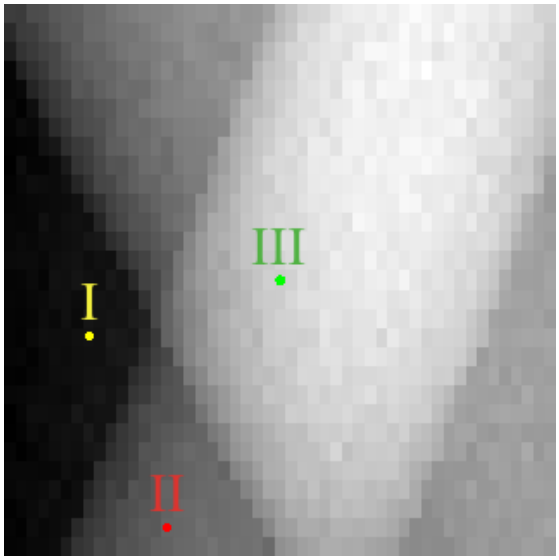

(b) Excerpt with marked sample measurements.

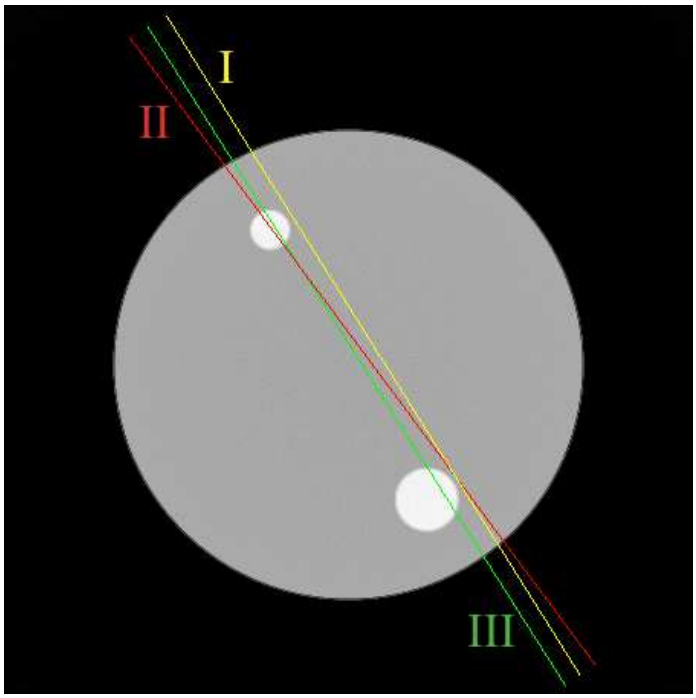

(c) Reconstructed slice with corresponding measurement lines.

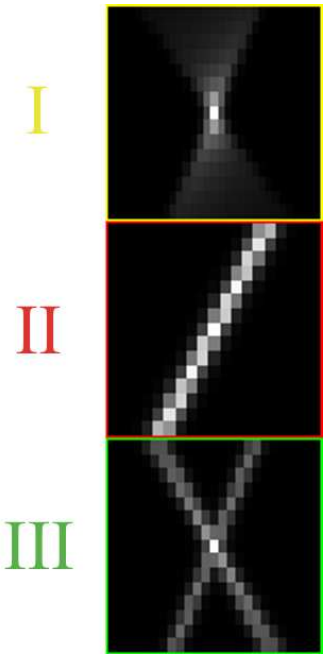

(d) RCMs.

Figure 4.8: Example for correspondences between projection and object space: (a) shows a sinogram of a simple phantom (Intensity window center (c): 5.25, width (w): 10.5, no unit), (b) shows a magnified excerpt with markers at sample locations, (c) shows the reconstructed slice (c: −250 HU, w: 1500 HU) with the ray lines in corresponding colors to the markers of Fig. (b) and Fig. (d) shows the RCMs for the measurement lines (Roman numerals indicate the correspondences).

Figure 4.8d shows an example of some RCMs for different rays and different local structures. Example I contains no specific dominant structures, the contributions of the water background are spread evenly on an hour-glass shape. Example II contains the small circle, which appears as a dominant structure, therefore the RCM consists mostly of the trajectory of this structure in the sinogram. The third example III contains two dominant structures at very different image locations. These appear as two trajectories in the RCM.

Structural Similarity

The RCM shape can be interpreted as follows: The value of $R_{\hat{c},\hat{r}}(c,r)$ contains the information on how much of the total attenuation measured at $(\hat{c},\hat{r})$ appears in the value measured at (c,r). Due to this property, the neighboring RCMs are very similar in regions where the dominant structures are very similar, so it can be used as a basis for the ISS filter kernel. For locations where local structures differ, the similarity between RCMs decreases and major contributions from other dominant structures may prevent strong smoothing in these directions. The averaging between these values has to be blocked. As the RCM is a measure for the local structure, it is perfectly suited to detect those structural changes. We can determine the structural similarity $s_{\hat{c},\hat{r}}(\hat{c}',\hat{r}')$ between neighboring measurement values at $(\hat{c},\hat{r})$ and $(\hat{c}',\hat{r}')$ by comparison of the RCMs at both locations.

The structural similarity $s_{\hat{c},\hat{r}}(\hat{c}',\hat{r}')$ can be calculated from the RCMs in various ways by employing any similarity or correlation measure on pairs of RCMs. The following variant describes a very simple approach using the sum of absolute differences as a dissimilarity measure:

$$\hat{s}_{\hat{c},\hat{r}}(\hat{c}',\hat{r}') = \sum_{\hat{c}''}\sum_{\hat{r}''}\{|R_{\hat{c},\hat{r}}(\hat{c}'',\hat{r}'') - R_{\hat{c}',\hat{r}'}(\hat{c}''-\hat{c}',\hat{r}''-\hat{r}')|\} \tag{4.18}$$

The expression $\hat{s}_{\hat{c},\hat{r}}(\hat{c}',\hat{r}')$ actually yields a non-normalized dissimilarity by computing the shifted difference of the two RCMs. We normalize this measure and convert it to a similarity measure by computing:

$$s_{\hat{c},\hat{r}}(\hat{c}',\hat{r}') = 1 - \frac{\hat{s}_{\hat{c},\hat{r}}(\hat{c}',\hat{r}')}{\sum_{\hat{c}'}\sum_{\hat{r}'}\hat{s}_{\hat{c},\hat{r}}(\hat{c}',\hat{r}')} \tag{4.19}$$

with $s_{\hat{c},\hat{r}}(\hat{c}',\hat{r}') \in [0,1]$, pairs of measurement values with a totally similar RCM-structure get an $s_{\hat{c},\hat{r}}(\hat{c}',\hat{r}')$-value of 1.

ISS Filter Calculation

With the similarities $s_{\hat{c},\hat{r}}(\hat{c}',\hat{r}')$ we can compute the final local filter $f_{\hat{c},\hat{r}}(\hat{c}',\hat{r}')$ by constructing a bilateral filter-type kernel using a spatial neighborhood filtering component and the structural neighborhood component of Eq. (4.19).

Note that it is theoretically possible to construct filter kernels with a range of more than one reading. However, this can make the filter prone to produce artifacts at high contrast objects since filtering over reading borders tends to cause minor inconsistencies in the projection data. Therefore we provide a kernel which performs

filtering only within one reading. It is a univariate Normal distribution with extends in channel direction:

$$\mathcal{N}^{(\sigma^2)}_{\hat{c},\hat{r}}(\hat{c}',\hat{r}') = \frac{1}{\sqrt{2\pi}\sigma} \cdot \exp\left\{\frac{(\hat{c}'-\hat{c})^2}{\sigma^2}\right\} \tag{4.20}$$

Its mean value is placed at the center position of the filter $\hat{c},\hat{r}$ and σ should be linked to $\Delta r_{\max}$ so that contributions beyond this range are negligible. Thus, only $\Delta r_{\max}$ steers the overall filter strength. The resulting local filter kernel is the normalized product of the spatial and structural similarity term

$$\tilde{f}_{\hat{c},\hat{r}}(\hat{c}',\hat{r}') = s_{\hat{c},\hat{r}}(\hat{c}',\hat{r}') \cdot \mathcal{N}^{(\sigma^2)}_{\hat{c},\hat{r}}(\hat{c}',\hat{r}'). \tag{4.21}$$

$$f_{\hat{c},\hat{r}}(\hat{c}',\hat{r}') = \frac{\tilde{f}_{\hat{c},\hat{r}}(\hat{c}',\hat{r}')}{||\tilde{f}_{\hat{c},\hat{r}}(\hat{c}',\hat{r}')||_2} \tag{4.22}$$

This approach fulfills the requirement stated above: Maximal smoothing between values with similar local structures according to their common attenuation and smoothing over values with different local structures is blocked. The structures are not estimated in the projection domain but from a projection model.

The normalized similarity masks $f_{\hat{c},\hat{r}}(\hat{c}',\hat{r}')$ for the sample locations shown in Fig. 4.8b are depicted in Fig. 4.9. These images demonstrate the basic properties of the filter: In homogeneous regions, the shape of the RCMs is similar and a high structural similarity causes strong smoothing into these directions. At borders with changing the local structure, no smoothing takes place and edges are preserved. This ensures strong noise reduction by an automatically steered averaging according to the similarity of the measured values.

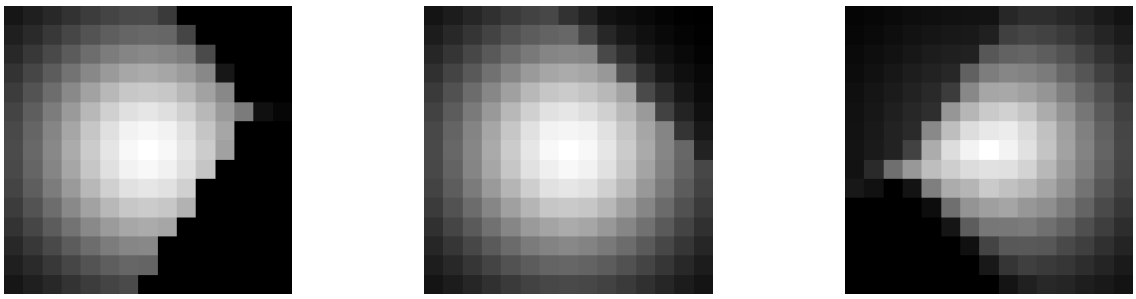

(a) I (b) II (c) III

Figure 4.9: Normalized RCM similarity masks for the examples given in Fig. 4.8. The Roman numerals indicate the correspondence with the markers in Fig. 4.8b and the lines in Fig. 4.8c. The center line corresponds to the shape of the filter kernels with a range of one reading.

Adaptive Filter Range

The RCM-similarity can also be used to perform a dynamic, homogeneity-driven range adaption. This measure is used to reduce the overall filter influence in regions

with large structural inhomogeneity or transitions between different dominating local structures. In practice, it has a positive influence on the overall image quality of the RCM filter results. We choose a very simple homogeneity adaption which incorporates the required properties. It scales the standard deviation σ of the spatial filter component defined in Eq. (4.20) with a homogeneity term. For the filter kernel of Eqs. (4.21) and (4.22) with a filter range of one reading and $\Delta r_{\max}$ channels, the scaling factor is defined as follows:

$$h_{\hat{c},\hat{r}} = \sum_{\hat{c}'=\hat{c}-\Delta r_{\max}/2}^{\hat{c}+\Delta r_{\max}/2} s_{\hat{c},\hat{r}}(\hat{c}',\hat{r}')/\Delta r_{\max}. \tag{4.23}$$

i. e. σ is replaced with $\sigma \cdot h_{\hat{c},\hat{r}}$. In case of total structural homogeneity in the neighborhood of $(\hat{c},\hat{r})$, $h_{\hat{c},\hat{r}} = 1$ and no size adaption is performed. With increasing inhomogeneity, $h_{\hat{c},\hat{r}}$ decreases and thus the filter range is decreased which reduces the overall filter strength. This can be combined with a noise model-driven filter range adaption.

4.3.2 Materials and Methods

Implementation Details

Our implementation of $\mathcal{P}_{\mathrm{P}}(\mathbf{r},\bar{\mu}(\mathbf{r}))$ features a pin-hole projection model and a numerical temporal integration for the sampling of the projection angles. The beam profile was assumed to follow a Normal distribution. The FWHM of the Normal distribution at the tube focus point was set to 0.9 mm in all evaluations. The used detector sizes were 678 or 736 channels and 1152 readings per rotation were acquired. In the measured data a detector quarter channel offset and an indirect fan-beam reconstruction was used. In simulations, no quarter offset was assumed and a direct fan-beam reconstruction was used. In most experiments, the pre-reconstruction and the final reconstruction both were performed with a Ram-Lak or a Shepp-Logan reconstruction kernel. Other kernel combinations are explicitly mentioned.

Optimization

Some essential optimizations have to be performed for a practical implementation of the algorithm. A naive realization of the formulas presented above would require a huge amount of computations. The resulting computation time would render the filtering impractical. Fortunately, the computation can be reformulated to exploit symmetries and enable a pre-computation of intermediate results that only depend on the system geometry and not on the imaged object. These computations have to be performed only once for a fixed scanner set-up and may be reused for each scan. They may include measurement effects like the temporal integration of projections during one reading.

The pre-computation makes use of the fact that the shape of all point-based forward projections does not depend on the absolute reading angle. The point-based analytic projections can be very expensive operations, so we want to ensure that as

little projections as possible are computed and that no projections have to be computed during the filtering phases. It is sufficient to compute all forward projections for a single reading. These forward projections can be stored and re-used for further filter computations as only the scale of the projections depends on the actual data whereas the shape is fully dependent on the scanner geometry. So the first step of the optimized algorithm is the pre-computation phase, where all sample locations on all rays of the X-ray fan for a fixed reading angle are determined. For each sample, the point-based forward projections Eq. (4.11) are computed for a neutral local attenuation value $\bar{\mu}(\mathbf{r})$ of one.

The filtering itself involves the following steps: First of all, a pre-reconstruction with a hard filter kernel has to be performed. It is used for the RCM computation of Eq. (4.17): One RCM corresponds to one sampled ray path. The ray path has to be rotated according to the reading angle, then the pre-reconstructed slice is interpolated at the according sample locations, the main contributions are identified and a weighted addition of the according pre-computed projection masks is performed. The interpolated values of $\bar{\mu}(\mathbf{r})$ are used as weights. The result of this operation is one RCM for each channel and reading which are held in memory for the next step.

The filter computation step of Eq. (4.21) can be carried out in a straight-forward fashion. The required similarity measures of Eqs. (4.18) and (4.19) can be computed on demand from the RCMs from the previous steps. A re-usage of similarity values computed earlier in the filter computation phase is unlikely to bring significant advantages as due to the storage and organization overhead.

The application of the filter is the final step. The filter changes for every sinogram location. This property leaves little room for high-level optimization, but the computational costs of these steps are negligible.

The overall complexity is dominated by the RCM computation. It scales linearly with the product channels $\times$ readings $\times$ samples per ray.

Phantoms and Experiments

Three different phantom set-ups were used for the performance evaluations (Tab. 4.3): The first one consists of a CT-scan of a high resolution phantom of aluminum insets in PMMA (Catphan HR[1]). It was used to assess noise and sharpness of filtered and standard reconstructions.

The second set-up involves in vivo CT-scans of live patients. In order to visually assess the influence of this filter on image data, we use three patient data sets acquired with a Siemens SOMATOM Definition (Siemens AG, Forchheim, Germany). All scans were conducted at 140 kVp tube voltage, 1.2 mm slice width, no flying focal spot. The integration time was set to 433 μs at a rotation time of 0.5 s. The selected tube currents were in the range of 55 mA to 80 mA.

Between the individual experiments the filter parameters were varied in order to assess their influence on noise suppression and sharpness compared to standard reconstructions. Homogeneity adaption was turned on in all cases. In some experiments, a Shepp-Logan kernel was used for pre- or final reconstruction instead of a

[1] Catphan 500, *http://www.phantomlab.com/catphan.html*, The Phantom Laboratory, Salem, NY, USA

Object	Type	Evaluated quantities
Catphan HR phantom	measured	MTF, noise, artifacts
Patient data	measured	Noise, image quality (visual)
Low contrast inset in water	simulated	MTF, noise

Table 4.3: Overview of conducted experiments.

Ram-Lak kernel. Here, the reconstruction quality for realistic application scenarios and the visual influence of filter parameters was inspected. The RCM filter results are compared to standard reconstructions using softened cosine kernels which lead to an approximately similar overall noise amplitude. The kernel used for these comparisons are special variants of the Cosine kernel and are defined in Eq. (1.9).

The third scenario uses simulated data. A scan of a cylindrical water phantom with a circular inset of varying densities was simulated with an analytic forward projector for four different contrasts between inset and water. For each contrast, 250 to 1000 scans were simulated and the filter was applied (the lowest contrasts required 500 resp. 1000 scans due to the low CNR). The edge between inset and water was used for an MTF estimation [Judy 76].

(a) Measured Catphan HR phantom.

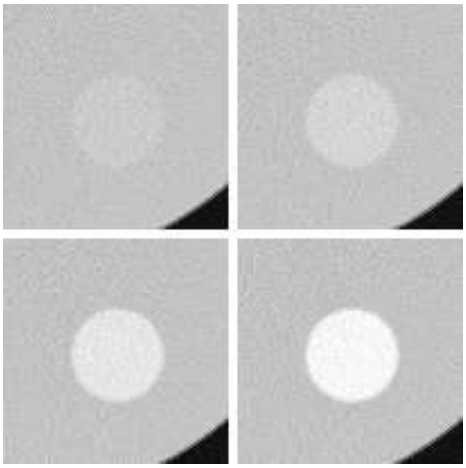

(b) Contrast insets in cylindrical water phantom.

Figure 4.10: Phantoms used for evaluation. Figure (a) shows the Catphan High Resolution phantom with aluminum insets in PMMA (c: 346 HU, w: 2751 HU). The distances between insets ranges from 1 lp/cm to 21 lp/cm. Figure (b) shows the four different contrast insets in a water phantom used for edge MTF evaluation (c: -387 HU, w: 1655 HU). The noise standard deviation is approx. 43 HU and the contrasts are 55 HU, 109 HU, 213 HU and 315 HU.

4.3.3 Evaluation and Results

High Resolution Phantom

Figure 4.11 shows the MTF estimates for the standard reconstruction and a filtered version. We can see only marginal changes in terms of relative contrast throughout the whole frequency range. This is due to the fact that the introduced filter clearly identifies the high-contrast structures throughout the whole sinogram and adapts the filters appropriately. No averaging takes place between components containing structure and background. In this case, the image sharpness is not affected and no additional reconstruction artifacts can be detected. The ISS filter manages to achieve a noise reduction of about 13.6 % from a standard deviation 10.3 HU without filter to 8.9 HU with filter. Due to its many small high-contrast inlays this phantom can be considered as a benchmark for robustness against reconstruction artifacts.

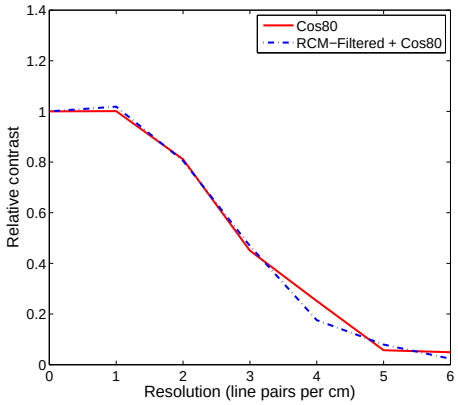

Figure 4.11: Relative contrast of a standard reconstruction between insets and background for various line resolutions. Cos80 indicates a cosine reconstruction kernel with a cut-off frequency at 80 % of the detector Nyquist frequency.

Patient Data

Figures 4.12 and 4.13 show comparisons between standard reconstructions and RCM-filtered reconstructions of patient scans. Although the estimated noise amplitudes are approximately similar in Figs. 4.12b and 4.12c resp. 4.13a and 4.13b, the ISS filter causes visibly less blurring, especially at edges with higher CNR and high frequency components, for instance, the organ tissue textures are preserved better. At very high CNR edges, like the transition between air and tissue, the ISS filter can cause a minor amplification of the edge strength. The noise shaping characteristics are also very different: The cosine kernel attenuates high frequency noise components very strongly whereas low frequency noise passes the filter, consequently the noise grains are rather big and smooth. The noise in the ISS filter result (Fig. 4.12c) has a different frequency distribution which resembles the original noise structure more closely. The noise reduction is more homogeneous throughout the whole frequency range.

The noise shaping characteristics can be influenced by altering the filter parameters. In general, the noise shaping characteristics of ISS filtering are less intuitively linked to the filter parameters than for standard reconstruction kernels. However, a desired specific noise shaping characteristic can be achieved by adapting the filter kernel of the final reconstruction of the ISS filter result. For instance, a smoother post-reconstruction kernel leads to stronger smoothing of the ISS filter result. A smoother pre-reconstruction filter also influences the ISS filter. This property is visualized in Fig. 4.13d. Here we investigate the influence of the pre-reconstruction kernel. We used a Shepp-Logan kernel instead of a Ram-Lak kernel for the pre-reconstruction. This leads to a visible decrease in sharpness and noise. The amount of noise reduction of approx. 13 % corresponds to a standard reconstruction with a Cos525 kernel (Fig. 4.13c). This indicates that the pre-reconstruction kernel has a clearly visible influence on the ISS filtering result and can be used to influence the filter properties of the RCM filter.

Noise Reduction and MTF

This evaluation addresses the frequency transfer behavior of the filter. This is done by measuring the image MTF of a standard Ram-Lak filtered FBP reconstruction and a ISS filtered reconstruction on an edge phantom. This evaluation requires a very huge number of repetitions to eliminate the influence of noise on the MTF measurement. We chose 250 to 1000 repetitions depending on the examined CNR level.

Figure 4.14 shows the resulting azimuthal edge MTFs for four different contrasts. The noise standard deviations in the Ram-Lak filtered original and the processed versions are given in Tab. 4.4. For the 55 HU low contrast case we can observe a slight reduction of the MTF in the mid-frequency range, in the 109 HU case, the MTFs are very similar between original and filtered case. The two higher contrast cases show a slightly edge enhancing property of the filter at higher frequencies whereas low frequencies are attenuated slightly. This reveals the frequency transmission behavior of the projection filter when it is fully adapted to the edge shape in the sinogram. This causes the edge to be visibly enhanced in the filtered sinogram. The total noise reduction achieved for these examples is also shown in Tab. 4.4. It shows the standard deviation of the noise for a Ram-Lak reconstruction and the RCM filtered reconstruction. In this simplified scenario a very strong noise reduction of over 80 % can be achieved. More dominant structures slightly reduce the total noise reduction. This can be seen in the standard deviations of the 109 HU to 315 HU cases. In the 55 HU case, we used a cosine reconstruction kernel for the pre-reconstruction, therefore the noise in the original images is already slightly lower. However, the relative noise reduction agrees with the other cases.

Complexity, Run-Time and Performance

All computations were carried out on a standard desktop computer equipped with an Intel Core i7 860 CPU at 2.8 GHz and 8 GB of DDR3 RAM. The filter computation consists of three phases: The initialization of the forward projections, the RCM computation and the filter generation and application. All these steps depend on the desired filter size in readings which was kept constant at 5 throughout all experiments.

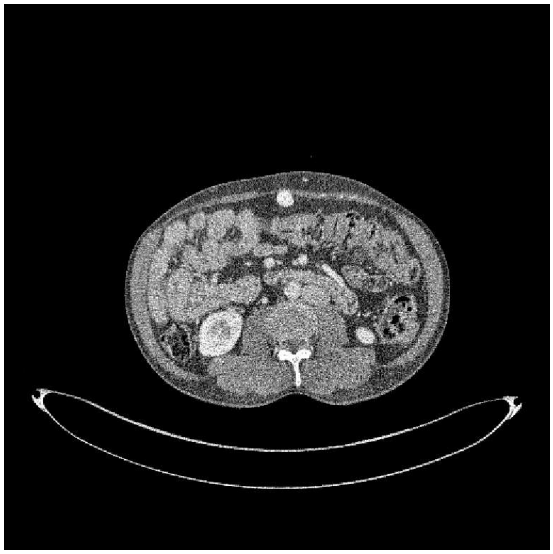

(a) Reconstructed slice.

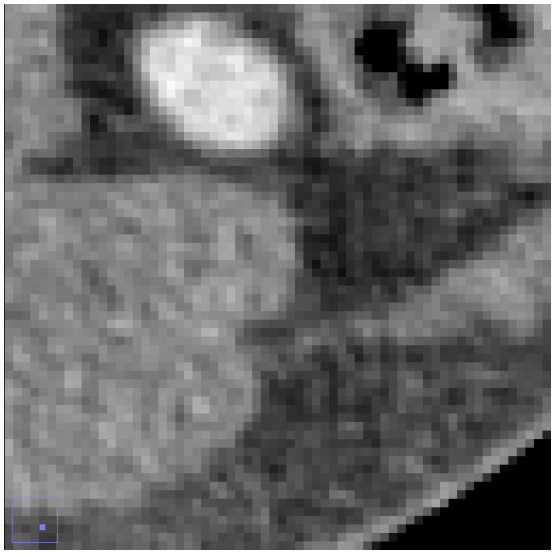

(b) Cos625 reconstruction.

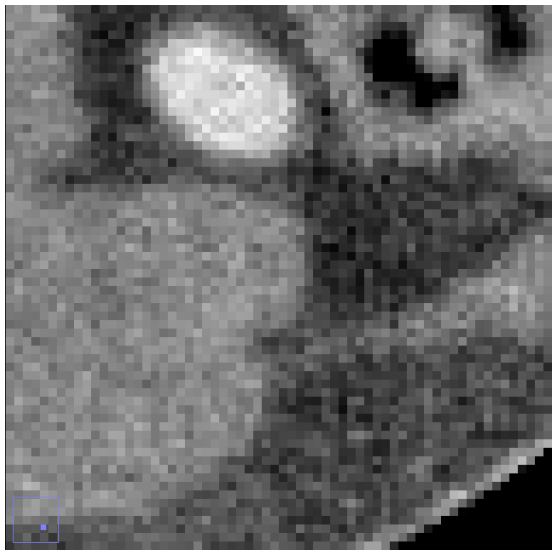

(c) RCM result.

Figure 4.12: Filter results: (a) Reconstructed slice of the data-set, (b) magnified excerpt (Cos63 kernel) and (c) result of the RCM filter (9×9 RCM size, 0.225 smoothing, structure preservation 0.9, homogeneity adaption on). The water scaling was omitted in these tests, so no intensity windows are given. Original images are a courtesy of Prof. Dr. Andreas H. Mahnken, RWTH Aachen, Germany.

Contrast	**Std. dev. original**	**Std. dev. filtered**	**Noise Reduction**
55 HU	27.7 HU	3.87 HU	86.0 %
109 HU	33.2 HU	5.75 HU	82.7 %
213 HU	33.2 HU	6.40 HU	80.7 %
315 HU	33.2 HU	6.54 HU	80.3 %

Table 4.4: Estimated noise reduction for various contrasts.

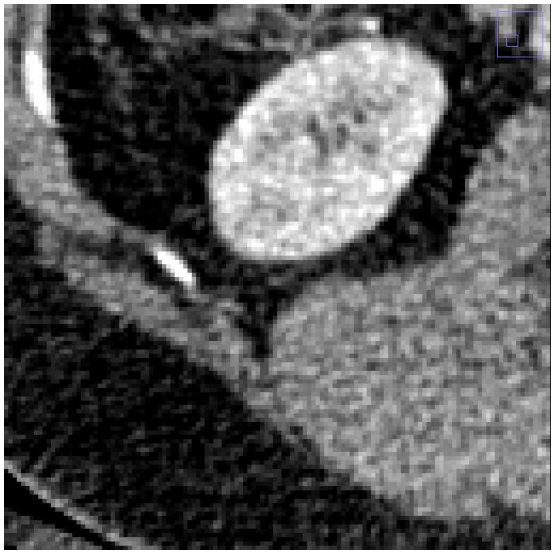

(a) Cos575 reconstruction.

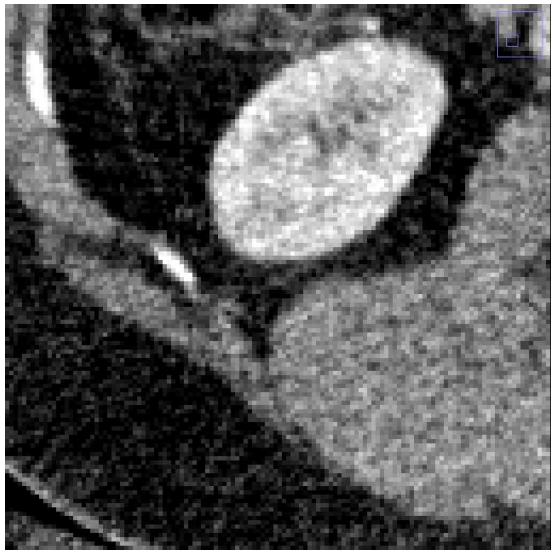

(b) RCM result.

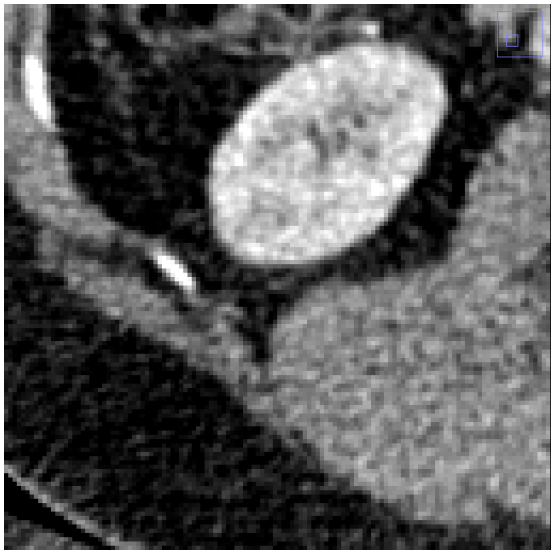

(c) Cos525 reconstruction.

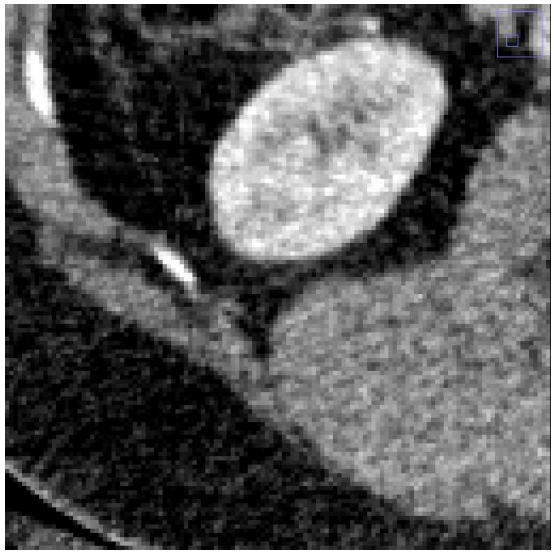

(d) RCM with Shepp-Logan pre-reconstruction.

Figure 4.13: Filter results for third example: (a) Magnified excerpt (Cos575 kernel), and (b) result of the RCM filter (9×9 RCM size, 0.5 smoothing, structure preservation 0.8, homogeneity adaption on), (c) Cos625 kernel result and (d) result with Shepp-Logan filtered pre-reconstruction. Original images are a courtesy of Prof. Dr. Andreas H. Mahnken, RWTH Aachen, Germany.

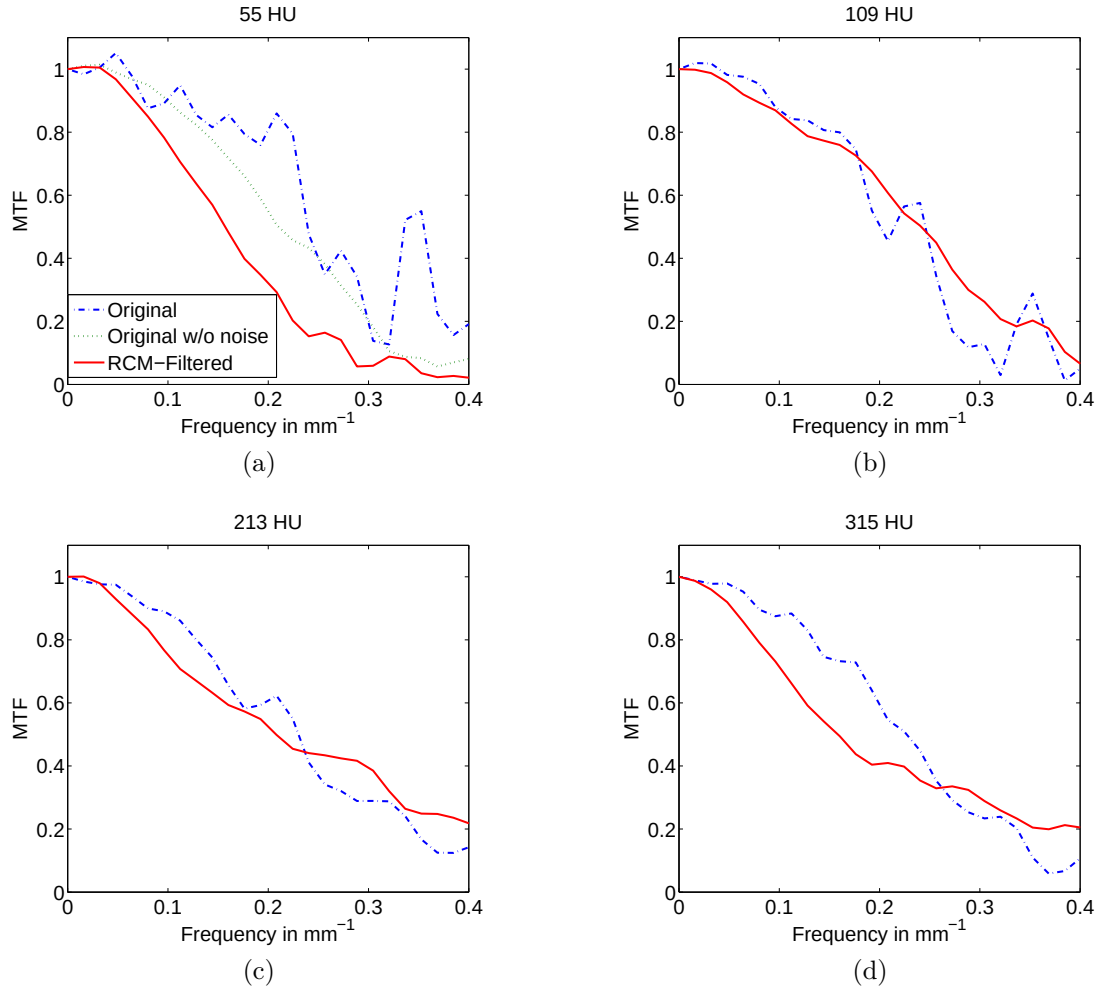

Figure 4.14: MTF comparisons for varying contrast strengths of insets. For the 55 HU example, 1000 realizations were simulated and the MTF estimate from a noise-free unfiltered realization is also shown. For the 109 HU case 500 realizations and for the other examples 250 realizations each were simulated. The estimates from the noise-free realization are omitted for the last three cases as there is only a minor influence of the noise for this number of realizations.

The time for the pre-computation of the forward projections depends on the number of detector channels, the ray sampling distance and the complexity of the point-based forward projector model. Unlike the following two phases it can be pre-computed for a given geometry as it does not depend on the imaged object. So the computation time of this phase does not add to the filter time. Our reference implementation with 736 detector channels and at sample distance of exactly one pixel width took about one minute for a $\Delta r_{\max}$-value of 9. The RCM computation depends on the number of channels, readings, ray sampling distance and $\Delta r_{\max}$. This phase took our reference implementation between 20 seconds to 1 minute, whereas the filter generation and application phase depends only on the number of channels and readings and required about two to three seconds on average. This leads to a filter times of approx. 1 minute per slice. Additionally the pre-reconstruction and the reconstruction of the have to be carried out. The computation time from sinogram to reconstructed and filtered slice totals to about 2 minutes per slice. The memory consumption is dominated by the size of the pre-computed point-based projection table and the RCM table. Not all tables have to reside in memory completely. Since the sizes are usually not critical on current hardware, we did no optimizations regarding this issue. It our set-up the pre-computed table size is approx. 100 MB, the peak memory consumption is about 4 to 8 GB for eight parallel threads.

4.4 Conclusions

The introduced noise-reduction technique for Dual Energy CT data showed the potential of reducing image noise by about 20 to 30% in subjective tests on real CT-images of various body regions. The quantitative accuracy was evaluated in an energy calibration application on phantom data. It revealed a tolerable accuracy loss of approx. 1 to 2% which is in the range of the overall accuracy of a CT system. The noise standard deviation could be reduced by approx. 30% for this quantitative CT application. A CNR test for small, low-contrast leasions yielded a CNR-gain ranging from 10% to over 100% depending on noise level, tube voltage setting and tissue contrast. The CNR values of the original image could be reproduced with 30% up to 70% less primary photons needed. This is directly related to an accordingly reduced radiation dose. These results demonstrate the possibility to perform a DECT scan at the same dose level as a standard CT scan. This is an important step in the clinical relevance of DECT applications.

The RCM-based ISS filter presented in the second part of the chapter is a novel approach to structure-preserving spatial filtering in projection data. We showed that this approach can detect and preserve structures in the projection domain while making use of the good contrast in the reconstructed data. The filter properties were assessed on measured and simulated phantom data as well as measured patient data. The patient data tests showed that image sharpness is superior to a standard reconstruction with the same total noise. The image MTF and high-frequency texture is well preserved even for low contrasts. The noise reduction in a simple edge phantom case exceeded 80 %, in scenarios with complex structure, a noise reduction of approx. 15 % is estimated for similarly sharp results. We also demonstrated that the filter can deal with structures that are prone to cause reconstruction artifacts.

The modulation transfer behavior of the filter was evaluated on simulated phantom data. The filter MTF is contrast dependent. For small contrasts around 50 HU, a reduction of the mid-frequencies can be observed, for higher contrasts it follows the original MTF closely and tends to enhance higher frequencies and attenuate low- and mid-frequencies in the reconstructed image.

Chapter 5

Summary and Outlook

The contributions presented in this work cover the full spectrum of Quantitative CT areas and can be divided into three main topics: Simulation tools for spectral signal acquisition were introduced in Chapter 2, Chapter 3 was dedicated to algorithms that compute quantitative measures from spectral CT data and signal enhancement was discussed in Chapter 4. In this chapter, we sum up all the findings and results of this work and give an outlook into possible further research directions for each part.

The first part focused on data acquisition methods for Quantitative CT called spectral detection. New look-up table-based simulation approaches were introduced that support very efficient simulations of full CT scans. The key contribution here is the possibility of simulating the full CT measurement process on a standard workstation within hours. The level of detail of a full-scale Monte Carlo simulation was reached and simulation results were verified by comparison with measured data from prototype detector systems, measuring stations and real-life CT systems. Simulation concepts for two different systems were presented: Integrating scintillation detectors and counting semiconductor detectors. The basic principle of both concepts is the identification of basic logical or physical steps in the detection process and defining appropriate interfaces between these steps. Then, each step is either modeled analytically or a huge number of possible random events occurring within the step is pre-computed and stored in a look-up table. The simulation cascades these steps by processing each step for all occurring events and processes the result data of an individual step so that it matches the defined interface between the process steps.

For integrating scintillators these steps are particle interaction in the scintillator crystal, light transport and electronics modeling. A deviation of 3.68 % was determined in a comparision between simulated and measured image MTF with a slice image of a high resolution test phantom. The 2-D detector NPS of a flat field image deviated by 3.06 % on average between a full scale MC simulation and the look-up table based approach. For full scan simulations, the computation time of the look-up table-based approach was found to be approximately 200 times faster than a classical MC approach. A comparison with the detector NPS in phi-direction acquired in a measuring station and a standard CT gantry showed an average deviation of 5.23 %.

For counting semiconductors, particle interaction in the semiconductor, pulse generation, photon counts extraction and A/D conversion were simulated. A full single-slice scan of a 40 cm water phantom takes approximately 8 h on a workstation

equipped with 4 × 2 AMD 885 Opteron cores at 2.6 MHz and 16 GB of RAM for a detector with 2475 detector pixels, 1600 readings at a reading time of 1ms using a sampling time of 2 ns. Comparisons with measured MTFs and DQEs generally show a good agreement with a slight tendency of underestimating the measurement noise and sharpness. The non-linear detector response of such a system could be reproduced for different energy thresholds and flux levels. Additionally, several characteristics were simulated that could not be measured directly, including electrode signal excerpts for various input signals, the energy transfer probability map for a given detector layout or linearity measures for different comparators. The linearity and signal analysis clearly shows the need for sophisticated discriminators and linearity corrections in order to deal with the full range of X-ray flux seen in medical CT scans. The results for both simulation approaches demonstrate that the real system behavior is modeled with a similar accuracy delivered by a full-scale Monte Carlo simulation. The higher efficiency makes a detailed optimization of design parameters possible.

Chapter 2 also gave a short overview on recent publications on counting semiconductor detectors. First prototype systems for medical detectors of the type are introduced and first evaluations of the designs are given. This is a clear indication that this topic is under investigation by several research groups and companies. However, several design problems and material issues are currently unsolved, so commercial systems are not yet available for medical CT and up to now, no precise prognosis can be made, whether this might change in the near future.

In terms of possible future research directions of simulation concepts, our look-up table-based simulation approach may, for instance, be extended to other spectral detection technologies. As mentioned in Sec. 2.2.1, the design of an optical counting detector using avalanche photodiodes can be evaluated with a hybrid simulation approach of the optical integrating and counting semiconductor simulations with few additional simulation stages. With several adaptions, this simulation concept can as well be used for the evaluation of other X-ray detection concepts apart from medical CT. An overview on the possible future directions of CT system design is for instance given in [Wang 08].

Chapter 3 aims at the processing of spectral data. Basic principles of QCT algorithms and Basis Material Composition as a standard QCT tool were explained. Then a novel, unified framework for QCT applications was introduced: the Local Spectral Weighting Function and Local Spectral Reconstruction. The LWF establishes the link between the spectral attenuation coefficient of a material and the effective attenuation value measured by a CT system. We have expressed the CT measurement and reconstruction process in terms of the LWF and introduced an algorithm for its computation. It is called Local Spectral Reconstruction algorithm, an iterative reconstruction scheme which uses forward and backward projectors, system energy weightings and BMD. It yields the LWF and the spatial distribution of spectral attenuation coefficients. Its application to several QCT topics was demonstrated: A quantitative beam-hardening correction was performed on scans of a cylindrical water phantom and a simulated thorax phantom. The thorax phantom was also used to demonstrate energy calibration. The suggested LSR iteration scheme uses LWF supported image-based BMD, so estimates of basis material coefficients can be directly extracted from the LSR iterations. Finally, a proof-of-concept for a method called

direct material identification was shown. This application allows to identify given materials or tissues directly in the CT data.

The precision and accuracy of the LSR algorithm were evaluated on simulated ground truth data. This evaluation showed a fast convergence with one to two iterations leading to a sufficient accuracy in most applications. For more iterations, however, a decrease in precision was found with increasing number of iterations, so no additional iterations should be performed when the desired level of accuracy is reached.

The next step in establishing LSR requires a clinical evaluation of a selected number of the proposed applications. The LSR concept is very fundamental as it offers a basic description of spectral detection and reconstruction. According to this property it is possible to formulate and evaluate other QCT applications in terms of the LSR framework that we did not cover in this work.

Chapter 4 introduced two algorithms for improving dose efficiency of multi-spectral CT. The first one is a value-based post-reconstruction method for improving multi-energy data. It uses a gradient ascent procedure on a joint probability estimates from two or more reconstructed multi-energy data sets to derive noise-reduced values. This method may be combined with frequency-based noise reduction techniques. We have demonstrated that only 30 % to 70 % of primary photons were required to achieve similar CNR values depending on the system settings and detection scenario. This number quantifies the dose reduction potential in Dual Energy scans, as the number of primary photons is directly linked to patient dose.

The capability of dose reduction for QCT applications was demonstrated on an energy calibration scenario. Here, a 30 % reduction of the noise level in the energy calibrated image was possible while the accuracy deviations stayed below the approximate system precision of 1 %. A subjective evaluation revealed a noise reduction potential of 20 % to 30 % without an impairment of the visibility of diagnostically relevant stuctures.

A further research direction for this topic was already indicated in Sect. 4.2: Here, we have outlined some possible strategies to efficiently combine this technique with adaptive frequency-based image filters. The combination of these methods is a promising approach to exploit the full dose saving potential for low-dose QCT applications. Consequently the next step is the evaluation of the combined approach for various QCT applications in order to find suited applications for low-dose QCT.

In the second part of Chapter 4 we presented a new concept for spatial filtering in the projection domain. It is called Iterative Structural Sinogram filtering using Ray Contribution Masks. This filter uses a pre-reconstructed image for deriving structural information in the projection domain. It merges the benefits of image-based filters (high contrast) and projection-based filters (simple noise properties). The local structural information is gathered by computing the so called Ray Contribution Mask. These masks offer many possibilities to construct projection-domain filter kernels that incorporate various desired properties like range- or noise adaption. We demonstrated this potential with an adapted version of the well-known concept of bilateral filtering. We replaced the photometric similarity term of traditional bilateral filters with an RCM-driven structural similarity term. The properties of this new filter type were thoroughly evaluated on simulated and measured phantom and patient data

in terms of noise reduction potential, MTF properties, artifacts and visual image quality. We observed a very different noise transfer behavior compared to traditional reconstruction-kernel based filtering. We demonstrated that this filter type can deal well with image artifacts and has noise reduction potential of at least 15 % on real patient scans. The filter MTF is contrast dependent and shows a tendency to amplify high frequencies whereas the MTF in the low- and mid-frequency range is slightly attenuated.

In summary, we expect that Quantitative CT will be a major research topic in the following years. Commercial clinical applications are not yet widespread but according to recent publications, all major CT manufacturers pursue solutions to cover this market. This applies to multi-spectral detection technologies and algorithmic QCT solutions in equal measure. In this work, we offered novel methods to enhance hardware concepts, reconstruct spectral data and improve diagnostic quality of QCT applications. We showed promising new applications and put existing ones in a common unified framework called Local Spectral Reconstruction. Although the basic ideas of QCT are almost as old as CT itself, its clinical relevance has just started to become important with the availability of suited CT scanners. Medical CT scanners capable of Dual Source spectral measurements have been available for approximately five years. With an increasing variety of spectrally resolving systems, the demand of new clinical QCT applications is likely to grow. With the LSR framework we provide a fundament on which new QCT applications may be developed and existing ones can be improved.

List of Figures

1.1 Third generation CT layout with rotating X-ray source and a single-row detector. The arrows annotated with (x, y, z) indicate the world coordinate system and the (ϕ, z)-arrows indicate the detector coordinate system. The symbol $\odot$ indicates an arrow pointing perpendicularly outwards the paper or display plain towards the reader. 3

1.2 Tube model and wedge filter. 4

1.3 Schematic illustration of an X-ray tube with single FFS. The two dots on the anode represent the alternating focal spot positions. The deflection coils force the electron beam to alternate between to trajectories indicated by the hatched and solid line. 5

1.4 Tube spectra with and without pre-filtering. Tube spectra generated with *drasim* (by Karl Stierstorfer, Siemens AG, Forchheim). The spectral attenuation coefficients were taken from the XCOM database of photon cross sections [Berg 98]. 6

1.5 Spectral overlap without and with tin filter (data from *drasim* by Karl Stierstorfer, Siemens AG, Forchheim). The intensities are displayed in arbitrary units (a. u.). 7

1.6 Sample output signals for ideal energy integration and ideal photon counting for synthetic input signal of randomly distributed interaction events at different energies. 9

1.7 Scintillation detectors. 10

1.8 Detector responsivity $D(E)$ for a 1.4 mm Gd_2O_2S scintillator CT detector [Heis 08]. This is the relative detector output signal strength for a detected quantum of given energy. 11

1.9 Basic layout and working principle of a directly converting semiconductor detector. 12

1.10 Output signals for two different Gaussian impulse responses with FWHM 10 ns and 50 ns. In the 10 ns signal most of the pulses remain distinguished and their locations and pulse heights can be recovered by a suitable discriminator. The 50 ns signal does not show this property, so it is only suited for energy integrating detection. The average frequency of events in the input signal is 50 MHz. 12

1.11 Concept of Dual Source CT. 14

1.12 Concept of a dual layer detector. 14

1.13 Spectral sensitivity example for a counting semiconductor detector with thresholds set to 5 keV and 60 keV. Due to several effects like cross talk, escape photons and signal pile-up, the spectral separation is reduced by a considerable overlap of the sensitivity curves. This example was generated using *SimSD* [Bald 09]. 15
1.14 Mass attenuation function of water and its contributions. Data taken from XCOM database [Berg 98]. 17
1.15 Mass attenuation function and its two major components in the CT energy range for various elements. Data taken from XCOM database [Berg 98]. 18
1.16 Notation for fan- and parallel-beam geometries. 19
1.17 Schematics of an X-ray attenuation measurement. 20
1.18 Left: Slice image of a clock phantom. The attenuation coefficients at 64 keV are gray-coded (intensity window center (c): $0.016\,\mathrm{mm}^{-1}$, width (w): $0.032\,\mathrm{mm}^{-1}$). Middle: Measured intensities $I_{\theta,t}$ for mono-energetic radiation at 64 keV (arbitrary units). Right: Corresponding sinogram of attenuation values (arbitrary units). The gantry rotation angle θ (ordinate direction) covers one full rotation, the detector channels are arranged on the horizontal axis. 20
1.19 Example illustration of the indirect fan-beam FBP reconstruction steps. 22
1.20 Reconstruction kernels for parallel-beam FBP. 24
1.21 Beam hardening example: (a) A simple phantom set-up consisting of water (gray), bone (white) and air (black). (b) Reconstruction of the phantom with visible beam hardening artifacts. We observe a superposition of the typical cupping artifact caused by the patient water background and the funnel-shaped artifact between strong bone absorbers. 25
1.22 MTF computation from a point spread function. 27
1.23 MTF computation from an edge spread function: Figure (a) shows an example edge image, (b) is the corresponding edge spread function extracted perpendicularly to the edge direction and (c) is the corresponding 1-D MTF. 27

2.1 Signal generation in scintillation detectors. 34
2.2 Detection steps and interfaces for integrating scintillation detectors. . 34
2.3 Signal flow diagrams for detection- and complete CT scan simulation. 35
2.4 (a) Interaction locations of 2500 randomly picked X-ray photon events (100 keV); (b) and (c) show excerpts of the histogram of energy deposition within scintillator voxels for homogeneous irradiation of center pixel with mono-energetic X-ray photons. Central slice in z-direction is shown. (b) mono-energetic 25 keV photons, (c) mono-energetic 100 keV photons. 37
2.5 Optical photon distribution-LUT example and comparisons between voxel positions 38

2.6 (a) Image-MTF comparison; (b) detector NPS comparison (profile of 2D-NPS along diagonal of 1st quadrant) between proposed simulation and full scale Monte-Carlo simulation; (c) and (d) NPS comparison between simulation and different measurements in measuring station and CT gantry. Measurements were conducted by Daniel Niederlöhner, Siemens Healthcare, Forchheim, Germany. 41
2.7 Detection steps and interfaces for counting semiconductor detectors. . 44
2.8 Pulse sample locations of a standard PulseLUT. Locations outside center pixel denote induced pulses by interactions in neighboring pixels. Color coded locations correspond to pulses plotted in Figs. 2.9 and 2.10. Color codes do not indicate a correspondence between Figs. (a) and (b). The red coordinate axis indicate the LUT-internally used detector pixel (x, y, z)-coordinate system also used in Figs. 2.9 and 2.10. 46
2.9 Example pulses for pulse locations marked in top view of Fig. 2.8. The colors of bullets marking the sample locations in Fig. 2.8a and function plots are matched. 46
2.10 Example pulses for pulse locations marked in side view of Fig. 2.8. The colors of bullets marking the sample locations in Fig. 2.8b and function plots are matched. 47
2.11 Measured relation between pulse amplitude and charge. Hatched line indicates ideal linear relationship. Slight deviations from the ideal line can be observed for low charges. Data from Daniel Niederlöhner, Siemens Healthcare, Forchheim, Germany. 48
2.12 Basic model of the simulation signal flow. 49
2.13 Comparison of measured and simulated MTF estimate. The fluorescence photons yield a crosstalk-like behavior which results in a slightly decreased MTF. 51
2.14 Comparison of measured and simulated DQE estimate. 51
2.15 Discretized 140 kVp input spectra for full, half and 10% CT flux with an energy bin width of 5 keV. 52
2.16 Resulting detector signals for spectra of Fig. 2.15. 53
2.17 Count rate behavior of rising edge discriminator for various thresholds and flux levels. 54
2.18 Simulated and measured linearity for two thresholds at 30 and 60 keV. 55
2.19 Energy transfer probability for X-ray photon of energy E and thresholds corresponding to energies E'. (a): Small pixels ($0.05\,\mathrm{mm}^2$), (b): large pixels ($0.20\,\mathrm{mm}^2$), (c): difference image. Intensity windows are for left and center image: Center 0.025, width: 0.05; Right image: Center 0, width: 0.02. The values reflect detection probabilities. . . . 56

3.1 System Weighting Functions $w_1(E)$,$w_2(E)$ according to Eq. (3.1) for the 80 kV and 140 kV tube spectra in Fig. 1.5a and the detector responsivity $D(E)$ in Fig. 1.8. The two weighting functions reflect a common Dual Energy measurement case, often referred to as a Dual-kVp CT measurement. 65

3.2 The LSR procedure is a two-phase update process, starting with the SWF as an initial estimation of the LWF, updating $\mu^{(1)}(E, \mathbf{r})$, updating $\Omega_j^{(1)}(E, \mathbf{r})$, updating $\mu^{(2)}(E, \mathbf{r})$, etc. After S steps we obtain an estimate for both the LWF and the object attenuation coefficient. Image taken from [Heis 09]. 69
3.3 Thorax phantom set-up used as set-up D and E in Tab. 3.1. The roman number annotations indicate specific body materials listed in Tab. 3.2. The spectral attenuation coefficient $\mu(E, \mathbf{r})$ is provided for each material type according to the body compositions in the ICRU46 report. At regions XV to XVII, set-up E contains blood with varying iodine contrast agent concentrations, whereas set-up D substitutes the three regions by the standard blood parametrization XIV. 73
3.4 CT image of the upper abdomen phantom and location of the sample points for the LWF plots of Fig. 3.5. 75
3.5 Samples of the local spectral weighting function within the thorax phantom. 75
3.6 Beam hardening correction result after first iteration compared to original and ground truth attenuation values. The higher values at the border of the phantom are caused by the plastic casing of the water phantom. 77
3.7 Absolute error for average soft tissue attenuation values after energy calibration with 80 kV target weighting. 78
3.8 Relative error for energy calibration with 80 kV base and target weighting (negative values indicate over-estimation). The tissue classes are described in Tab. 3.2 and illustrated in Fig. 3.3. 79
3.9 Relative error for energy calibration from 140 kV base to mono-energetic 511 keV target weighting (negative values indicate over-estimation). . 79
3.10 Relative errors for energy calibration of 80 kV input data to target spectra from 60 kV to 140 kV and a mono-energetic 141 keV spectrum. 80
3.11 Absolute error for blood and iodine densities in blood-iodine mixtures estimated with LSR. 80
3.12 (a) 80 kV input image (attenuation values $\bar{\mu}(\mathbf{r})$, center: $0.220\,\mathrm{mm}^{-1}$, width: $0.012\,\mathrm{mm}^{-1}$); (b) Color-coded identification result. Blue: skeletal muscle, red: blood, green: liver, yellow: average soft tissue 82

4.1 Examples for the gradient ascent procedure with $\bar{\mu}_1(\mathbf{r}) = 0.0187\,\mathrm{mm}^{-1}$ and $\bar{\mu}_2(\mathbf{r}) = 0.0232\,\mathrm{mm}^{-1}$. Arrows indicate the gradient direction, the start point is located at the base of the arrows. 89
4.2 (a) Thorax phantom (with a small water cylinder at the top-left corner used for water scaling); (b) Low contrast lesions for CNR evaluation. (c) Lesion example at 80 kVp with 14 HU contrast and 70000 primary photons (intensity window center: 45 HU, width: 35 HU). 92
4.3 CNR test results for different contrasts at 80 kVp and 140 kVp tube voltage and selected noise reduction parameters. Contrasts and bandwidths given in mm^{-1} (integrated attenuation values). 94

4.4 Filter input and result for head image example. (a) Original 80 kVp image, (b) processed 80 kVp image, original 140 kVp image, filtered 140 kVp image. Original images are a courtesy of Prof. Dr. Andreas H. Mahnken, RWTH Aachen. 95

4.5 Filter input and result for foot image example (from left to right): Top row: Original 80 kVp image including evaluated region of interest, processed 80 kVp image (80 kVp, HU-window: center -12; width 108). Bottom row: original 140 kVp image, processed 140 kVp image (140 kVp, HU-window: center 1; width 131). The black outline in Figs. (c) and (d) marks the homogeneous region in which the noise estimate was computed. Original images are a courtesy of Prof. Dr. Andreas H. Mahnken, RWTH Aachen. 96

4.6 Illustration of the working principle of the projection operator $\mathcal{P}_{\mathrm{P}}(\mathbf{r}, \bar{\mu}(\mathbf{r}))$. Figure (a) shows a Normally distributed tube-profile, (b) illustrates the schematics of projection process and (c) is the according sampled projected tube-profile $\bar{\mu}_{\mathrm{L}}(c, r_1)$ for fixed reading r_1. A complete result of $\mathcal{P}_{\mathrm{P}}(\mathbf{r}, \bar{\mu}(\mathbf{r}))$ is displayed in Fig. 4.7. 99

4.7 Result of point-based projection operator for all channels and readings $\bar{\mu}_{\mathrm{L},\mathbf{r}}(c, r)$ at a fixed location $\mathbf{r}$ (scale: arbitrary units). For visualization purposes, an extremely large X-ray focus of 9 mm FWHM was used. . 100

4.8 Example for correspondences between projection and object space: (a) shows a sinogram of a simple phantom (Intensity window center (c): 5.25, width (w): 10.5, no unit), (b) shows a magnified excerpt with markers at sample locations, (c) shows the reconstructed slice (c: −250 HU, w: 1500 HU) with the ray lines in corresponding colors to the markers of Fig. (b) and Fig. (d) shows the RCMs for the measurement lines (Roman numerals indicate the correspondences). 102

4.9 Normalized RCM similarity masks for the examples given in Fig. 4.8. The Roman numerals indicate the correspondence with the markers in Fig. 4.8b and the lines in Fig. 4.8c. The center line corresponds to the shape of the filter kernels with a range of one reading. 104

4.10 Phantoms used for evaluation. Figure (a) shows the Catphan High Resolution phantom with aluminum insets in PMMA (c: 346 HU, w: 2751 HU). The distances between insets ranges from 1 lp/cm to 21 lp/cm. Figure (b) shows the four different contrast insets in a water phantom used for edge MTF evaluation (c: -387 HU, w: 1655 HU). The noise standard deviation is approx. 43 HU and the contrasts are 55 HU, 109 HU, 213 HU and 315 HU. 107

4.11 Relative contrast of a standard reconstruction between insets and background for various line resolutions. Cos80 indicates a cosine reconstruction kernel with a cut-off frequency at 80 % of the detector Nyquist frequency. 108

4.12 Filter results: (a) Reconstructed slice of the data-set, (b) magnified excerpt (Cos63 kernel) and (c) result of the RCM filter (9×9 RCM size, 0.225 smoothing, structure preservation 0.9, homogeneity adaption on). The water scaling was omitted in these tests, so no intensity windows are given. Original images are a courtesy of Prof. Dr. Andreas H. Mahnken, RWTH Aachen, Germany. 110
4.13 Filter results for third example: (a) Magnified excerpt (Cos575 kernel), and (b) result of the RCM filter (9×9 RCM size, 0.5 smoothing, structure preservation 0.8, homogeneity adaption on), (c) Cos625 kernel result and (d) result with Shepp-Logan filtered pre-reconstruction. Original images are a courtesy of Prof. Dr. Andreas H. Mahnken, RWTH Aachen, Germany. 111
4.14 MTF comparisons for varying contrast strengths of insets. For the 55 HU example, 1000 realizations were simulated and the MTF estimate from a noise-free unfiltered realization is also shown. For the 109 HU case 500 realizations and for the other examples 250 realizations each were simulated. The estimates from the noise-free realization are omitted for the last three cases as there is only a minor influence of the noise for this number of realizations. 112

List of Tables

1.1 X-ray detector types and typical fields of application. The abbreviation *a-Se* refers to amorphous selenium detectors. 8

1.2 HU value ranges for various body fluids according to [Heis 06]. 26

2.1 LUT and simulation data types used for integrating scintillation detector simulation. 35

2.2 LUT and simulation data types used for counting semiconductor detector simulation. 44

2.3 Example event dataset taken from the energy bin from 70 to 75 keV and consisting of two interactions. 45

3.1 Measurement and simulation set-ups A to E used for the LSR validation. For each set-up, the phantom, data generation method and chosen basis material functions are listed. 73

3.2 List of body materials used in the thorax phantom set-ups D and E, with the former shown in Fig. 3.3. Roman numbers provide an index to each material. Columns 3 to 7 contain the relative systematic deviation of the material ground truth to the basis material representation, see Eq. (3.33). The values represent relative deviations, not percent-values. The upper half of the table includes relative deviations for the water / bone $\mu(E, \mathbf{r})$ representation and the lower half includes the deviations for blood / iodine representations. The respective target energy weighting is given by a tungsten spectrum with the tube voltage stated in the column title. Cases where the relative deviation exceeds 1 % are highlighted. 74

3.3 Integral values of the SWF and LWFs at different locations within the 40 cm water cylinder slice. 76

3.4 Chemical composition of soft tissue reference materials, taken from [ICRU 92]. The table lists mass percentages of the four main elements **H**ydrogen, **C**arbon, **N**itrogen and **O**xygen as well as other elemental contributions. The tissue density is given in the right most column. . 81

4.1 Ground truth and calculated mean (standard deviation) of attenuation values for virtual 120 kVp image from original and processed images. All quantities given in mm^{-1}. Minor shifts in the mean values of 1 % or less can be observed, the standard deviation resp. noise is reduced with increasing bandwidth except for very large bandwidths. The noise increase at large bandwith is caused caused by occasional gradient ascents into the wrong direction. 95
4.2 Average noise reduction for several different test scenarios with optimal bandwidth setting. First number corresponds to low-kVp image, second to high-kVp. Image noise was determined by evaluating the standard deviation in homogeneous image regions. (*) only 80 kVp image was evaluated for the *Foot* dataset. 96
4.3 Overview of conducted experiments. 107
4.4 Estimated noise reduction for various contrasts. 110

Bibliography

[Agos 03] S. Agostinelli *et al.* "G4 - a simulation toolkit". *Nuclear Instruments and Methods in Physics Research Section A*, Vol. 506, No. 3, pp. 250–303, July 2003.

[Aich 04] H. Aichinger, J. Dierker, S. Joite-Barfuß, and M. Säbel. *Radiation Exposure and Image Quality in X-Ray Diagnostic Radiology.* Springer-Verlag, Berlin, 2004.

[Alli 06] J. Allison *et al.* "Geant4 developments and applications". *IEEE Transactions on Nuclear Science*, Vol. 53, No. 1, pp. 270–278, Februar 2006.

[Alva 76] R. E. Alvarez and A. Macovski. "Energy-selective Reconstructions in X-ray Computerized Tomography". *Physics in Medicine and Biology*, Vol. 21, No. 5, pp. 733–744, 1976.

[Baer 00] H. Baer, F. E. Paige, S. D. Protopopescu, and X. Tata. "ISAJET 7.48: A Monte Carlo Event Generator for pp, $\bar{p}p$, and e^+e^- Interactions". 2000.

[Bald 08] M. Balda, S. Wirth, D. Niederlöhner, B. Heismann, and J. Hornegger. "Look-up Table-Based Simulation of Scintillation Detectors in Computed Tomography". In: P. Sellin, Ed., *2008 IEEE Nuclear Science Symposium Conference Record*, pp. 4028–4033, 2008.

[Bald 09] M. Balda, D. Niederlöhner, B. Kreisler, J. Durst, and B. Heismann. "Look-up Table-Based Simulation of Directly-Converting Counting X-Ray Detectors for Computed Tomography". In: B. Yu, Ed., *2009 IEEE Nuclear Science Symposium Conference Record*, pp. 2588–2593, 2009.

[Bald 10a] M. Balda, B. Heismann, and J. Hornegger. "Non-stationary CT image noise spectrum analysis". In: H.-P. Meinzer, T. M. Deserno, H. Handels, and T. Tolxdorff, Eds., *Bildverarbeitung für die Medizin*, pp. 191–195, Berlin, 2010.

[Bald 10b] M. Balda, B. Heismann, and J. Hornegger. "Value-Based Noise Reduction for Low-Dose Dual-Energy Computed Tomography". In: T. Jiang, Ed., *Medical Image Computing and Computer-Assisted Intervention - MICCAI 2010, Part III, LNCS 6363*, pp. 547–554, Berlin, 2010.

[Beng 87] H.-U. Bengtsson and T. Sjöstrand. "The Lund Monte Carlo for hadronic processes - PYTHIA version 4.8". *Computer Physics Communications*, Vol. 46, pp. 43–82, 1987.

[Berg 98] M. J. Berger, J. H. Hubbell, S. M. Seltzer, J. Chang, J. S. Coursey, R. Sukumar, and D. S. Zucker. "XCOM: Photon Cross Sections Database". *NIST Standard Reference Database 8 (XGAM)*, 1998.

[Beut 00] J. Beutel, H. L. Kundel, and R. L. V. Metter. *Handbook of Medical Imaging - Volume 1. Physics and Psychophysics*. SPIE, Bellingham, 2000.

[Bisc 77] C. J. Bischof and J. C. Ehrhardt. "Modulation transfer function of the EMI CT head scanner". *Medical Physics*, Vol. 4, No. 2, pp. 163–167, 1977.

[Bors 08a] A. Borsdorf, S. Kappler, R. Raupach, and J. Hornegger. "Analytic Noise Propagation for Anisotriopic Denoising of CT Images". In: P. Sellin, Ed., *2008 IEEE Nuclear Science Symposium Conference Record*, pp. 5335–5338, 2008.

[Bors 08b] A. Borsdorf, R. Raupach, T. Flohr, and J. Hornegger. "Wavelet based Noise Reduction in CT-Images using Correlation Analysis". *IEEE Transactions on Medical Imaging*, Vol. 27, No. 12, pp. 1685–1703, 2008.

[Burd 01] R. L. Burden and J. D. Faires. *Numerical Analysis*. Brooks/Cole, 7 Ed., 2001.

[Camp 98] M. Campbell, E. H. M. Heijne, G. Meddeler, E. Pernigotti, and W. Snoeys. "A Readout Chip for a 64 x 64 Pixel Matrix With 15-bit Single Photon Counting". *IEEE Transactions on Nuclear Science*, Vol. 45, pp. 751–753, 1998.

[Catt 92] F. Catte, P.-L. Lions, J.-M. Morel, and T. Coll. "Image selective smoothing and edge-detection by nonlinear diffusion". *SIAM Journal on Numerical Analysis*, Vol. 29, pp. 182–193, 1992.

[Chen 08] G.-H. Chen, J. Tang, and S. Leng. "Prior image constrained compressed sensing (PICCS): A method to accurately reconstruct dynamic CT images from highly undersampled projection data sets". *Medical Physics*, Vol. 35, pp. 660–663, 2008.

[Chew 78] E. Chew, G. H. Weiss, R. A. Brooks, and G. Di Chiro. "Effect of CT Noise on Detectability of Test Objects". *American Journal of Radiology*, Vol. 131, pp. 681–685, 1978.

[Cunn 99] I. A. Cunningham and R. Shaw. "Signal-to-noise optimization of medical imaging systems". *Journal of the Optical Society of America A*, Vol. 16, No. 3, pp. 621–632, 1999.

[Enge 94] J. Engel, E. Herrmann, and T. Gasser. "An Iterative Bandwidth Selector for Kernel Estimation of Densities and Their Derivatives". *Journal of Nonparametric Statistics*, Vol. 4, pp. 21–34, 1994.

[Erdl 09] M. Erdélyi, M. Lajkó, R. Kákonyi, and G. Szabó. "Measurement of the x-ray tube anodes' surface profile and its effects on the x-ray spectra". *Medical Physics*, Vol. 36, No. 2, pp. 587–593, 2009.

[Fara 90] J. J. Faraway and M. Jhun. "Bootstrap Choice of Bandwidth for Density Estimation". *Journal of the American Statistical Association*, Vol. 85, pp. 1119–1122, 1990.

[Feld 84] L. A. Feldkamp, L. C. Davis, and J. W. Kress. "Practical cone-beam algorithm". *Journal of the Optical Society of America A*, Vol. 1, No. 6, pp. 612–619, 1984.

[Fisc 98] P. Fischer, J. Hausmann, M. Overdick, B. Raith, N. Wermes, L. Blanquart, V. Bonzom, and P. Delpierre. "A Counting Pixel Readout Chip for Imaging Applications". *Nuclear Instruments and Methods in Physics Research Section A*, Vol. 405, pp. 53–59, 1998.

[Floh 06] T. Flohr, C. McCollough, H. Bruder, M. Petersilka, K. Gruber, C. Süß, M. Grasruck, K. Stierstorfer, B. Krauss, R. Raupach, A. Primak, A. Küttner, S. Achenbach, C. Becker, A. Kopp, and B. Ohnesorge. "First performance evaluation of a dual-source CT (DSCT) system". *European Radiology*, Vol. 16, pp. 256–268, 2006.

[Gier 03] J. Giersch, A. Weidemann, and G. Anton. "ROSI - an object-oriented and parallel-computing Monte Carlo simulation for X-ray imaging". *Nuclear Instruments and Methods in Physics Research Section A*, Vol. 509, No. 1, pp. 151–156, August 2003.

[Gier 08] J. Giersch and J. Durst. "Monte Carlo simulations in X-ray imaging". *Nuclear Instruments and Methods in Physics Research Section A*, Vol. 591, pp. 300–305, 2008.

[Gree 09] D. Greenberger, K. Hentschel, and F. Weinert. *Compendium of Quantum Physics – Concepts, Experiments, History and Philosophy.* Springer, Berlin, 2009.

[Gres 00] H. Gress, H. Wolf, U. Baum, M. Lell, M. Pirkl, W. Kalender, and W. Bautz. "Dose reduction in computed tomography by attenuation based on-line modulation of tube current: Evaluation of six anatomical regions". *European Radiology*, Vol. 10, No. 2, pp. 391–394, 2000.

[Hawk 86] D. J. Hawkes, D. F. Jackson, and R. P. Parker. "Tissue analysis by dual-energy computed tomography". *British Journal of Radiology*, Vol. 59, pp. 537–542, 1986.

[Hawk 97] D. J. Hawkes, D. F. Jackson, and R. P. Parker. "Energy-Dependent Systematic Errors in Dual-energy X-Ray CT". *IEEE Transactions on Nuclear Science*, Vol. 44, No. 2, pp. 212–217, 1997.

[He 10] K. He, J. Sun, and X. Tang. "Guided image filtering". In: *Proceedings of the 11th European conference on Computer vision: Part I*, pp. 1–14, Springer-Verlag, Berlin, Heidelberg, 2010.

[Heis 03] B. J. Heismann, J. Leppert, and K. Stierstorfer. "Density and atomic number measurements with spectral X-ray attenuation method". *Journal of Applied Physics*, Vol. 94, No. 3, pp. 2074–2079, 2003.

[Heis 06] B. J. Heismann and A. H. Mahnken. "Quantitative CT characterization of body fluids with spectral ρZ projection method". In: *Nuclear Science Symposium Conference Record, 2006. IEEE*, pp. 2079–2080, 2006.

[Heis 08] B. J. Heismann, K. Pham-Gia, W. Metzger, D. Niederloehner, and S. Wirth. "Signal transport in Computed Tomography detectors". *Nuclear Instruments and Methods in Physics Research Section A*, Vol. 591, No. 1, pp. 28–33, 2008.

[Heis 09] B. Heismann and M. Balda. "Quantitative image-based spectral reconstruction for computed tomography". *Medical Physics*, Vol. 36, No. 10, pp. 4471–4485, 2009.

[Heis 10] B. Heismann and M. Balda. "Evaluation of an image-based algorithm for quantitative spectral CT applications". In: E. Samei and N. J. Pelc, Eds., *Medical Imaging 2010: Physics of Medical Imaging*, 2010.

[Hilt 04] M. Hilts and C. Duzenli. "Image noise in X-ray CT polymer gel dosimetry". *Journal of Physics Conference Series*, Vol. 3, pp. 252–256, 2004.

[Hsie 98] J. Hsieh. "Adaptive streak artifact reduction in computed tomography resulting from excessive x-ray photon noise". *Medical Physics*, Vol. 25, No. 11, pp. 2139–2147, 1998.

[Hubb 69] J. H. Hubbell, Ed. *Photon cross-sections, attenuation coefficients, and energy absorption coefficients from 10 keV to 100G eV*. National Bureau of Standards (U.S.) Report, Publication No. NSRDS-NBS 29, 1969.

[Huds 94] H. M. Hudson and R. S. Larkin. "Accelerated Image Reconstruction using Ordered Subsets of Projection Data". *IEEE Transactions on Medical Imaging*, Vol. 13, No. 4, pp. 601–609, 1994.

[ICRU 92] ICRU. "ICRU Report 46. Photon, Electron, Proton and Neutron Interaction Data for Body Tissues". Tech. Rep., International Commission on Radiation Units and Measurements, 1992.

[IEC 06] IEC. "IEC 62220-1: Medical electrical equipment — Characteristics of digital X-ray imaging devices — Part 1: Determination of the detective quantum efficiency.". Tech. Rep., International Electrotechnical Commission, Geneva, Switzerland, October 2006.

[Jone 96] M. C. Jones, J. S. Marron, and S. J. Sheather. "A brief survey of bandwidth selection for density estimation". *Journal of the American Statistical Association*, Vol. 91, No. 433, pp. 401–407, 1996.

[Jose 78] P. M. Joseph and R. D. Spital. "A method for correcting bone induced artifacts in CT scanners". *Journal of Computer Assisted Tomography*, Vol. 2, pp. 100–108, 1978.

[Jose 97] P. M. Joseph and C. Ruth. "A method for simultaneous correction of spectrum hardening artifacts in CT images containing both bone and iodine". *Medical Physics*, Vol. 24, No. 10, pp. 1629–1634, 1997.

[Judy 76] P. F. Judy. "The line spread function and modulation transfer function of a computed tomographic scanner". *Medical Physics*, Vol. 3, No. 4, pp. 233–236, 1976.

[Kach 01] M. Kachelriess, O. Watzke, and W. A. Kalender. "Generalized multi-dimensional adaptive filtering for conventional and spiral single-slice, multi-slice, and cone-beam CT". *Medical Physics*, Vol. 28, No. 4, pp. 475–490, 2001.

[Kach 04] M. Kachelriess, M. Knaup, C. Penssel, and W. Kalender. "Flying focal spot (FFS) in cone-beam CT". In: *Nuclear Science Symposium Conference Record, 2004 IEEE*, pp. 3759–3763, 2004.

[Kach 06] M. Kachelriess, T. Berkus, P. Stenner, and W. Kalender. "Empirical Dual Energy Calibration (EDEC) for Cone-Beam Computed Tomography". In: *Nuclear Science Symposium Conference Record, 2006. IEEE*, pp. 2546–2550, 2006.

[Kak 01] A. C. Kak and M. Slaney. *Principles of Computerized Tomographic Imaging*. Society of Industrial and Applied Mathematics, 2001.

[Kale 90] W. A. Kalender, W. Seissler, E. Klotz, and P. Vock. "Spiral volumetric CT with single-breathhold technique, continuous transport, and continuous scanner rotation". *Radiology*, Vol. 176, pp. 181–183, 1990.

[Kapp 09a] S. Kappler, M. Grasruck, D. Niederlöhner, M. Strassburg, and S. Wirth. "Dual-energy performance of dual kVp in comparison to dual-layer and quantum-counting CT system concepts". p. 725842, SPIE, 2009.

[Kapp 09b] S. Kappler, D. Niederlöhner, S. Wirth, and K. Stierstorfer. "A Full-System Simulation Chain For Computed Tomography Scanners". In: B. Yu, Ed., *2009 IEEE Nuclear Science Symposium Conference Record*, 2009.

[Kapp 10a] S. Kappler, F. Glasser, S. Janssen, E. Kraft, and M. Reinwand. "A research prototype system for quantum-counting clinical CT". p. 76221Z, SPIE, 2010.

[Kapp 10b] S. Kappler, D. Niederlöhner, K. Stierstorfer, and T. Flohr. "Contrast-enhancement, image noise, and dual-energy simulations for quantum-counting clinical CT". p. 76223H, SPIE, 2010.

[Kelc 79] F. Kelcz, P. M. Joseph, and S. K. Hilal. "Noise considerations in dual energy CT scanning". *Medical Physics*, Vol. 6, pp. 418–425, October 1979.

[Kese 92] L. Keselbrener, Y. Shimoni, and S. Akselrod. "Nonlinear filters applied on computerized axial tomography: theory and phantom images". *Medical Physics*, Vol. 19, pp. 1057–1064, July 1992.

[Kije 87] M. F. Kijewski and P. F. Judy. "The noise power spectrum of CT images". *Physics in Medicine and Biology*, Vol. 32, pp. 565–575, 1987.

[Klei 29] O. Klein and T. Nishina. "Über die Streuung von Strahlung durch freie Elektronen nach der neuen relativistischen Quantendynamik von Dirac". *Zeitschrift für Physik A: Hadrons and Nuclei*, Vol. 52, pp. 853–868, 1929.

[Kraf 07] E. Kraft, P. Fischer, M. Karagounis, M. Koch, H. Krüger, N. Wermes, C. Herrmann, A. Nascetti, M. Overdick, and W. Rütten. "Counting and Integrating Readout for Direct Conversion X-ray Imaging: Concept, Realization and First Prototype Measurements". *IEEE Transactions on Nuclear Science*, Vol. 54, pp. 383–390, 2007.

[Krei 08] B. Kreisler, J. Durst, T. Michel, and G. Anton. "Generalised adjoint simulation of induced signals in semiconductor X-ray pixel detectors". *Journal of Instrumentation*, Vol. 3, p. 11002, 2008.

[Lass 99] E. Lassner and W.-D. Schubert. *Tungsten: Properties, Chemistry, Technology of the Element, Alloys, and Chemical Compounds*. Springer, Berlin, 1999.

[Leco 06] P. Lecoq, A. Annenkov, A. Gektin, M. Korzhik, and C. Pedrini. *Inorganic Scintillators for Detector Systems*. Springer-Verlag, Berlin, 2006.

[Llop 01] X. Llopart, M. Campbell, D. S. Segundo, E. Pernigotti, and R. Dinapoli. "Medipix2, a 64k pixel read out chip with 55 μm square elements working in single photon counting mode". *IEEE 2001 Nuclear Science Symposium Conference Record*, Vol. 3, pp. 1484–1488, 2001.

[Lu 03] H. Lu, X. Li, L. Li, D. Chen, Y. Xing, J. Hsieh, and Z. Liang. "Adaptive noise reduction toward low-dose computed tomography". In: M. J. Yaffe and L. E. Antonuk, Eds., *Society of Photo-Optical Instrumentation Engineers (SPIE) Conference Series*, pp. 759–766, June 2003.

[Maas 09] C. Maaß, M. Baer, and M. Kachelriess. "Image-based dual energy CT using optimized precorrection functions: A practical new approach of material decomposition in image domain". *Medical Physics*, Vol. 36, No. 8, pp. 3818–3829, 2009.

[Mail 09] N. Mail, D. J. Moseley, J. H. Siewerdsen, and D. A. Jaffray. "The influence of bowtie filtration on cone-beam CT image quality". *Medical Physics*, Vol. 36, No. 1, pp. 22–32, 2009.

[Mang 95] S. H. Manglos, G. M. Gagne, A. Krol, F. D. Thomas, and R. Narayanaswamy. "Transmission maximum-likelihood reconstruction with ordered subsets for cone beam CT". *Physics in Medicine and Biology*, Vol. 40, pp. 1225–1241, 1995.

[McCu 75] E. C. McCullough. "Photon attenuation in computed tomography". *Medical Physics*, Vol. 2, No. 6, pp. 307–320, 1975.

[Nalc 79] O. Nalcioglu and R. Lou. "Post-reconstruction Method for Beam Hardening in Computerised Tomography". *Physics in Medicine and Biology*, Vol. 24, No. 2, pp. 330–340, 1979.

[Noo 02] F. Noo, M. Defrise, R. Clackdoyle, and H. Kudo. "Image reconstruction from fan-beam projections on less than a short scan". *Physics in Medicine and Biology*, Vol. 47, pp. 2525–2546, 2002.

[Pack 04] J. D. Pack, F. Noo, and H. Kudo. "Investigation of saddle trajectories for cardiac CT imaging in cone-beam geometry". *Physics in Medicine and Biology*, Vol. 49, pp. 2317–2336, 2004.

[Parz 62] E. Parzen. "On estimation of a probability density function and mode". *Annals of Mathematical Statistics*, Vol. 33, pp. 1065–1076, 1962.

[Pett 98] H. Pettersson, D. Allison, and G. K. V. Schulthess. *The Encyclopaedia of Medical Imaging, Volume I: Physics, Techniques and Procedures*. NICER Institute, Oslo, 1998.

[Rabb 87] M. Rabbani, R. Shaw, and R. V. Metter. "Detective quantum efficiency of imaging systems with amplifying and scattering mechanisms". *Journal of the Optical Society of America A*, Vol. 4, No. 5, pp. 895–901, 1987.

[Rado 17] J. Radon. "Über die Bestimmung von Funktionen durch ihre Integralwerte längs gewisser Mannigfaltigkeiten". *Berichte über die Verhandlungen der Königlich-Sächsischen Gesellschaft der Wissenschaften zu Leipzig*, Vol. 69, pp. 262–277, 1917.

[Ried 78] S. J. Riederer, N. J. Pelc, and D. A. Chesler. "The noise power spectrum in computed x-ray tomography". *Physics in Medicine and Biology*, Vol. 23, pp. 446–454, 1978.

[Rose 46] A. Rose. "A unified approach to the performance of photographic film, television pickup tubes and the human eye". *Journal of the Society of Motion Picture Engineers*, Vol. 47, p. 273, 1946.

[Ruth 97] C. Ruth and P. M. Joseph. "Estimation of a photon energy spectrum for a computed tomography scanner". *Medical Physics*, Vol. 24, No. 5, pp. 695–702, 1997.

[Rutt 80] B. Rutt and A. Fenster. "Split-Filter Computed Tomography: A Simple Technique for Dual Energy Scanning". *Journal of Computer Assisted Tomography*, Vol. 4, No. 4, pp. 501–509, 1980.

[Scha 08] M. Schaap, A. M. R. Schilham, K. J. Zuiderveld, M. Prokop, E.-J. Vonken, and W. J. Niessen. "Fast Noise Reduction in Computed Tomography for Improved 3-D Visualization". *IEEE Transactions on Medical Imaging*, Vol. 27, No. 8, pp. 1120–1129, 2008.

[Schi 06] A. M. R. Schilham, B. van Ginneken, H. Gietema, and M. Prokop. "Local Noise Weighted Filtering for Emphysema Scoring of Low-Dose CT Images". *IEEE Transactions on Medical Imaging*, Vol. 25, No. 4, pp. 451–463, 2006.

[Schl 08] J. P. Schlomka, E. Roessl, R. Dorscheid, S. Dill, G. Martens, T. Istel, C. Bäumer, C. Herrmann, R. Steadman, G. Zeitler, A. Livne, and R. Proksa. "Experimental feasibility of multi-energy photon-counting K-edge imaging in pre-clinical computed tomography". *Physics in Medicine and Biology*, Vol. 53, No. 15, p. 4031, 2008.

[Schm 04] B. Schmitt, C. Bronnimann, E. F. Eikenberry, G. Hulsen, H. Toyokawa, R. Horisberger, F. Gozzo, B. Patterson, C. Schulze-Briese, and T. Tomizaki. "Development of single photon counting detectors at the Swiss Light Source". *Nuclear Instruments and Methods in Physics Research Section A*, Vol. 518, pp. 436–439, 2004.

[Scot 92] D. W. Scott. *Multivariate Density Estimation: Theory, Practice, and Visualization*. John Wiley, New York, 1992.

[Sega 03] W. P. Segars, B. M. W. Tsui, E. C. Frey, and E. K. Fishman. "Extension of the 4D NCAT phantom to dynamic X-ray CT simulation". *IEEE Nuclear Science Symposium Conference Record*, Vol. 5, pp. 3195–3199, 2003.

[Shar 08] T. Sharir, S. Ben-Haim, K. Merzon, V. Prochorov, D. Dickman, S. Ben-Haim, and D. S. Berman. "High-Speed Myocardial Perfusion Imaging: Initial Clinical Comparison With Conventional Dual Detector Anger Camera Imaging". *Journal of the American College of Cardiology: Cardiovascular Imaging*, Vol. 1, No. 2, pp. 156–163, 2008.

[Sidk 05] E. Y. Sidky, L. Yu, X. Pan, Y. Zou, and M. Vannier. "A robust method of x-ray source spectrum estimation from transmission measurements: Demonstrated on computer simulated, scatter free transmission data". *Journal of Applied Physics*, Vol. 97, No. 124701, 2005.

[Sten 07] P. Stenner, T. Berkus, and M. Kachelriess. "Empirical dual energy calibration (EDEC) for cone-beam computed tomography". *Medical Physics*, Vol. 34, No. 9, pp. 3630–3641, 2007.

[Tagu 07] K. Taguchi, M. Zhang, E. C. Frey, J. Xu, W. P. Segars, and B. M. W. Tsui. "Image-domain material decomposition using photon-counting CT". p. 651008, SPIE, 2007.

[Tayl 89] C. C. Taylor. "Bootstrap Choice of the Smoothing Parameter in Kernel Density Estimation". *Biometrika*, Vol. 76, pp. 705–712, 1989.

[Tlus 06] L. Tlustos, R. Ballabriga, M. Campbell, E. Heijne, K. Kincade, X. Llopart, and P. Stejska. "Imaging properties of the Medipix2 system exploiting single and dual energy thresholds". *IEEE Transactions on Nuclear Science*, Vol. 53, pp. 367–372, 2006.

[Toma 98] C. Tomasi and R. Manduchi. "Bilateral filtering for gray and color images". In: *Sixth International Conference on Computer Vision*, pp. 839–846, 1998.

[Tuck 91] D. M. Tucker, G. T. Barnes, and D. P. Chakraborty. "Semiempirical model for generating tungsten target x-ray spectra". *Medical Physics*, Vol. 18, No. 2, pp. 211–218, 1991.

[Vett 86] J. Vetter, W. Perman, W. A. Kalender, R. Mazess, and J. Holden. "Evaluation of a prototype dual-energy computed tomographic apparatus. II. Determination of vertebral bone mineral content". *Medical Physics*, Vol. 13, No. 3, pp. 340–343, 1986.

[Wang 05] J. Wang, H. Lu, T. Li, and Z. Liang. "Sinogram noise reduction for low-dose CT by statistics-based nonlinear filters". pp. 2058–2066, SPIE, 2005.

[Wang 08] G. Wang, H. Yu, and B. D. Man. "An outlook on x-ray CT research and development". *Medical Physics*, Vol. 35, No. 3, pp. 1051–1064, 2008.

[Weav 84] J. B. Weaver and A. L. Huddleston. "Attenuation coefficients of body tissues using principal-components analysis". *Medical Physics*, Vol. 12, No. 1, pp. 40–45, 1984.

[Weic 98] J. Weickert. *Anisotropic Diffusion in Image Processing*. Teubner-Verlag, Stuttgart, 1998.

[Wirt 03] S. Wirth, W. Metzger, K. Pham-Gia, and B. J. Heismann. "Impact of Photon Transport Properties on the Detection Efficiency of Scintillator Arrays". *IEEE Nuclear Science Symposium Conference*, No. M11-212, pp. 2602–2603, 2003.

[Xu 09] D. Xu, D. A. Langan, X. Wu, J. D. Pack, T. M. Benson, J. E. Tkaczky, and A. M. Schmitz. "Dual energy CT via fast kVp switching spectrum estimation ". p. 72583T, SPIE, 2009.

[Yan 00] C. H. Yan, R. T. Whalen, G. S. Beaupré, S. Y. Yen, and S. Napel. "Reconstruction Algorithm for Polychromatic CT Imaging: Application to Beam Hardening Correction". *IEEE Transactions on Medical Imaging*, Vol. 19, No. 1, pp. 1–11, 2000.

[Yan 99] C. H. Yan, R. T. Whalen, G. S. Beaupré, S. Y. Yen, and S. Napel. "Modeling of polychromatic attenuation using computed tomography reconstructed images". *Medical Physics*, Vol. 26, No. 4, pp. 631–642, 1999.

[Zatz 77] L. M. Zatz and R. E. Alvarez. "An Inaccuracy in Computed Tomography: The Energy Dependence of CT Values". *Radiology*, Vol. 124, No. 1, pp. 91–98, 1977.

[Zhen 08] L. Zheng, D. Maksimov, T. Stutzmann, S. Jochum, C. Brockmann, S. Diehl, and J. Hesser. "Removal of bone information in dual energy CT". In: *Proceedings of the MICCAI-CVII Workshop*, pp. 120–127, 2008.

[Zou 08] Y. Zou and M. D. Silver. "Analysis of fast kV-switching in dual energy CT using a pre-reconstruction decomposition technique". p. 691313, SPIE, 2008.

[Zwie 65] H. J. Zwieg. "Detective quantum efficiency of photodetectors with some amplifying mechanism". *Journal of the Optical Society of America*, Vol. 55, pp. 525–528, 1965.